KfK 4674
April 1990

A New Approach for Precise Measurements of keV Neutron Capture Cross Sections: the Examples of ^{93}Nb, ^{103}Rh, and ^{181}Ta

K. Wisshak, F. Voß, F. Käppeler, G. Reffo
Institut für Kernphysik

Kernforschungszentrum Karlsruhe

KERNFORSCHUNGSZENTRUM KARLSRUHE
Institut für Kernphysik

KfK 4674

A NEW APPROACH FOR PRECISE MEASUREMENTS OF keV NEUTRON CAPTURE CROSS SECTIONS: THE EXAMPLES OF ^{93}Nb, ^{103}Rh, AND ^{181}Ta

K. Wisshak, F. Voß, F. Käppeler and G. Reffo*

*Permanent address: E.N.E.A. Bologna, Viale Erolani 8. I-40138 Bologna, Italy

Kernforschungszentrum Karlsruhe GmbH, Karlsruhe

Kernforschungszentrum Karlsruhe GmbH
Postfach 3640, 7500 Karlsruhe 1

ISSN 0303-4003

ABSTRACT

A new experimental method has been implemented for precise measurements of neutron capture cross sections in the energy range from 3 to 200 keV. Neutrons are produced via the $^{7}Li(p,n)^{7}Be$ reaction using a pulsed 3 MV Van de Graaff accelerator. The neutron energy is determined by the time of flight technique using flight paths of less than 1 m. Capture events are detected with the Karlsruhe 4π Barium Fluoride Detector. This detector is characterized by a resolution in gamma-ray energy of 14% at 662 keV and 7% at 2.5 MeV, a time resolution of 500 ps, and a peak efficiency of 90% at 1 MeV. Capture events are registered with ~95% probability above a gamma-ray threshold of 2.5 MeV.

The combined effect of the relatively short primary flight path, the 10 cm inner radius of the detector sphere, and of the low capture cross section of BaF_2 allows to discriminate the main background due to capture of sample scattered neutrons in the scintillator via time of flight, leaving part of the neutron energy range completely undisturbed. The high efficiency and good energy resolution for capture gamma-rays yields a further reduction of this background by using only the relevant energy channels for data evaluation.

In the first measurements with the new detector, the neutron capture cross sections of ^{93}Nb, ^{103}Rh, and ^{181}Ta were determined in the energy range from 3 to 200 keV relative to gold as a standard. The cross section ratios could be determined with overall systematic uncertainties of 0.7 to 0.8%; statistical uncertainties were less than 1% in the energy range from 20 to 100 keV, if the data are combined in 20 keV wide bins. The necessary sample masses were of the order of one gram. Further improvements with respect to sensitivity and accuracy are discussed.

ZUSAMMENFASSUNG

EINE NEUE METHODE ZUR GENAUEN BESTIMMUNG VON NEUTRONENEINFANGQUERSCHNITTEN IM keV BEREICH: DIE BEISPIELE ^{93}Nb, ^{103}Rh und ^{181}Ta.

Es wurde ein neuartiges Experiment aufgebaut, um Wirkungsquerschnitte für Neutroneneinfang im Energiebereich von 3 bis 200 keV sehr genau zu bestimmen. Die Neutronen werden mit einem gepulsten 3 MV Van de Graaff Beschleuniger über die ^{7}Li(p,n)^{7}Be Reaktion erzeugt. Die Neutronenenergie wird mit Hilfe der Flugzeittechnik bestimmt, wobei die Flugwege typischerweise ≦ 1 m betragen. Die Einfangereignisse werden mit dem Karlsruher 4π Barium Fluorid Detektor nachgewiesen. Dieser Detektor besitzt eine Energieauflösung für Gamma Strahlung von 14 % bei 662 keV und 7 % bei 2.5 MeV, eine Zeitauflösung von 500 ps und eine Nachweiswahrscheinlichkeit für die volle Energie der Gammaquanten von 90 % bei 1 MeV. Einfangereignisse können so mit ~95 % Wahrscheinlichkeit oberhalb einer Schwelle von 2.5 MeV nachgewiesen werden.

Die Kombination aus kurzem Flugweg, 10 cm Innenradius der BaF_2 Kugelschale und dem geringen Einfangquerschnitt von Barium erlaubt es, den Untergrund durch Einfang gestreuter Neutronen im Szintillatormaterial auf Grund seiner Zeitstruktur vom Meßeffekt zu unterscheiden. Die hohe Ansprechwahrscheinlichkeit und die gute Energieauflösung für Gamma Strahlung ermöglicht eine weitere Reduzierung dieses Untergrundes durch Auswahl geeigneter Energiebereiche bei der Auswertung.

In der ersten Messung mit dem neuen Detektor wurden die Neutroneneinfangquerschnitte von ^{93}Nb, ^{103}Rh und ^{181}Ta im Energiebereich von 3 bis 200 keV relativ zu Gold als Standard bestimmt. Für das Verhältnis der Wirkungsquerschnitte wurde eine systematische Unsicherheit von 0.7 bis 0.8 % erreicht; die statistische Genauigkeit ist besser als 1 % im Energiebereich von 20 bis 100 keV, wenn man die Daten in 20 kev breite Intervalle zusammenfaßt. Im Mittel wurde lediglich 1 g Probenmaterial benötigt. Mögliche Verbesserungen der Empfindlichkeit und Meßgenauigkeit werden diskutiert.

CONTENTS

I. INTRODUCTION

The accurate determination of neutron capture cross sections in the keV neutron energy range is of interest in two different areas:

(i) For nuclear astrophysics accurate data are required for the quantitative investigation of nucleosynthesis in the so called slow neutron capture process or s-process for short[1]. There, the fundamental quantity is the product $N_s\langle\sigma\rangle(A)$, where N_s denotes the isotopic abundance and $\langle\sigma\rangle$ the neutron capture cross section averaged over a Maxwellian velocity distribution at a temperature of kT=30 keV. In many actual problems it is sufficient to know the ratio of this quantity for two isotopes of the same element. In this case, the accuracy is clearly limited by the cross sections since isotopic ratios are known with uncertainties of less than 0.5% (Ref.2). In favorable cases, it is even possible to determine elemental abundances with an uncertainty of 2% (Refs.3,4), which is still significantly better than the accuracy of present cross section measurements.

Detailed investigations during the last ten years showed that the conclusions on the physical conditions during the s-process, such as temperature and neutron density, are limited by the accuracy of the measured neutron capture cross sections, and that uncertainties of 1% or even better are highly desirable[1]. This requires an improvement of present experimental techniques by factors of 5-10, since the accuracy of the presently available data is 5-10% and in many cases even worse[5].

(ii) In the field of applied physics neutron capture cross sections in the keV energy range are required mainly in fast reactor design. According to the World Request List for Nuclear Data[6] capture cross sections of structural materials and actinide isotopes are needed with accuracies up to 1 %.

The registration of a neutron capture event and especially the accurate determination of the cross section is complicated by the fact that there is no unique signature in the exit channel, as e.g. in (n,p) or (n,α) reactions. The capture process results in a cascade of prompt gamma-rays, the multiplicity and the energies of the individual gamma-rays being determined by the transition probabilities to a great variety of nuclear levels. The only fixed quantity is the sum energy of the cascade that corresponds

to the binding energy of the captured neutron (6 to 8 MeV for most isotopes of interest for s-process studies) increased by the kinetic energy of the captured neutron (3-200 keV). For isotopes with Z>26, the level density at excitation energies of several MeV is so large that the capture cross section is spread over many possible cascades. According to statistical model calculations for neutron capture in gold[7] more than 4000 cascades have to be considered in order to cover 95% of the cross section (see section IV). For ^{56}Fe, a typical isotope with intermediate mass, the respective number is still 300 (Refs.8,9). The average gamma-ray multiplicity of the cascades is 3 to 4 with maximum values of up to 10.

The accurate determination of the cross section requires a detector with an efficiency independent of the individual gamma-ray cascades. Since only a comparatively low neutron flux is available at the sample position, large sample masses have to be used in order to obtain sufficient statistics. The corresponding corrections for neutron multiple scattering and self-absorption and for absorption of capture gamma-rays represent a second major problem for reliable measurements.

After three decades of neutron capture cross section measurements with large liquid scintillator tanks[10,11], Moxon-Rae detectors[9,12], and C_6D_6 or C_6F_6 detectors[13,14], the potentials of these techniques seem to be exhausted. As mentioned already, the related accuracies are limited to about 5%.

In case of the liquid scintillator tank, the main problems arise from the poor energy resolution of the scintillator material. A significant fraction of events is registered with low pulse height only and thus is buried underneath a background due to natural radioactivity and to capture of scattered neutrons in the hydrogen of the scintillator. The necessary extrapolation of the pulse height spectrum to low energies yields systematic uncertainties of the order of ten percent. Therefore, this method was abandoned relatively soon. Better results were obtained with Moxon-Rae detectors and with small hydrogen-free C_6D_6 or C_6F_6 liquid scintillators in combination with the pulse height weighting technique.In the latter cases, on average only one gamma-ray is detected from the capture cascade due to the low detector efficiency. The efficiency for the entire capture cascade has therefore to be determined via the pulse height observed in the detector. This is complicated and requires to calculate or to measure the efficiency for monoenergetic gamma-rays and the related pulse height distribution precisely. In

this procedure, all materials near the scintillator need to be considered, because energetic electrons created by capture gamma-rays outside the scintillator may be detected as well, thus increasing the efficiency. This problem was discussed in detail recently[15,16], and is hard to solve with high precision. As a result, many of the previously published cross sections exhibit discrepancies, which significantly exceed the quoted accuracies. A prominent example is the capture cross section in the 1.18 keV resonance of ^{56}Fe (Refs.17,18,19), but also for the isotopes of the present investigation one finds severe discrepancies between the data of Refs. 20, 21, 22 and our first experiment[7] (see section VII).

The difficulties related to the sample mass may be illustrated by the following comparison: In the measurements of the neutron capture cross sections of ^{93}Nb, ^{103}Rh, and ^{181}Ta carried out at ORELA[20, 21, 22], sample masses of 10 to 30 g were used, whereas 1.5 to 6 g were sufficient in Van de Graaff experiments[7]. For example, the corrections for multiple scattering and self-shielding in the Nb-measurements of Refs. 7,22 were 5 and 14 % at 200 keV neutron energy, respectively.

The aim of the present investigation was to implement a new experimental technique for the determination of neutron capture cross sections that avoids or reduces the problems of the existing techniques in order to improve the accuracy by factors of 5 to 10. It will mainly be used for measurements motivated by nuclear astrophysics in the mass range from iron to bismuth. The intended neutron energy range is 3 to 200 keV.

The desired improvement could be realized with a new capture detector, the Karlsruhe 4π Barium Fluoride (BaF_2) Detector. This detector combines about 100% efficiency for gamma-rays up to 10 MeV with good energy and time resolution. The full potentials of this detector can best be used in connection with a Van de Graaff accelerator for neutron production via the ^{7}Li(p,n)^{7}Be reaction, where short flight paths of less than one meter can be used in time of flight (TOF) experiments (see section II). The detector, originally planned to be build from bismuth germanium oxyde (BGO), was proposed in 1983 (Ref.23). The design studies and preliminary results from prototype crystals have been published in Refs.24,25,26 . The final detector and the experimental technique is described in detail in Ref.27. In the present paper, we present the results of first measurements that were used to study the procedures of data acquisition, data evalua-

tion, and to optimize the experimental setup. Samples were the stable monotopic elements ^{93}Nb, ^{103}Rh, and ^{181}Ta as well as ^{197}Au that was used as a cross section standard. These isotopes cover the entire mass range of interest for the astrophysical application and exhibit significantly different nuclear properties, i.e. level densities and neutron binding energies, to investigate the respective detector response. Furthermore, these samples are easily available with high purity, and the cross sections have previously been studied in detail [7,20,21,22]. In case of ^{181}Ta, it is also possible to check the results by an independent activation experiment that is presently underway[28].

A first approach to measure neutron capture events with a 4π detector of good energy resolution and high efficiency was reported by Muradjan et al.(Ref.29). However, the use of NaI(Tl) as detector material did not allow for precise measurements in the keV neutron energy range. The same holds for a spectrometer recently described by Block et al. (Ref.30). Both instruments are well suited for measurements in the eV range, where the detector can be shielded from neutrons scattered in the sample. The use of BGO as detector material was realized by Yamamoto et al.[31], but their design is simpler and less efficient compared to the present setup and, hence, cannot yield the accuracy aimed at in our study. Presently, another 4π BaF_2 detector is under construction at the LANSCE facility[32] in Los Alamos, which has about the same efficiency as the Karlsruhe detector.

II. EXPERIMENTAL METHOD

A detector for the accurate determination of neutron capture cross sections must meet the following requirements:

(i) Efficiency of about 100% for gamma-ray energies up to 10 MeV;
(ii) Good energy resolution (10% at 1 MeV gamma-ray energy);
(iii) Good time resolution (Δt=1 ns);
(iv) Low sensitivity for the detection of neutrons scattered from the sample.

The first feature guarantees that all gamma-rays of the capture cascade are registered in the detector; hence, their added signals represent the total energy of the cascade, which corresponds to the neutron binding energy. This sum energy is the only reliable signature of a capture event independent of the cascade multiplicity.

With the second requirement, all capture events show up in the sum energy spectrum of the detector in a sharp line at the neutron binding energy. In this way, these events are separated from the gamma-ray background at low energies (< 2.5 MeV), so that good signal to background ratios can be obtained in the experiment.

A good time resolution of the detector is important since the energy of the captured neutrons are to be measured by their TOF. In the present case it is also required for the discrimination of background due to sample scattered neutrons as discussed below.

The last requirement is of key importance for the design of this new experimental setup. For most isotopes of astrophysical interest, the cross sections for neutron scattering are 10 to 100 times larger than for capture. These scattered neutrons being captured in the detector material results in a background that is difficult to distinguish from true capture events in the sample.

The above requirements were satisfied by a 4π BaF_2 detector in combination with a Van de Graaff accelerator for neutron production as sketched in Fig. 1. Neutrons are

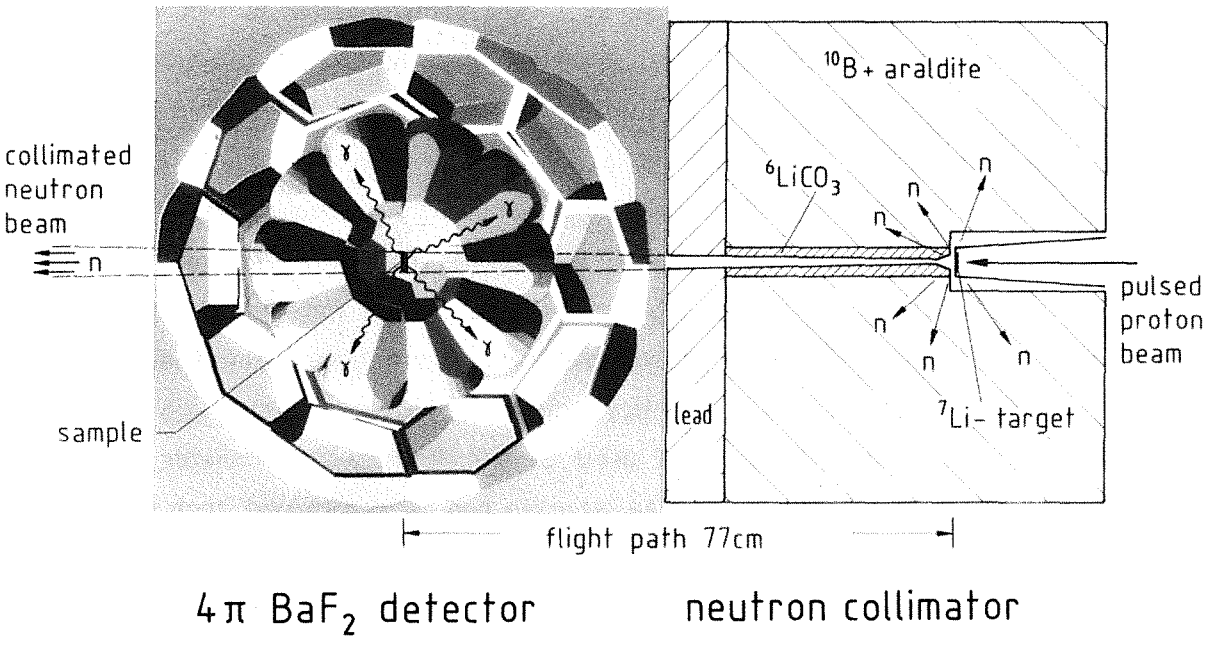

FIG.1 Schematic setup for the determination of neutron capture cross sections in the energy range from 3 to 200 keV using a Van de Graaff accelerator and a 4π gamma-ray detector.

obtained via the $^{7}Li(p,n)^{7}Be$ reaction using the pulsed proton beam of the accelerator. At a proton energy of approximately 2 MeV, continuous neutron spectra in the required energy range from 3 to 200 keV are emitted. A massive shield serves for producing a narrow, well collimated neutron beam to pass through the detector without hitting the scintillator. The samples are located in the centre of the detector at a flight path of 77cm from the lithium target. The total gamma-ray cascade is absorbed in the detector, and the energy of the captured neutrons is determined by the flight time between neutron target and sample (typically 100 to 500 ns depending on energy).

The excellent properties of BaF_2 for detection of gamma-rays were discovered in 1983 (Ref.33) and large crystals became available[34] when we started with the design of the 4π detector. This scintillator combines outstanding timing properties with good energy resolution; it also exhibits small cross sections for capture of keV neutrons.

The detector, which is described in detail in Ref.27 consists of 42 crystals shaped as hexagonal and pentagonal truncated pyramids forming a spherical shell with 10 cm inner radius and 15 cm thickness. Each crystal is supplied with its own photomultiplier and reflector, thus representing an independent gamma-ray detector. Each detector module covers the same solid angle with respect to the sample in the centre. The energy resolution for the sum energy signal of the total detector is 14% at 662 keV and 7% at 2.5 MeV gamma-ray energy. The peak efficiency is 90% at 1 MeV and the time resolution is 500 ps.

The 4π detector records capture cascades with about 95% probability above a threshold of 2.5 MeV in the sum energy spectrum. Besides its application for neutron capture cross section measurements, the detector is also suited for the determination of gamma-ray multiplicities, angular distributions, and capture gamma-ray spectra. It may also be used for the investigation of (p,γ) and (α,γ) reactions, which are of interest for the origin of the light elements. If used as a multiplicity spectrometer, the fission to capture cross section ratio of actinide isotopes can be determined, that is important for reactor applications.

Most of the features of the present experimental method represent significant improvements compared to the existing setups:

(i) Neutrons are produced exactly and only in the energy range of interest for the

intended application in nuclear astrophysics. At the reaction threshold of the $^{7}Li(p,n)^{7}Be$ reaction of E_p=1.881 MeV, quasi monoenergetic neutrons are produced with an energy of 31 keV. This fits well to the thermal energies of 25 to 30 keV at which the s-process is supposed to work in stellar interiors. Adjusting the proton energy slightly above the reaction threshold produces a continuous neutron spectrum in the energy range relevant for the determination of the Maxwellian averaged stellar cross sections, e.g. from 3 to 200 keV. In repeated runs with different neutron spectra, different background conditions are achieved, which allow for reliable corrections, while additional backgrounds from neutrons outside the relevant energy range are avoided, in contrast to "white" neutron sources where the spectra extend from thermal energies up to the MeV range.

(ii) The entire capture cascade is absorbed in the detector; hence, the sum energy represents a clear signature of the capture event for its safe identification.

(iii) The good energy resolution causes the capture events to be concentrated in a line in the sum energy spectrum. About 95% of the capture events are registered with a sum energy of more than 2.5 MeV, well separated from most of the background. The correlated systematic uncertainty in the present experiment was found to be 0.6 % and will be reduced by further improvements (see section VIII).

(iv) Due to the small capture cross sections of the of barium isotopes, the detector exhibits a very low neutron sensitivity: About 90% of the sample scattered neutrons escape from the scintillator material without producing a background signal.

(v) The short primary flight path of 77 cm and the inner radius of the detector of 10 cm guarantees that part of the TOF spectrum at high energies is completely undisturbed by background from sample scattered neutrons. This is important as this part offers optimum signal to background ratio and is used for normalization (see section IV). As shown in Ref.27, it is possible to cover the total energy range from 30 to 200 keV neutron energy free from this type of background by choosing different proton energies in subsequent experimental runs.

(vi) Background from sample scattered neutrons will disturb the measured effect at lower neutron energies. Since these neutrons are scattered 20 times on average

before they are captured in the scintillator, most of these events are delayed in time due to their additional flight path and their decreasing velocity. Therefore, they fall partly in a TOF interval, where no primary capture events are observed, and do not affect the measurement. It has to be mentioned that features (v) and (vi) are lost in LINAC experiments where flight paths of 10 m or more have to be used.

(vii) According to the large binding energies of ^{135}Ba and ^{137}Ba, capture events in barium are concentrated in the sum energy spectrum at about 9 MeV. If the binding energy of the measured isotope is below this value, these background events can be efficiently suppressed. This is the case for most isotopes of interest for nuclear astrophysics.

(viii) The high efficiency for capture events allows to use rather small samples.In this first measurement on ^{93}Nb, ^{103}Rh, and ^{181}Ta, sample masses of 0.5 to 1.6g were found to be sufficient, 13 to 27 times less than in LINAC experiments[20,21,22] and 3 to 6 times less than in our previous experiment with Moxon-Rae detectors[7]. Correspondingly, corrections for gamma-ray self absorption are negligible, and those for neutron multiple scattering and self-shielding are of the order of 1 % for most of the covered energy range (see section IV). With the improvements discussed in section VIII it will be possible to reduce the sample mass further by a factor of 2 to 3.

(ix) The 4π geometry of the detector makes the measurement insensitive to a possible angular anisotropy of the capture gamma-rays and reduces the problem of gamma-ray self-absorption.

III. MEASUREMENTS

A. Neutron source

The measurements were performed at the Karlsruhe 3MV Van de Graaff accelerator.The important parameters of the neutron source are compiled in Table I. Neutrons are produced via the ^{7}Li(p,n)^{7}Be reaction. The pulsed proton beam hits a metallic lithium target of 6 mm diameter and ~2 mg/cm^2 thickness evaporated onto a 0.3 mm thick copper backing. The target is cooled via heat conduction by water flowing in a closed

TABLE I. Important parameters of the neutron source

Accelerator:	3 MV Van de Graaff
Proton energy:	30 and 100 keV above the threshold of the $^{7}Li(p,n)^{7}Be$ reaction at 1.881 MeV
Repetition rate:	250 kHz
Pulse width:	2 ns
Beam intensity:	2 μA
Neutron beam:	continuous neutron spectra in the energy ranges from 3 to 100 keV and 3 to 200 keV, collimated to 25 mm diameter at the sample position
Neutron target:	metallic lithium (~2 mg/cm^2) evaporated onto water cooled copper backing (0.3 mm thickness)
Flight path:	77 cm

tube about 3 cm behind the lithium target. This cooling prooved to be sufficient for the low beam currents applied in the present experiment, and replaced the previously used direct cooling of the target backing by an open water flow that did not allow for reliable monitoring of the neutron flux (see below).

The proton energy was adjusted 100 keV above the reaction threshold of the $^{7}Li(p,n)^{7}Be$ reaction, yielding a continuous neutron spectrum in the energy range from 3 to 200 keV at the sample position, which covers the entire energy range of interest for s-process studies. An additional run was performed with the proton energy 30 keV above threshold, restricting the neutron energy range from 3 to 100 keV. In this case, the signal to background ratio at low neutron energies is significantly better as in the first run due to the reduced integral neutron flux.

The repetition rate of the accelerator was chosen to 250 kHz and the correlated beam current is 2 μA. Though the primary neutrons pass the sample at 77 cm distance from the target in a time interval of only ~700 ns, the low repetition rate was required to avoid overlap with the time-dependent background due to sample scattered neutrons, which appears with delays of up to 3 μs.

The neutron target is surrounded by a shield of ~1 m^3 volume. The inner part consists of blocks casted from boron carbide and araldite mixed in a ratio of 4:1 by weight. The central part of the collimator defining the neutron beam is made from separate pieces that can be changed if a different diameter is desired. Optionally, pieces made from isotopically pure ^6Li carbonate can be used as well. In the present geometry, the beam diameter at the sample position is 25mm. The central part of the collimator is surrounded by at least 25 cm of boron loaded paraffin. Towards the BaF_2 detector, gamma-rays produced in the neutron target and in the collimator are suppressed by 10 cm lead.

The required quality of the collimator can be estimated from the following numbers: Of the ~2×10^7 neutrons produced per sec in the neutron target, ~8×10^3 s^{-1} are hitting the sample and only ~10 n/s are captured. Therefore, the shielding factor of the collimator has to be larger than ~10^8 to avoid unacceptable backgrounds.

B. The Karlsruhe 4π barium fluoride detector

The Karlsruhe 4π BaF_2 detector is used for registration of the capture events. A photograph of the opened detector is given in Fig. 2, showing part of the 42 crystals; these are shaped as hexagonal and pentagonal truncated pyramids and form a spherical shell with 20 cm inner diameter and 15 cm thickness. Each crystal is covered by a reflector and a canning of 0.5 mm total thickness, and is viewed by a 5 inch phototube with quartz window (EMI 9823 QKA), thus representing a complete gamma-ray detector. The individual detector modules are mounted in a spherical honeycomb structure, so that they can be replaced and adjusted individually. The detector is subdivided into two parts fixed in octogonal frames, which can be moved on rails independent of each other over a maximum distance of 1.5 m. In this way, the detector can be opened for easy access of the samples or it can be shifted as a whole in order to change the flight path between neutron target and sample.

In the present state the detector is used as a calorimeter and only the sum energy signal and the TOF are recorded togeter with a 42 bit pattern indicating those modules that have fired per event. The installation of an ADC system is underway, by which gamma-ray energy and TOF can be recorded for each detector module separately. The essential part of the detector electronics for data processing is shown in Fig.3. Within 20 ns, a fast decision is made, whether the sum energy of a particular event exceeds a threshold of typically 2 to

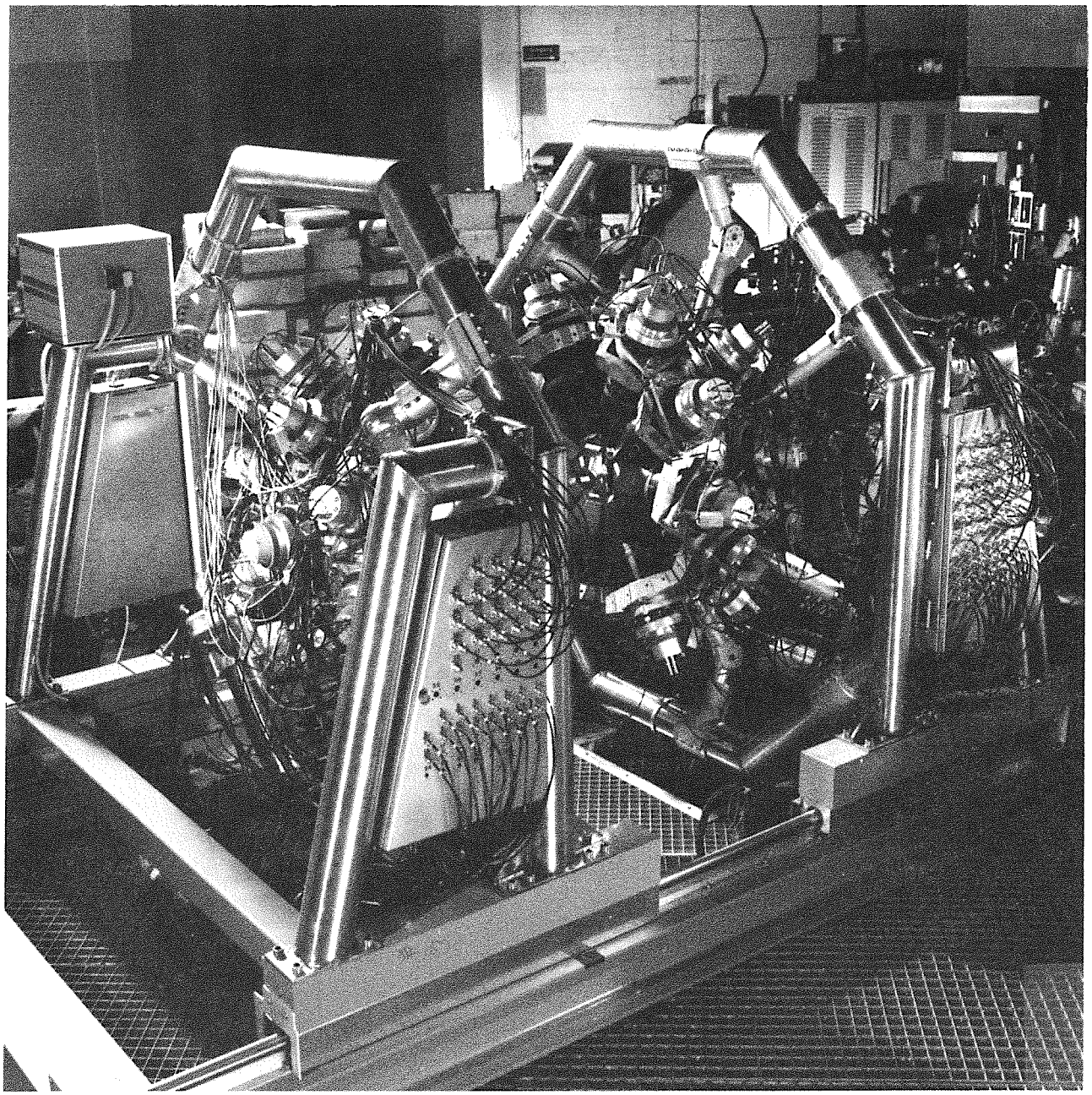

FIG.2 Photograph of the Karlsruhe 4π Barium Fluoride Detector showing the opened detector.

ELECTRONICS FOR SIGNAL PROCESSING

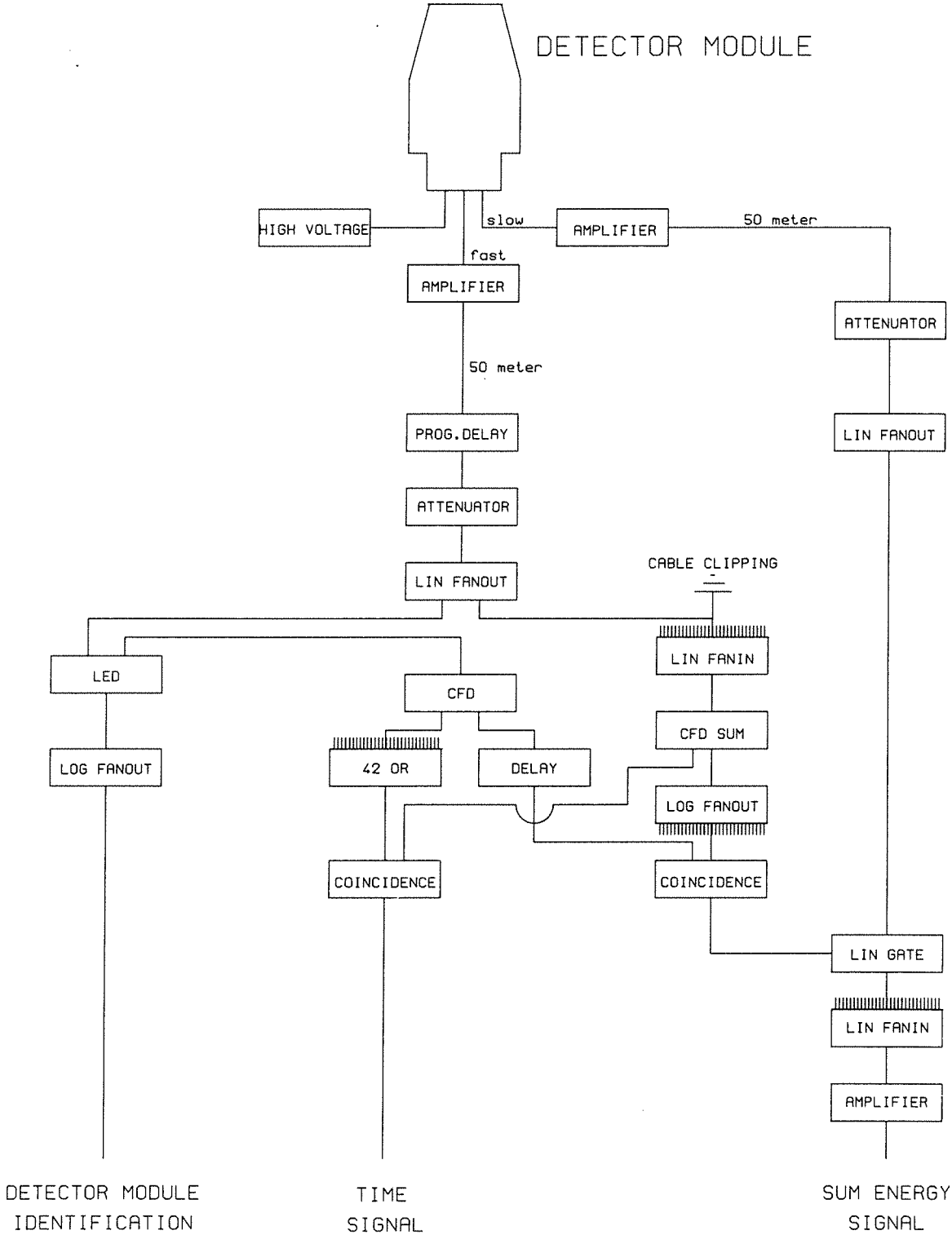

FIG.3 The relevant part of the electronics for signal processing (modules with 42 inputs or outputs are marked accordingly).

3 MeV in order to suppress low energy backgrounds. To this end, only the fast component of the scintillation light of all 42 detector modules is added in a linear fan-in module. The corresponding fast sum energy signal is 10 ns wide and carries still an energy resolution of ~15 % at 3 MeV gamma-ray energy. In principle, it is desirable to keep this threshold as low as possible, but due to the limited storage capacities of the magnetic tapes it has to be adjusted around 2.5 MeV. With this procedure, a master gate is produced, which opens the linear gates for those detector modules that have triggered the constant fraction discriminators (CFDs; threshold 50 keV). Then, the slow signals of these modules, which carry the energy information, pass the linear gates and are added in a linear fan-in module to a sum energy signal with good resolution. Simultaneously, a timing signal is derived from a fast 42-fold OR unit, which is fed by the CFDs of the individual detector modules. A leading edge discriminator produces a second logic signal for detector identification.

The complete detector is under computer control using CAMAC modules for constant fraction and leading edge discriminators, delays, high voltage power supplys, linear gates, scalers and multiplexers. This allows for automatic gain and delay adjustments, threshold settings, etc., via computer software. During the experiments, long term stability is maintained using the internal calibration provided by the α-lines from radium impurities in the crystals. These α-signals can easily be separated from gamma-ray events by a simple pulse shape analysis[24].

About 50% of the electronics is used for detector survey in order to ensure reliable long term operation. A generous fan-out capacity and a set of 6 multiplexers allow to observe all important signals of any detector module on oscilloscope, to determine the respective count rates, or to use them in further processing without disturbing data accquisition during an experiment[27].

The energy resolution of the sum energy signal is presented in Fig.4 at the example of spectra taken with calibrated sources. In the upper part, a peak efficiency of 93% is obtained for the ^{137}Cs line. For the higher energies of the ^{60}Co source (mid part of Fig.4), a peak efficiency of 82% is found. From the low intensity of the single lines in the cobalt spectrum, an escape probability of ~2% can be estimated for these energies. The high background in the spectrum measured with the (Pu+^{13}C) source (bottom) is caused by neutrons from the (α,n) reaction. As shown in the insert, the energy resolution follows the $1/\sqrt{E}$ law up to energies of ~3 MeV. The time resolution is shown in Fig.5 (for details see

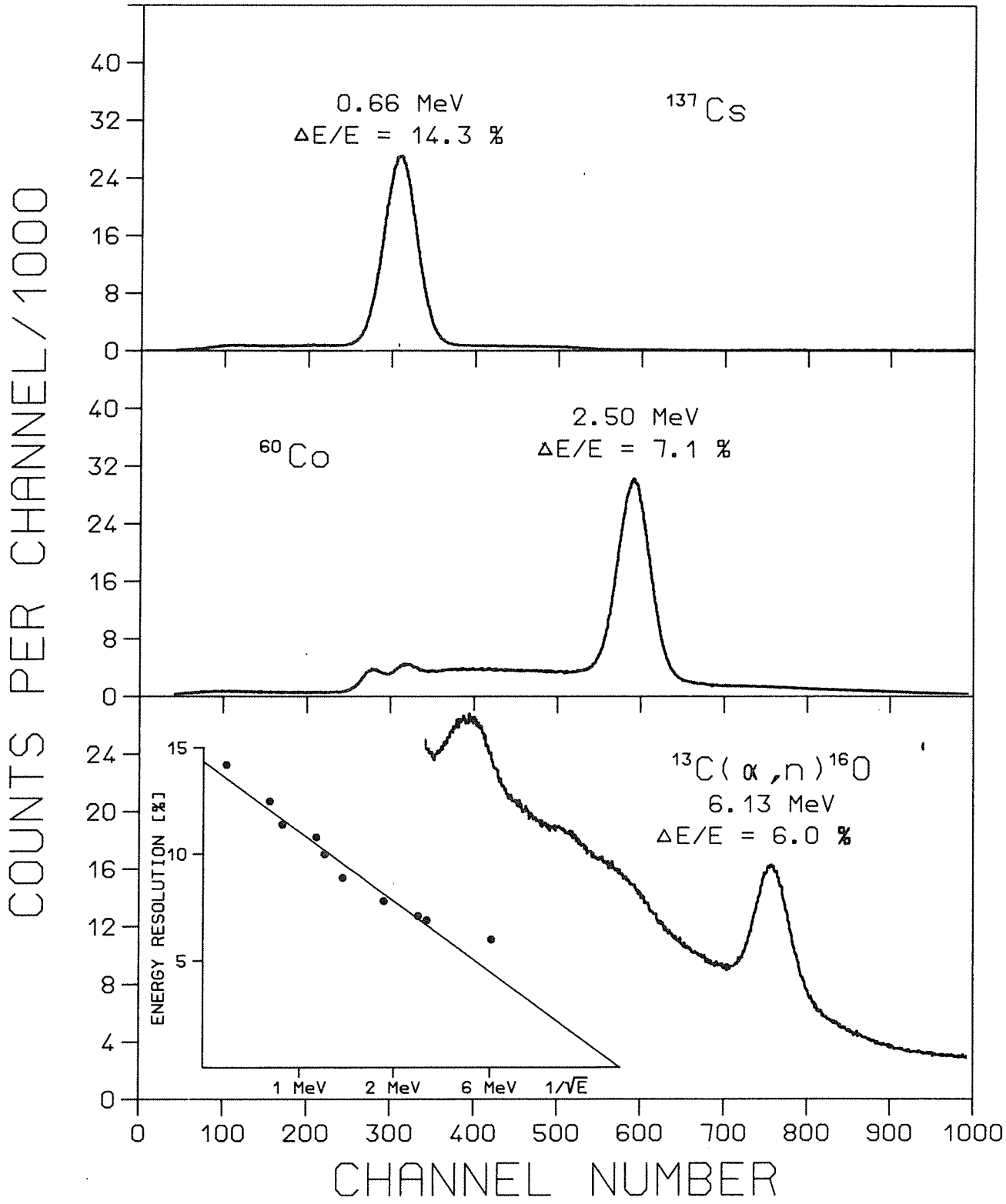

FIG.4 Energy resolution of the 4π detector in the gamma-ray energy range from 0.6 to 6.1 MeV (the large background in the lower spectrum is caused by neutrons from the (α,n) reaction).

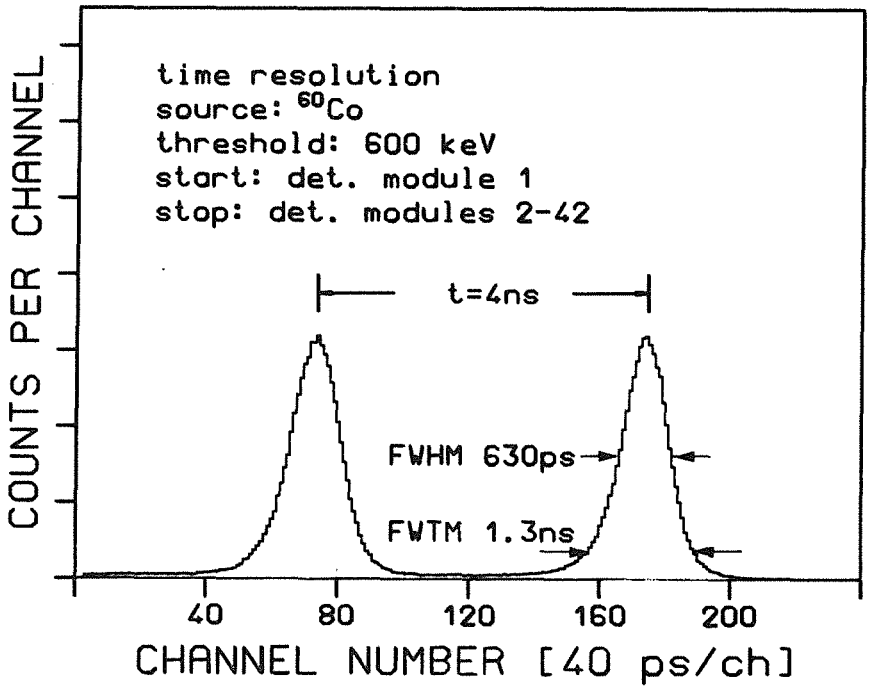

FIG.5 Time resolution of the 4π detector measured with a ^{60}Co source using one detector module for the START and the remaining 41 modules for the STOP signal in the time determination.

Ref.27); it was measured with a ^{60}Co source for two-fold coincidences using one detector module for the START and all other modules for the STOP signal.

During the experiments, each event is stored as a 64bit word in listmode on magnetic tape; this information is composed of sum energy (11bit), TOF (11bit), and detector identification (42bit). Simultaneously , a two-dimensional spectrum consisting of sum energy (7bit) versus TOF (11bit) is accumulated in a megastore device, and up to four one-dimensional control spectra are recorded by a separate increment unit. During the sample change (see below), a new listmode file for the next sample is created on magnetic tape and the two-dimensional spectrum is added to a sum file that is stored on disk for each sample separately. Also the control spectra are transferred to disk. The two-dimensional spectra are always available, containing the full statistical information for inspection and survey of the actual measurement. Data acquisition is performed with a 32 bit Data General MV4000 computer with 8 Mbyte memory, 760 Mbyte disk and two high speed, high density tapes. For detector survey, control, and stabilisation a 16 bit Data General NOVA4 computer with 1 Mbyte memory, 76 Mbyte disk, and 1600 bpi tape is used.

This first measurement has been performed with 40 instead of 42 detector modules with two free positions at the entrance and exit of the neutron beam. In this way, the solid angle covered by the detector is reduced to 95 % of 4π, affecting the efficiency and the shape of the capture gamma-ray spectrum (see section IV). Crystals with a central hole of 5 cm diameter will be available in future experiments to reduce these remaining gaps.

C. Monitor detectors

The measuring time necessary to accumulate sufficient statistical accuracy is about 1 to 2 weeks for each choice of the proton energy. Using the accumulated charge of the proton beam current for defining the measuring time per sample implies a systematic uncertainty: Since the neutron yield of the lithium target is slightly decreasing with time, the first sample in a cycle is irradiated with a systematically higher neutron flux compared to the last sample. To correct for this effect, we used the data measured with two ^{6}Li glass monitor detectors. A pulse height spectrum is recorded from detector 1 located inside the neutron collimator at a distance of ~20 cm from the neutron target. The signal from this detector corresponds to the integral neutron flux, but does not distinguish between time-correlated and moderated neutrons. Therefore, a TOF spectrum is accumulated with the monitor detector 2 in the direct neutron beam at a flight path of ~2.5 m, which determines the time correlated integral neutron flux. Since it is looking at the neutron target through the samples, its spectrum has to be corrected for the sample transmission; in general, these values are larger than 98 % (see section IV). The two monitor detectors offer an independent normalization of the integral neutron flux per sample.

D. Samples

A sample changer driven by a computer controlled stepping motor is installed at the detector. The samples are fixed on two parallel steel wires of 0.1 mm thickness at distances of 10 cm from each other. A set of 8 samples was mounted on the sample changer and moved cyclically into the measuring position in ~10 min intervals as defined by accumulating the proton beam current up to a preselected charge. In order to pass the sample changer vertically through the detector, a rectangular grove of 30×10 mm was milled in two opposite crystals and in the honeycomb structure. The important parameters of the samples are compiled in Table II .

TABLE II. Compilation of relevant sample data.

Sample[a]	Thickness [mm]	Thickness [10^{-3} A/barn]	Weight [g]	Purity [%]	Neutron Binding Energy [MeV]
1.) Au I	0.25	1.50994	1.8772	99.99	6.5127
2.) Graphite	0.50	4.0561	0.3075		
3.) Ta	0.15	0.8092	0.9242	99.9	6.0629
4.) Rh	0.10	0.79166	0.5142	99.9	6.9996
5.) Nb	0.50	2.8923	1.6961	99.9	7.2295
6.) Co	1.00	9.0032	3.349		7.4916
7.) Au II	0.25	1.50504	1.8711	99.99	6.5127
8.) no sample					

[a] Metallic samples of 22 mm diameter

In addition to the isotopes under investigation, i.e. ^{93}Nb, ^{103}Rh, and ^{181}Ta two identical ^{197}Au samples were used as cross section standards. The two gold samples allow to check the normalization to equal neutron flux and to verify the subtraction of the various background components. In addition, an empty position is used to determine the sample-independent background that is mainly due to the natural radioactivity and to neutrons escaping from the collimator or scattered in the air along the flight path. The transmission of 50 cm air equals that for the 0.3 mm gold samples; hence, air scattered neutrons cause a background that exceeds that from scattering in the gold samples. Therefore, an evacuated tube will be installed along the flight path in future experiments. Finally, a graphite sample is used to simulate the background from sample scattered neutrons, and a ^{59}Co sample serves for verification of the neutron energy scale via the positions of several well defined neutron resonances[35].

E. Measurements

Three experimental runs have been performed (Table III), two with a maximum neutron energy of 100 keV and one with 200 keV. In the first case, data were recorded in a TOF range of ~1.2 μs thus covering neutron energies down to ~2 keV. In these runs, the threshold

TABLE III. Parameters of the individual measurements.

Run	Flight path [mm]	Number of cycles	Maximum neutron energy [keV]	Measuring time [h]	Neutron flux [rel.units]
I	775.7	105	100	180	1.0
II	775.3	30	100	46	1.6
III	776.0	71	200	110	2.6

in the sum energy spectrum was adjusted at 2.6 MeV, yielding a total count rate of ~0.5 kHz. Most of the recorded events are due to background from the radium impurities in the BaF_2 crystals with sum energies below 3 MeV and multiplicities 1 and 2 (see section IV). In run III, the time interval for data acquisition was reduced to ~0.7 μs corresponding to a minimum neutron energy of ~6 keV; the sum energy threshold was lowered to 2.3 MeV yielding about the same integral countrate of 0.5 kHz. In the total measuring period of 2 weeks, 50 high density magnetic tapes were required containing a total information of ~5 Gbyte. Time and energy calibrations of the electronics were performed every second day.

IV. DATA EVALUATION

A. Processing of list mode data

In a first step, the list mode data stored on magnetic tape were converted into two-dimensional TOF versus sum energy spectra. In runs I and II, where a time range of 1.2 μs was covered, the spectra contained 2048 × 128 channels, while the shorter time range in run III required only 1024 × 128 channels. The respective calibrations were 0.72 ns/channel for the TOF and 86 keV/channel for the sum energy spectra. The event multiplicity was determined from the 42 bit pattern defining the involved detectors. Separate spectra were determined for events with multiplicities 1, 2, 3, 4 and ≧ 5; these five spectra per sample were found to be sufficient for further evaluation. In principle, spectra for higher multiplicities

could be considered as well; however, since spectra from eight samples are recorded simultaneously, data analysis would become increasingly time consuming.

True capture events are concentrated at higher multiplicities. In general about 50% of the capture events are observed in the spectrum with multiplicities ≧5, while only ~1 % have multiplicity 1. On the contrary, the background decreases rapidly with increasing multiplicity because it is dominated by the the radium impurities in the BaF_2 crystals; this component is concentrated in the spectra with multiplicity 1 and 2. Therefore, the small fraction of capture events observed with multiplicities 1 and 2 is difficult to determine. For the absolute normalization of the cross section, however, this contribution cannot be neglected. To improve the signal to background ratio in the spectra with low multiplicity, the sorting of list mode data was repeated by eliminating those events, where only neighboring detectors have fired. Events rejected in this way are with high probability due the background from radium impurities, which is dominated above 2 MeV by the decays of ^{214}Bi and ^{208}Tl, where an electron is emitted in prompt coincidence with one or two gamma-rays ; these events have a high probability for triggering two or three neighboring detector modules. This selection criterion also removed background events due to neutron captures in the scintillator, since the capture cascade originates inside a detector module. In contrast, there is only a very small probability that all gamma-rays from true capture events in the sample should be absorbed in neighboring detector modules.

With this additional criterion, ~70% of the low energy background in the spectra with multiplicity 2, and 40% in the spectra with multiplicity 3 could be rejected. It also eliminates ~50% of the background from scattered neutrons, whereas only ~2% of the true capture events are lost. In order to ensure that this criterion does not systematically affect the results, the complete data evaluation was performed twice using the original data as well (section V). The signal to background ratio as a function of multiplicity is illustrated in Appendix A at the example of the two-dimensional spectra measured with the gold and rhodium samples. The spectra contain the combined data of runs I and II compressed into 64X64 channels. Further improvements of the signal to background ratio will be discussed in section VIII.

B. Normalization to equal neutron flux

Due to the cyclic transfer of the samples into the measuring position in the centre of the

TABLE IV. Transmission of the samples

Sample	Neutron energy range [keV]			
	15-30	30-50	50-80	80-160
Au	0.9799	0.9819	0.9834	0.9853
Nb	0.9760	0.9757	0.9752	0.9737
Rh	0.9933	0.9931	0.9928	0.9924
Ta	0.9905	0.9915	0.9922	0.9931
C	0.9813	0.9815	0.9819	0.9826

detector and due to the decrease of the neutron yield with time, the first sample in a cycle is exposed to a slightly higher neutron dose than the last sample. The corresponding correction factors have been calculated in two independent ways. First, the peak in the analog spectrum recorded from the monitor detector 1 was integrated and the results were compared for the different samples. Secondly, the TOF spectrum measured with monitor 2 was divided into four energy bins, the respective integrated rates were corrected for the transmission (Table IV), and the results were again compared for the different samples. The two completely independent procedures yielded consistent results within uncertainties (section VI). The averaged corrections from both procedures, which are smaller than ~0.5%, were finally adopted in further analysis.

C. Sample-Independent background

At first, the spectrum recorded with the empty position of the sample changer was subtracted from the other spectra for the recorded five multiplicities separately. By this procedure all time-dependent and time-independent backgrounds correlated with the neutron source were considered; these are mainly due to capture of moderated neutrons, escaping from the collimator, and to capture of neutrons scattered in the air along their flight path. Simultaneously, the overwhelming part of the time-independent background due to natural radioactivity and to gamma-rays from the collimator is eliminated, too. However, minor parts of these background components are still present or have been overcompensated, since the

spectra have been normalized to equal neutron intensity and not to equal time or beam current.

In a second step, this remaining time-independent background was removed from the specta by integrating a time interval of ~100 ns prior to the prompt gamma-ray peak corresponding to neutron flight times of 3.9 μs. According to Monte Carlo studies[27], no time-dependent effects are expected at such long flight times. This was verified experimentally by dividing that interval in two equal parts: the respective integrated count rates were indeed equal. These corrections are demonstrated for the gold and the rhodium samples in the upper and middle part of Figs. 6a and 6b. Now, the capture events concentrated at a sum energy of 6.5 and 7.0 MeV, respectively, and the remaining background due to capture of sample scattered neutrons concentrated around 9 MeV can clearly be distinguished.

D. Sample scattered neutrons

The projection of a background corrected spectrum measured with the graphite sample is shown in Fig. 7. Since neutron capture in carbon can be neglected, the spectrum contains only events due to capture of sample scattered neutrons in the scintillator. Capture in ^{135}Ba and ^{137}Ba with binding energies of 9.11 MeV and 8.61 MeV, respectively, dominates the spectrum. A considerably smaller effect is due to ^{134}Ba and ^{136}Ba (6.97 and 6.90 MeV binding energies), whereas the contribution from ^{138}Ba at 4.72 MeV is almost negligible. Capture events in fluorine should show up at 6.60 MeV, but cannot be identified. The observed intensity ratios correspond in good approximation to those of the products, isotopic abundance times capture cross section, at 30 keV (Ref. 5), which are:

$$N\sigma(^{138}Ba) : N\sigma(^{134,136}Ba) : N\sigma(^{135,137}Ba) = 6\% : 21\% : 73\%.$$

Fig. 7 demonstrates the low sensitivity of BaF_2 crystals for neutron experiments due to the very small capture cross sections of the most abundant isotopes ^{138}Ba and ^{19}F. Since the neutron binding energies of the investigated nuclei are between 6.0 and 7.2 MeV, only a small part of the background from sample scattered neutrons is disturbing the true capture events.

For subtraction of this background, the two-dimensional spectra of sample and graphite sample were projected on the TOF axis in the sum energy range of the ^{135,137}Ba peak (e.g. in the shaded region from channel 91 to 112 in the spectrum of Fig. 7), well above the binding energies of the measured isotopes. The observed ratio of the counts in the two

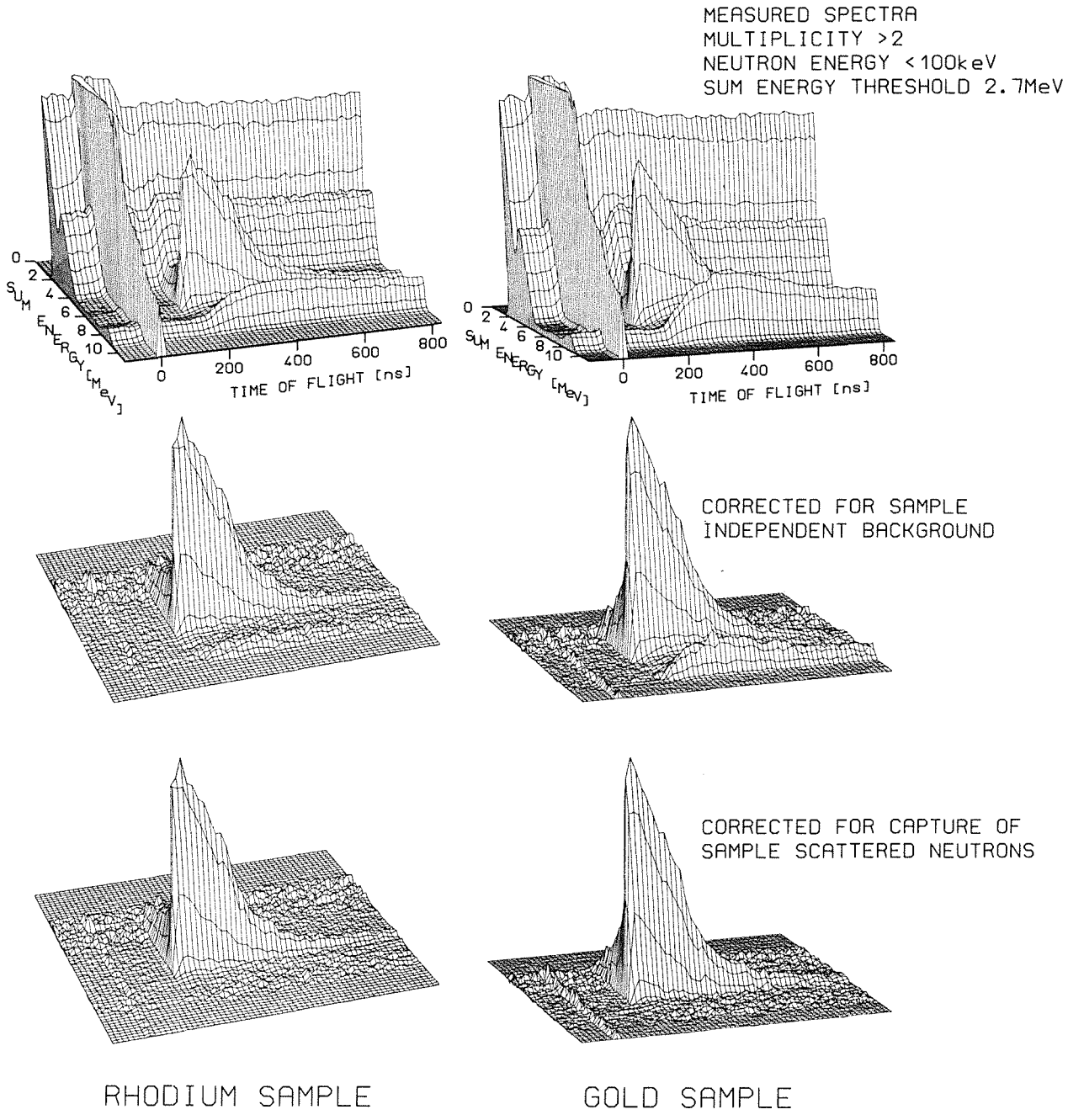

FIG.6a The different steps of background subtraction demonstrated with the example of the gold and rhodium samples. The spectra contain the summed data of runs I and II with a maximum neutron energy of 100 keV (multiplicity ≧3).

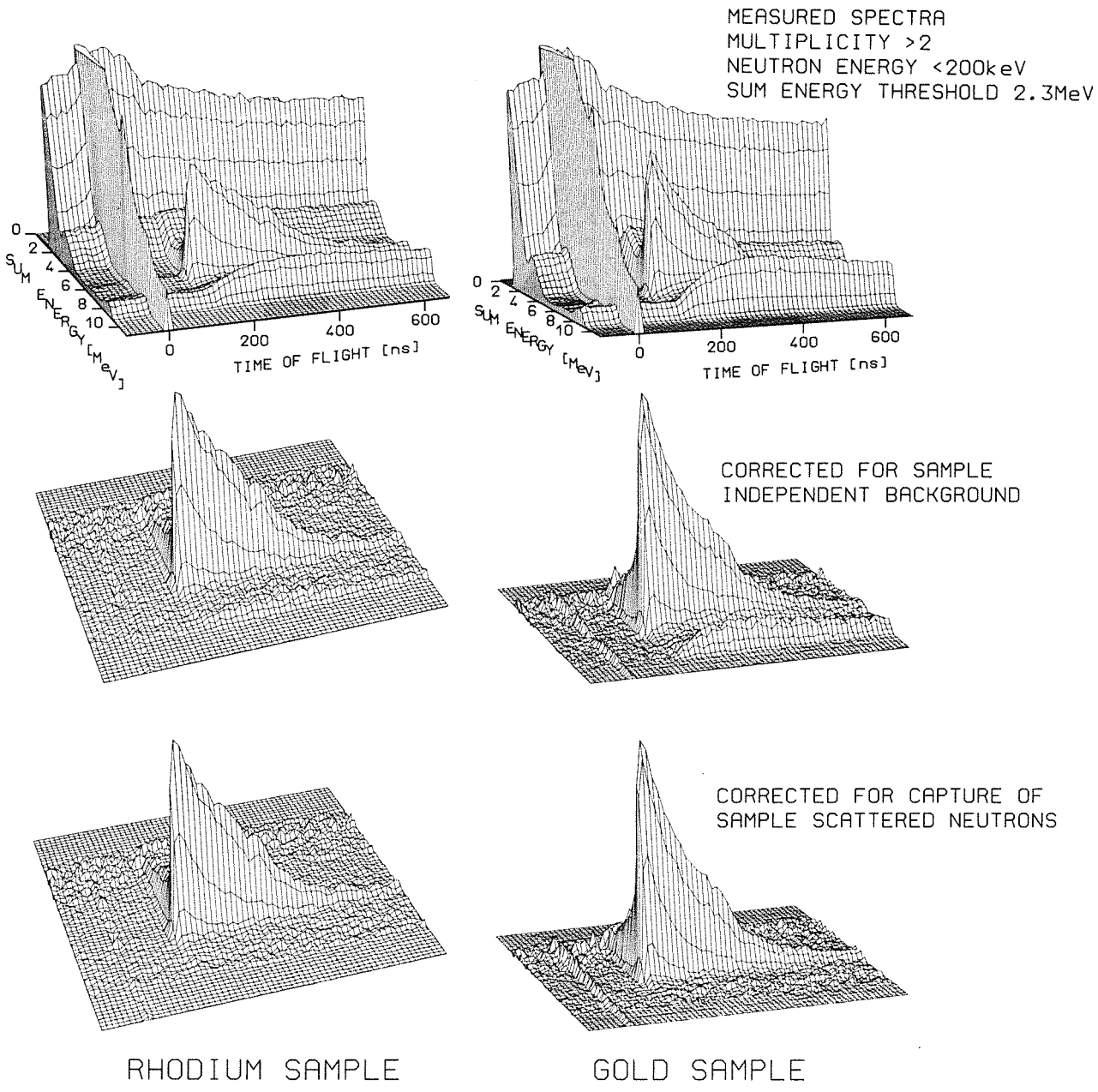

FIG.6b The same as Fig.6a but for run III with maximum neutron energy of 200 keV.

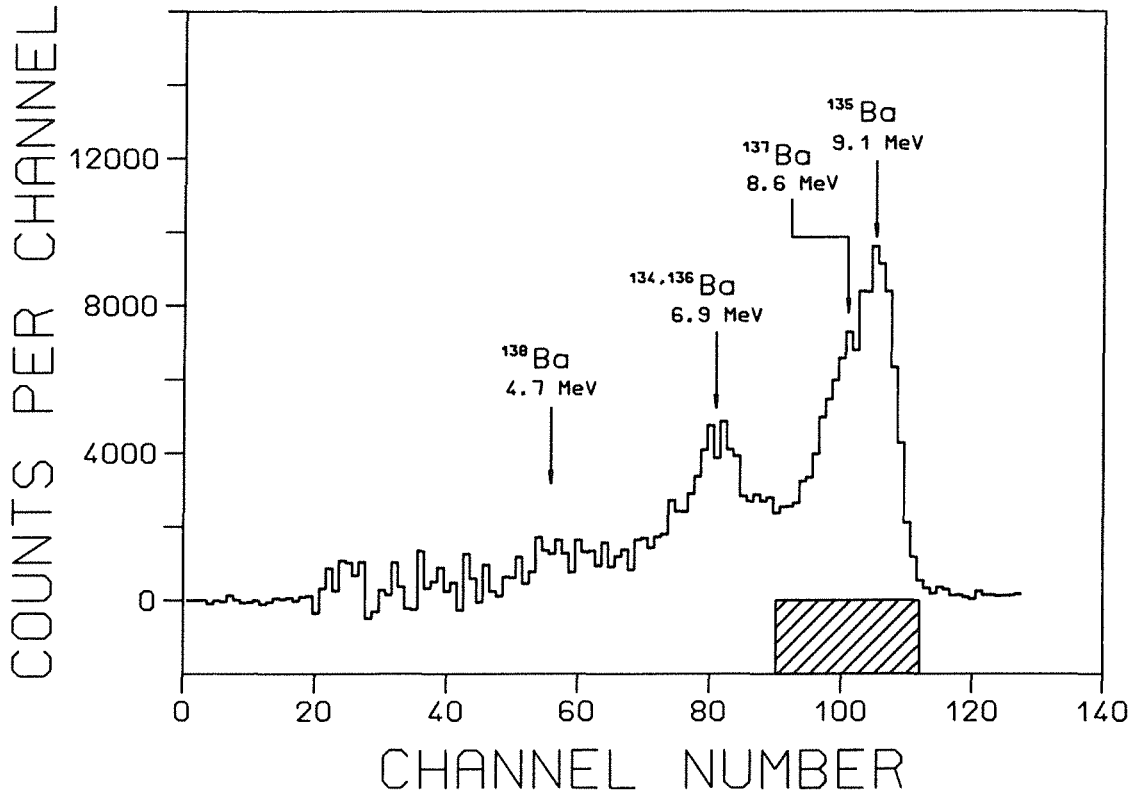

FIG.7 Sum energy spectrum measured with the graphite sample, showing the energy distribution due to neutron capture in the BaF_2 scintillator. The dashed energy range was used to determine the normalization factor for background subtraction (see Fig.8).

spectra was used to normalize the graphite spectrum correctly prior to its subtraction from the spectrum of the respective sample. As shown in Fig. 8, this ratio depends on neutron energy (or TOF); accordingly, an energy dependent normalization factor was applied.

In previous experiments with Moxon-Rae or C_6D_6 detectors, the respective correction factors could not be determined as a function of neutron energy. Therefore, the spectrum measured with the carbon sample was always normalized with a constant factor determined from the time-independent count rate at long flight times. While this is a good approximation for gold and tantalum (Fig. 8), it leads to unaccounted systematic uncertainties for the other samples. For the first time, the energy resolution obtained in the present experiment allows to determine this background in the energy range of interest reliably including its correct energy dependence. The only assumption that still has to be made is that this ratio for neutrons scattered from the sample or from graphite is equal for the odd and even barium isotopes. The final, background corrected spectra are shown in the lower part of Figs. 6a and 6b.

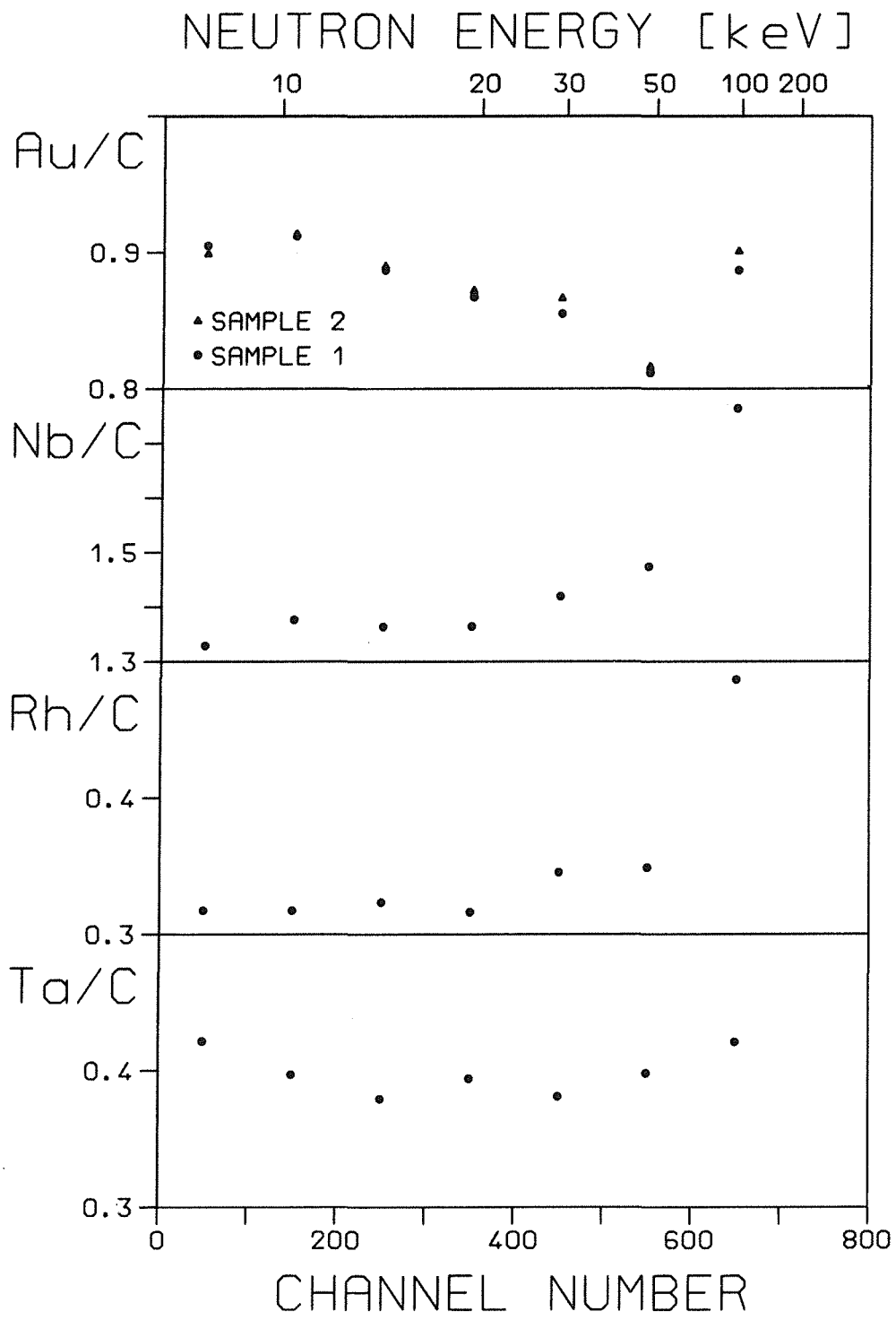

FIG.8 Ratio of capture events in the scintillator due to neutrons scattered in the different samples and in the graphite sample determined by integrating the two-dimensional spectra in the region around 9 MeV (see Fig. 7).

E. Determination of the cross section shape

In Fig. 9 the sum energy spectra of gold and rhodium are plotted for different multiplicities. These spectra are obtained by projecting the two-dimensional distributions in the TOF range with optimum signal to background ratio (see part F below). For the determination of the cross section shape, the two-dimensional distributions were projected on the TOF axis in selected energy regions around the binding energy as indicated by arrows in Fig. 9 to obtain favorable signal to background ratios. After summation over all multiplicities, the resulting one-dimensional TOF spectrum is shown in full time resolution in Fig. 10. For comparison, this figure contains also the background due to capture of sample scattered neutrons that has been subtracted before. The time shift between the primary capture events and the delayed background is clearly visible. This delay leaves the neutron energy interval from 150 to 200 keV completely undisturbed. In contrast to the sharp onset of the capture events, the background is spread in time due to the fact that the neutrons are scattered 20 times on average before they are captured in the scintillator. Fig. 10 demonstrates that a signal to background ratio larger than one is obtained down to neutron energies around 10 keV; better signal to background ratios at low neutron energies are obtained in runs I and II with a maximum neutron energy of 100 keV.

At this point it should be mentioned that the use of NaI(Tl) as a detector material is completely ruled out for measurements in the keV neutron energy range. As calculated in Ref. 27, in this case more than 60% of the neutrons are captured in the scintillator after a few scattering interactions without significant delay. Since the binding energy of iodine is the same as for gold, these events cannot be separated from true capture events in the sum energy spectrum. The ratio of scattering to capture cross section in gold being ~20 implies that the background dominates by a factor of 10 over the true capture events. For keV neutron energies it is impossible to shield the scattered neutrons from the detector without destroying the energy resolution and hence the well defined detector efficiency (see part F below).

F. Absolute normalization of the cross sections

For absolute normalization, the total efficiency for capture events has to be determined. For this purpose, the sum energy spectra were projected in the TOF region with optimum signal to background ratio as indicated by the shaded region in Fig. 10, e.g. between channels 600

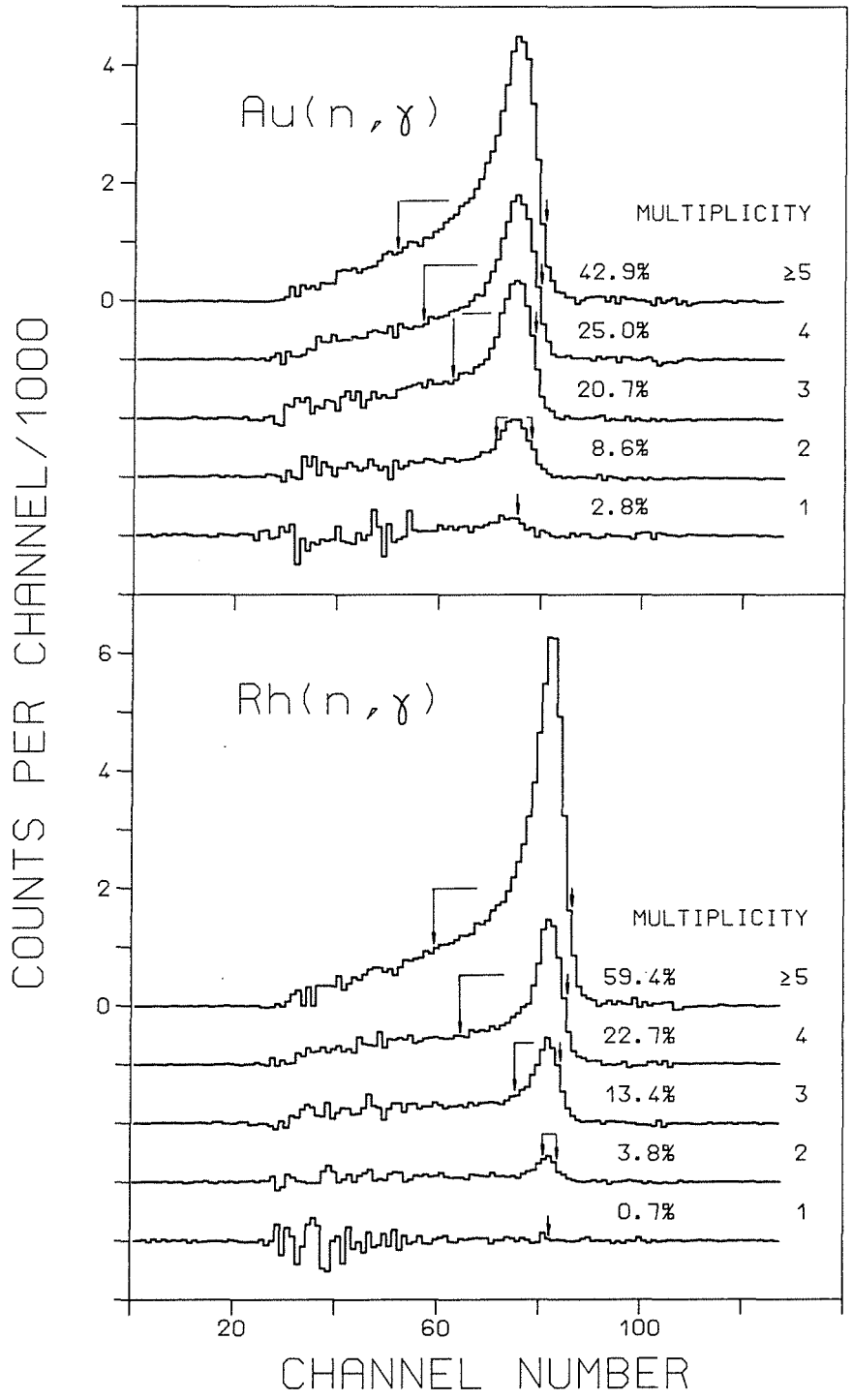

FIG.9 Sum energy spectra of gold and rhodium as a function of multiplicity. The regions used for determination of the cross section shape are indicated by arrows.

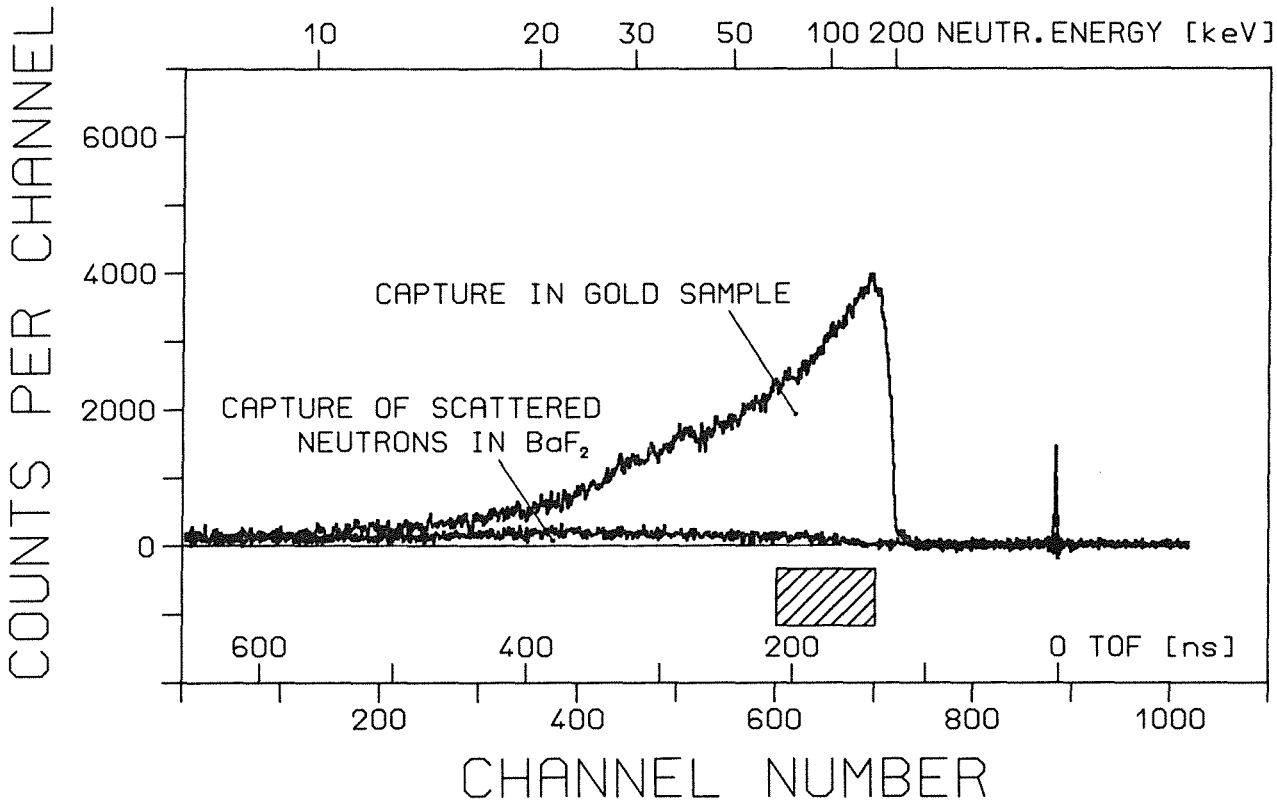

FIG.10 TOF spectrum used for the determination of the cross section shape. The region for absolute normalization is shaded.

and 699. The resulting spectra are shown in Fig. 9 . The total detector efficiency can be determined from these spectra after correction for the number of events falling below the experimental thresholds of 2.3 or 2.6 MeV (see part G below).

It is obvious from Fig. 9 that the number of capture events in the spectrum with multiplicity 1 is difficult to define at low sum energies due to statistical fluctuations. To reduce this problem, the ratio of the integrated count rates of these spectra and of the respective count rates at high sum energies, where statistics are much better, i.e. above channel 54, was plotted for all higher multiplicities. The resulting distribution was then extrapolated to multiplicity 1. In this way, a somewhat better accuracy was obtained for the normalization factor.

The cross section ratio of isotope X relative to the gold standard is then:

$$\frac{\sigma_i(X)}{\sigma_i(Au)} = \frac{Z_i(X)}{Z_i(Au)} \times \frac{\Sigma Z(Au)}{\Sigma Z(X)} \times \frac{\Sigma E(X)}{\Sigma E(Au)} \times \frac{m(Au)}{m(X)} \times F_1 \times F_2 \qquad (1)$$

In this relation, Z_i is the countrate in channel i of the TOF spectrum, ΣZ is the integral TOF count rate in the interval used for normalization (see Fig.10), ΣE is the total count rate in the sum energy spectrum for all multiplicities summed over the normalization interval (see Fig. 9), and m is the sample mass. The correction factor F_1 is the ratio of the capture events below the threshold for sample and reference sample (section G), and F_2 the respective ratio of the multiple scattering corrections (section H).

G. Correction for capture events below the experimental threshold

In the sum energy spectra for normalization of the cross section, $\Sigma E(X)$ (Fig. 9), a certain fraction of capture events falls below the electronic threshold of 2.3 or 2.6 MeV. This unobserved part may be different for sample and reference sample according to the differences in binding energies, capture gamma-ray spectra, and average cascade multiplicities. This difference is taken into account by the correction factor

$$F_1 = \frac{100 - f(Au)}{100 - f(X)}$$

where f is the fraction of unobserved events in (%).

F_1 has been calculated as described previously[8]. For this purpose two informations are necessary: the individual neutron capture cascades and their relative contribution to the total capture cross section as well as the detector efficiency for monoenergetic gamma-rays in the energy range up to 10 MeV.

The capture cascades and capture gamma-ray spectra of the involved isotopes have been calculated according to the statistical and optical model as discussed in detail in Ref. 7. Meanwhile, the computer codes have been modified to yield the energies for the individual gamma-rays as well as the partial capture cross sections related with the possible gamma-ray cascades. For illustration, these data are presented in Table V for the 20 most probable cascades, but in the following calculations all cascades necessary to account for 95% of the total capture cross section were considered. Depending on the level densities, the partial cross sections per cascade can be very different for the investigated isotopes. In case of gold, only 10% of the capture cross section are covered by the 20 most probable cascades; consequently, more than 4000 cascades are necessary to cover 95% of the gold cross section. For rhodium, the corresponding numbers are 40% and only ~300 cascades.

TABLE V. Calculated capture gamma-ray cascades including multiplicities, partial cross sections, σ_p, and gamma-ray energies of the 20 most significant cascades.

Gold

σ(30 keV)=0.590 b	total capture cross section
σ(mul 1)=0.0049 b	
σ(mul 2)=0.0495 b	
σ(mul 3)=0.1434 b	
σ(mul 4)=0.1689 b	average multiplicity <m>=4.2
σ(mul 5)=0.1219 b	
σ(mul 6)=0.0714 b	
σ(mul 7)=0.0300 b	

calculated number of cascades: 4447

σ_p [mbarn]	σ_p/σ_{tot} [%]	gamma1	gamma2	gamma3 [MeV]	gamma4	gamma5
4.94	0.84	6.542				
4.51	0.76	6.487	0.055			
3.96	0.67	5.366	1.176			
3.63	0.62	6.281	0.261			
3.44	0.58	6.214	0.328			
3.40	0.57	6.306	0.236			
3.40	0.57	6.144	0.398			
3.16	0.53	2.981	3.561			
3.10	0.52	3.577	2.965			
2.98	0.50	4.770	1.772			
2.96	0.50	4.174	2.368			
2.87	0.48	2.385	4.154			
2.82	0.48	5.366	1.121	0.055		
2.59	0.44	6.283	0.168	0.036	0.055	
2.48	0.42	2.981	3.506	0.055		
2.46	0.42	6.195	0.292	0.055		
2.39	0.41	3.577	2.910	0.055		
2.28	0.39	2.385	4.102	0.055		
2.24	0.38	4.174	2.314	0.055		
2.20	0.37	4.770	1.717	0.055		
	Σ 10.5%					

TABLE V. (continued)

Niobium

σ(30 keV)=0.258 b	total capture cross section
σ(mul 1)=0.0050 b	
σ(mul 2)=0.0396 b	
σ(mul 3)=0.0866 b	
σ(mul 4)=0.0821 b	average multiplicity <m>=3.5
σ(mul 5)=0.0364 b	
σ(mul 6)=0.0083 b	
σ(mul 7)=0.0000 b	

calculated number of cascades: 584

σ_p [mbarn]	σ_p/σ_{tot} [%]	gamma1	gamma2	gamma3 [MeV]	gamma4	gamma5
4.10	1.59	7.146	0.113			
3.81	1.48	4.025	3.234			
3.79	1.47	4.830	2.370	0.018		
3.76	1.46	4.025	3.121	0.113		
3.73	1.45	5.635	1.565	0.018		
3.68	1.42	7.201	0.018			
3.67	1.42	4.830	2.429			
3.65	1.41	4.830	2.316	0.113		
3.64	1.41	4.025	3.175	0.018		
3.60	1.40	6.947	0.253	0.018		
3.33	1.29	3.220	4.039			
3.27	1.27	3.220	3.926	0.113		
3.21	1.24	5.635	1.624			
3.21	1.24	7.259				
3.18	1.23	5.635	1.511	0.113		
3.02	1.17	3.220	3.980	0.018		
2.91	1.13	4.025	2.922	0.253	0.018	
2.69	1.04	5.635	1.583			
2.67	1.03	3.220	2.117	0.253	0.018	
2.58	1.00	4.830	2.117	0.253	0.018	
	Σ=26.2%					

TABLE V. (continued)

Rhodium

σ(30 keV)=0.861 b — total capture cross section
σ(mul 1)=0.0027 b
σ(mul 2)=0.0387 b
σ(mul 3)=0.1971 b
σ(mul 4)=0.3607 b — average multiplicity <m>=4.0
σ(mul 5)=0.2108 b
σ(mul 6)=0.0510 b
σ(mul 7)=0.0000 b

calculated number of cascades: 328

σ_p [mbarn]	σ_p/σ_{tot} [%]	gamma1	gamma2	gamma3 [MeV]	gamma4	gamma5
36.7	4.26	5.948	1.030	0.051		
34.3	3.98	5.099	0.850	1.030	0.051	
33.3	3.87	4.249	1.700	1.030	0.051	
28.7	3.34	3.399	2.549	1.030	0.051	
20.2	2.34	2.549	3.399	1.030	0.051	
18.9	2.20	5.948	0.895	0.186		
17.0	1.97	5.099	0.850	0.895		
16.0	1.86	4.249	1.700	0.895	0.186	
15.1	1.75	3.399	1.699	0.850	1.030	0.051
14.3	1.66	2.549	2.549	0.850	1.030	0.051
13.6	1.58	3.399	2.549	0.895	0.186	
13.2	1.53	5.948	1.081			
10.2	1.19	4.249	0.850	0.850	1.030	0.051
10.2	1.18	1.700	4.249	1.030	0.051	
9.56	1.11	2.549	3.399	0.895	0.186	
9.36	1.09	5.099	0.850	1.081		
9.32	1.08	4.249	1.700	1.081		
8.66	0.97	1.700	3.399	0.850	1.030	0.051
8.32	0.97	5.099	1.880	0.051		
8.20	0.95	3.399	2.549	1.081		
	Σ=38.9%					

TABLE V. (continued)

Tantalum

σ(30 keV)=0.749 b — total capture cross section
σ(mul 1)=0.0036 b
σ(mul 2)=0.0530 b
σ(mul 3)=0.2040 b
σ(mul 4)=0.2704 b — average multiplicity <m>=3.9
σ(mul 5)=0.1649 b
σ(mul 6)=0.0531 b
σ(mul 7)=0.0000 b

calculated number of cascades: 2124

σ_p [mbarn]	σ_p/σ_{tot} [%]	gamma1	gamma2	gamma3 [MeV]	gamma4	gamma5
6.18	0.83	2.772	3.321			
5.79	0.77	2.772	3.224	0.098		
5.67	0.76	2.772	3.207	0.114		
5.65	0.75	3.465	2.629			
5.24	0.70	2.772	2.079	1.243		
5.03	0.67	3.465	2.531	0.098		
4.98	0.66	2.079	2.772	1.243		
4.90	0.65	3.465	2.515	0.114		
4.60	0.61	2.079	4.014			
4.41	0.59	2.079	3.917	0.098		
4.33	0.58	2.079	3.900	0.114		
4.21	0.56	4.157	1.936			
4.08	0.54	2.079	2.079	1.936		
3.39	0.45	4.157	1.838	0.098		
3.33	0.44	4.850	1.243			
3.27	0.44	4.157	1.822	0.114		
3.19	0.43	3.465	1.386	1.243		
3.18	0.42	2.772	3.172	0.133		
3.18	0.42	2.079	2.079	1.838	0.098	
3.13	0.42	2.772	2.079	1.145	0.098	
	Σ=11.7%					

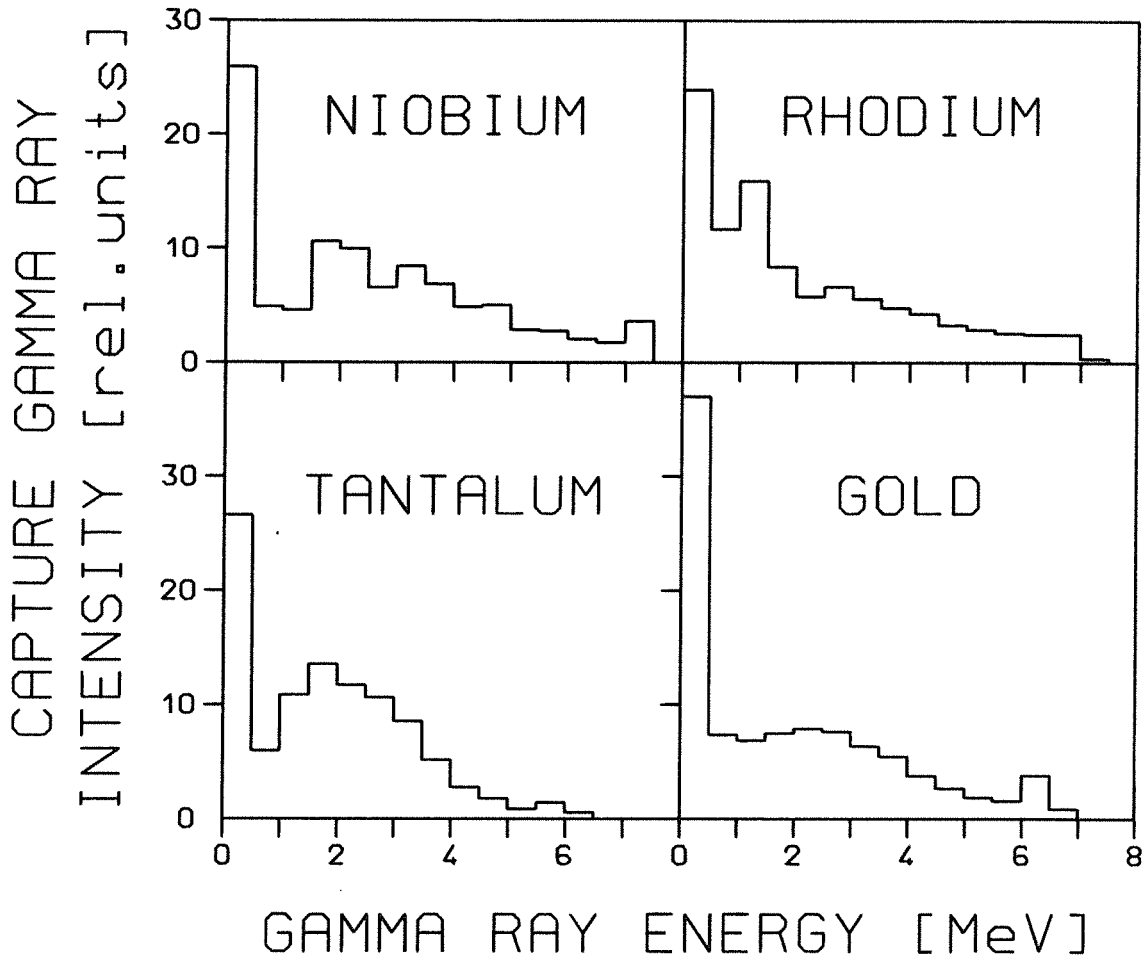

FIG.11 Calculated capture gamma-ray spectra for neutron capture in ^{93}Nb, ^{103}Rh, ^{181}Ta and ^{197}Au.

The average multiplicities are surprisingly constant and vary between 3.6 and 4.2. The respective capture gamma-ray spectra are shown in Fig. 11.

The efficiency for monoenergetic gamma-rays of a spherical BaF_2 shell with 20 cm inner diameter and 15 cm thickness was calculated analytically up to 10 MeV as described in Refs. 8 and 37. These calculations have been performed with different assumptions for multiple Compton events resulting in an optimistic and a pessimistic estimate for the peak efficiency SW(MAX) and SW(MIN). The respective values in the energy range between 0.5 and 10 MeV are compiled in Table VI, containing 20 bins for each gamma-ray energy. Measurements of the detector efficiency[27] with calibrated sources showed that the actual efficiency can be approximated by

$$EFF = {}^{2}/_{3}\ SW(MAX) + {}^{1}/_{3}\ SW(MIN). \qquad (2)$$

TABLE VI. Calculated probability SW for the detection of monoenergetic gamma-rays in a spherical BaF_2 detector with 20 cm inner diameter and 15 cm thickness[a].

Gamma-ray energy [MeV][b]	Probability SW(MAX) [%]									
0.5	0.1711	0.0359	0.0250	0.0168	0.0110	0.0069	0.0044	0.0030	0.0023	0.0022
	0.0032	0.0053	0.0094	0.0134	0.0099	0.0047	0.0000	0.0000	0.0000	99.6755
1.0	1.8339	0.2942	0.2561	0.2200	0.1867	0.1571	0.1316	0.1112	0.0966	0.0897
	0.0911	0.1042	0.1311	0.1819	0.2815	0.4691	0.3923	0.1214	0.0000	94.8503
2.0	5.6913	0.5577	0.5250	0.4946	0.4654	0.4388	0.4165	0.4002	0.3913	0.3899
	0.3970	0.4170	0.4547	0.5187	1.3639	0.8147	1.2008	1.9714	0.8336	82.2575
3.0	7.6931	0.5394	0.5234	0.5087	0.4967	0.4881	0.4833	0.4816	0.4840	0.4911
	0.5043	0.5261	0.5603	0.6141	0.7035	0.8560	3.5467	1.8422	2.6358	76.0216
4.0	8.5480	0.4659	0.4585	0.4532	0.4508	0.4513	0.4543	0.4604	0.4697	0.4828
	0.5007	0.5246	0.5577	0.6047	0.6760	0.7948	1.0197	5.2913	3.0253	74.3103
5.0	8.8495	0.3945	0.3918	0.3913	0.3932	0.3973	0.4038	0.4127	0.4248	0.4401
	0.4595	0.4845	0.5171	0.5604	0.6218	0.7176	0.8921	4.0803	4.4933	74.6744
6.0	8.8608	0.3342	0.3341	0.3357	0.3395	0.3450	0.3526	0.3623	0.3747	0.3902
	0.4097	0.4343	0.4654	0.5060	0.5614	0.6428	0.7810	1.0810	7.3272	75.7621
7.0	8.7099	0.2850	0.2864	0.2894	0.2939	0.3002	0.3081	0.3178	0.3302	0.3455
	0.3644	0.3884	0.4187	0.4577	0.5098	0.5838	0.7033	0.9522	7.3561	76.7991
8.0	8.4663	0.2446	0.2468	0.2503	0.2551	0.2612	0.2688	0.2783	0.2898	0.3041
	0.3218	0.3438	0.3720	0.4081	0.4560	0.5221	0.6239	0.8229	7.2049	78.0592
9.0	8.1707	0.2115	0.2140	0.2177	0.2224	0.2284	0.2356	0.2444	0.2552	0.2685
	0.2847	0.3052	0.3310	0.3642	0.4082	0.4683	0.5574	0.7220	7.0404	79.2502
10.0	7.8480	0.1841	0.1867	0.1904	0.1951	0.2007	0.2075	0.2158	0.2258	0.2381
	0.2533	0.2721	0.2960	0.3268	0.3672	0.4224	0.5029	0.6433	3.5425	83.6813
	Probability SW(MIN) [%]									
0.5	0.1711	0.0769	0.1368	0.2337	0.3660	0.5303	0.7217	0.9360	1.1672	1.4194
	1.7027	2.0660	2.6238	3.3221	2.7216	1.5047	0.2409	0.0004	0.0000	80.0527
1.0	1.8366	0.3141	0.3124	0.3360	0.3899	0.4793	0.6107	0.7936	1.0365	1.3525
	1.7586	2.2826	2.9577	3.8658	5.2078	7.5358	8.5571	4.0625	0.1300	56.1804
2.0	5.6920	0.5631	0.5417	0.5282	0.5260	0.5387	0.5714	0.6306	0.7255	0.8985
	1.1996	1.4926	1.9184	2.5423	4.3833	6.3072	8.8997	14.8758	10.5226	36.6428
3.0	7.6933	0.5415	0.5292	0.5213	0.5199	0.5268	0.5444	0.5749	0.6220	0.6932
	0.7979	0.9521	1.1850	1.9644	2.5845	3.5579	10.1452	14.1537	21.2665	30.6263
4.0	8.5481	0.4668	0.4613	0.4590	0.4617	0.4695	0.4836	0.5055	0.5373	0.5834
	0.6496	0.7451	0.8885	1.1116	1.5941	2.9217	4.1669	17.1832	25.5998	32.1633
5.0	8.8495	0.3950	0.3932	0.3944	0.3991	0.4071	0.4194	0.4371	0.4616	0.4954
	0.5423	0.6088	0.7072	0.8569	1.1008	1.7500	3.5088	9.7869	30.8750	37.6116
6.0	8.8608	0.3346	0.3348	0.3377	0.3429	0.3509	0.3621	0.3772	0.3973	0.4245
	0.4615	0.5128	0.5864	0.6975	0.8779	1.1958	2.5016	4.6917	33.2366	43.1154
7.0	8.7099	0.2856	0.2869	0.2906	0.2961	0.3039	0.3141	0.3274	0.3447	0.3675
	0.3977	0.4395	0.4982	0.5851	0.7226	0.9618	1.4731	4.1654	30.2967	48.9332
8.0	8.4663	0.2448	0.2471	0.2510	0.2565	0.2636	0.2728	0.2844	0.2993	0.3185
	0.3437	0.3776	0.4249	0.4939	0.6008	0.7838	1.1468	3.0057	25.7021	56.2164
9.0	8.1707	0.2116	0.2142	0.2183	0.2234	0.2302	0.2384	0.2490	0.2623	0.2792
	0.3012	0.3306	0.3710	0.4292	0.5194	0.6717	0.9718	2.2800	19.9102	63.9176
10.0	7.8481	0.1841	0.1869	0.1908	0.1957	0.2020	0.2095	0.2190	0.2308	0.2457
	0.2648	0.2902	0.3246	0.3735	0.4475	0.5707	0.8100	1.5209	12.0925	73.5927

[a] The calculation was performed with two differnt assumptions on the detection probability of multi-scattering Compton events,SW(MIN) and SW(MAX).

[b] Each gamma-ray energy is divided into 20 equal bins.

Using the above informations, the sum energy spectrum of the detector was calculated in the following way: The registration probability for each gamma-ray of a capture cascade was calculated as a function of energy in 20 energy bins by linear interpolation of the values given in Table VI . Then, the sum energy spectrum was determined for each cascade, and the final spectrum was obtained by summation of the individual spectra according to their partial capture cross sections.

In the calculation it was taken into account that only 40 out of 42 detector modules were actually installed. Allowing in addition for 1% losses through the gaps between the BaF_2 crystals, only 94% of 4π were covered by active material. Gamma-rays below 50 keV were rejected to account for the electronic thresholds. The calculated results for the fraction f of events below threshold energies of 2.0, 2.5 and 3.0 MeV in the sum energy spectrum are given in Table VII for the two estimates of the peak efficiency. The final correction factors F_1 were calculated as the mean of the two possibilities and were interpolated to the actual threshold energies. For comparison, the corresponding f values for an ideal 4π detector (full solid angle, no electronic thresholds) are given as well.

In the present first experiment, the design value of 95% efficiency could not be reached. In future, two additional crystals with a central hole of 50 mm diameter will be introduced at the neutron beam entrance and exit, which will cover 80% of the space presently not filled by detector material. Moreover, the 7 crystals with the largest radium content have been replaced, thus reducing the correlated background by 40%. With these improvements, it will be possible to increase the total efficiency finally up to values of 97 to 98 %.

In Fig. 12 the calculated sum energy spectra for gold and rhodium are displayed separarely for the two different assumptions of the detector efficiency. Comparison with the experimental results of Fig. 9 shows them to lie between these two extreme values, but somewhat closer to SW(MIN). This means that the resolution for capture cascades is slightly worse compared to that for monoenergetic gamma-rays (Eq. 2)[27]. Therefore, F_1 was determined using the mean of the calculation for SW(MIN) and SW(MAX) (see Table VII and section VI).

The significantly different level densities and neutron binding energies of the investigated isotopes led to correction factors F_1 of up to 2 %. In future experiments of interest for nuclear astrophysics neighboring isotopes of the same element like $^{148,\ 150}Sm$ or $^{122,\ 123,\ 124}Te$ will be investigated. In these cases, the corresponding differences are much smaller and, therefore, even smaller correction factors are expected.

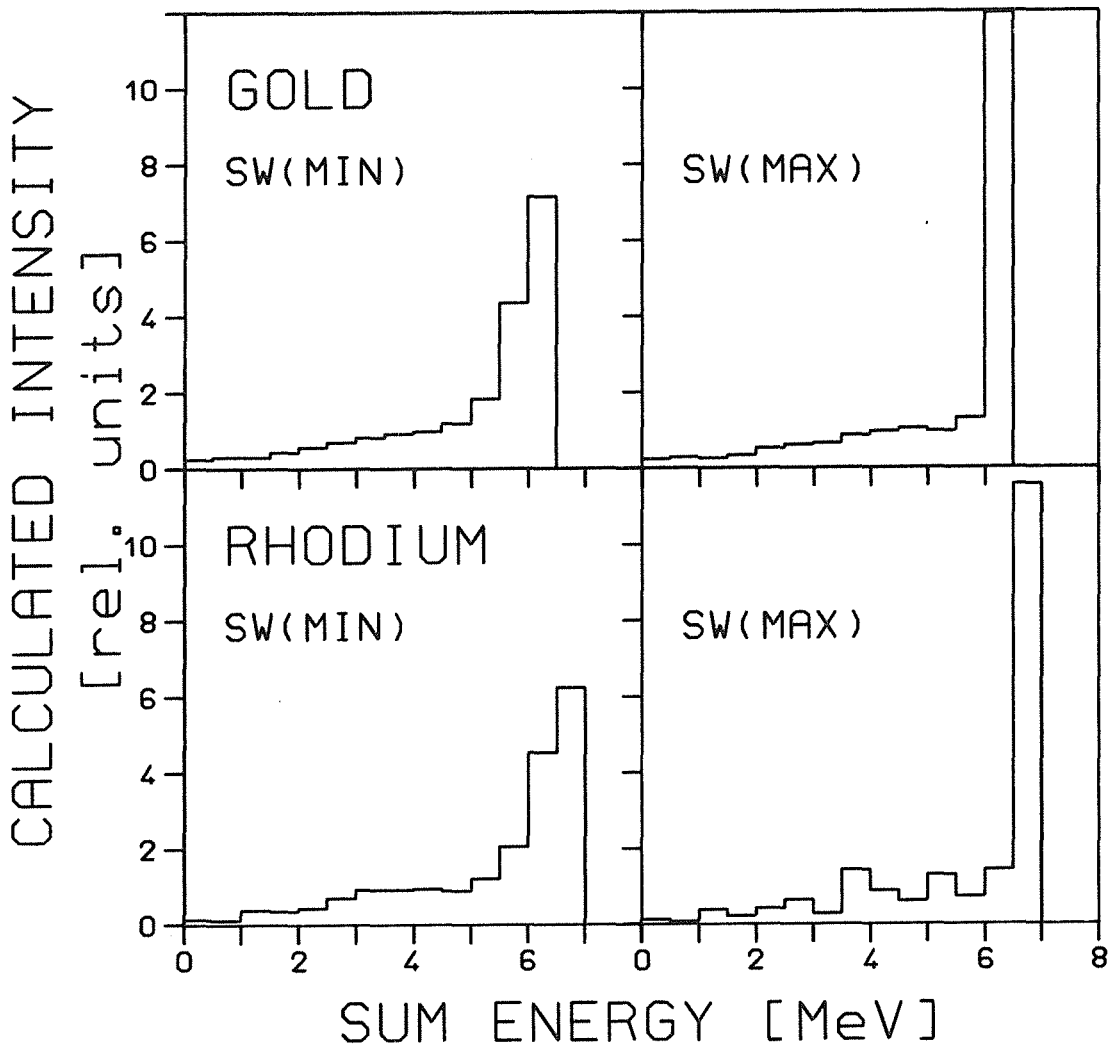

FIG. 12 Calculated sum energy spectra used for the determination of the correction F_1 for unobserved capture events.

TABLE VII. Calculated fraction of unobserved capture events, f (%), and the corresponding correction factors, F_1, for the cross section ratios.

Sample	Threshold in sum energy [MeV]					Assumption for gamma-ray efficiency
	2.0	2.32	2.5	2.67	3.0	
Solid angle 94 %, gamma-ray threshold 50 keV						
f(Au)	5.25		7.78		10.87	SW(MAX)
f(Nb)	5.56		7.87		9.96	
f(Rh)	3.77		5.89		9.12	
f(Ta)	3.68		5.67		9.45	
f(Au)	6.19		8.99		12.50	SW(MIN)
f(Nb)	6.09		8.85		11.35	
f(Rh)	4.73		6.91		10.43	
f(Ta)	4.48		7.37		12.06	
F_1(Nb/Au)	1.0011	1.0003	0.9998	0.9960	0.9885	$^1/_2$SW(MAX)+
F_1(Rh/Au)	0.9846	0.9809	0.9788	0.9788	0.9789	$^1/_2$SW(MIN)
F_1(Ta/Au)	0.9829	0.9812	0.9801	0.9834	0.9897	
Solid angle 100 %, gamma-ray threshold 0 keV						
f(Au)	2.95		4.31		6.18	SW(MAX)
f(Nb)	2.78		3.27		5.20	
f(Rh)	2.01		3.78		6.08	
f(Ta)	1.63		2.93		5.19	
f(Au)	3.52		5.20		7.31	SW(MIN)
f(Nb)	2.98		4.05		5.88	
f(Rh)	2.71		4.29		6.51	
f(Ta)	2.14		3.80		6.50	

H. Multiple scattering corrections

The correction for neutron multiple scattering and self-shielding in the sample was calculated by the SESH code[38]. In order to study the influence of the input parameters in detail and to obtain reliable estimates for the uncertainties, the calculations were carried out with three sets of input parameters (Table VIII). One set had already been used for the respective corrections in Ref. 7 and was selected to reproduce the known total and capture cross sections. The second set was adopted from Ref. 35, and the third contains the calculated parameters given in Ref.7. The resulting corrections listed in Table IX represent the mean values obtained with the different sets; however, results were only considered, if the calculated cross sections for neutron scattering or capture deviated by less than ~20 % from the compilated data of Ref. 39. For the first two sets, the level density was calculated simply by the statistical factor $1/D \sim \Sigma 2J+1$, while in the third it was treated more accurately according to:

$$\frac{1}{D} \sim f(E,J) \sim 2J+1 \frac{\exp[-\frac{(J+1/2)^2}{2\sigma^2(E)}]}{2\sigma^2(E)} \quad ,$$

where the spin cut-off factor

$$\sigma^2(E) = 0.146 \sqrt{a(B_n-\Delta)}\, A^{2/3}$$

is calculated at the neutron binding energy B_n ; a is the level density parameter. The pairing energy Δ is zero for the investigated odd-odd compound nuclei. The correction factor F_2 is defined as F_2 = MS(Au)/MS(X). Due to the very small samples used in the present experiment, all values for F_2 are below 2%. With the future improvements (section VIII) it may be possible to decrease the sample masses by an additional factor of 2 to 3 , so that this correction can be further reduced.

I. Gamma-ray self-absorption

The self-absorption of neutron capture gamma-rays in gold samples has been measured for two conventional setups using Moxon-Rae and C_6D_6 detectors in Ref. 40. Compared to these results, the present gold samples would have led to corrections of ~1 % with even smaller corrections for the cross section ratios. In these previous experiments, the gamma-ray detectors were located at 90 or 60 deg with respect to the neutron beam axis causing a

TABLE VIII. Input parameters for the calculation of neutron multiple scattering and self-shielding corrections with SESH[38]. Three parameter sets were used for each sample.

Parameter		Sample										
		Au		Nb			Rh			Ta		
Nucleon number		197		93			103			181		
Abundance		1		1			1			1		
Binding energy[MeV]		6.513		7.228			6.999			6.063		
Nucl.temp.[MeV]		0.535		0.745			0.640			0.470		
Eff.temp.[K]		293		293			293			293		
Nucl.spin		1.5		4.5			0.5			3.5		
Av.rad.width	s	0.128	0.128	0.133	0.160	0.165	0.143	0.080	0.160	0.170	0.060	0.057	0.057
[eV]	p	0.080	0.048	0.115	0.160	0.190	0.160	0.080	0.160	0.166	0.020	0.056	0.056
	d	0.080	0.048	0.115	0.160	0.165	0.143	-	0.160	0.170	0.010	0.056	0.056
Av. levelsp.	s	15.5	16.5	16.79	77.4	44.0	89.8	12.0	16.0	30.0	4.40	4.17	4.24
[eV]	p	8.45	8.25	8.62	38.7	22.0	46.6	5.3	7.1	13.8	2.2	2.08	2.17
	d	6.13	5.28	5.74	25.8	14.7	33.0	-	4.3	8.76	1.47	1.38	1.51
Strength fct.	S_0	1.8	2.0	2.1	0.36	0.60	0.47	0.54	0.53	0.32	2.1	1.7	1.8
[10^{-4}]	S_1	0.4	0.4	0.84	2.52	5.80	6.3	6.0	5.5	7.2	0.2	0.2	0.6
	S_2	0.4	0.7	0.7	0.21	1.0	1.0	-	1.0	1.0	2.3	2.3	2.3
Strength fct.	S'_0	0.2 (80keV)	0.0	0.0	0.0	0.0	0.0	0.0	0.0	0.0	0.0	0.0	0.0
inel sc. [10^{-4}]		0.8 (160keV)											
Nucl. radius	s	8.7	9.5	9.4	7.0	6.9	6.6	6.2	6.2	6.5	7.7	7.8	8.7
[fm]	p	8.0	9.5	9.4	7.0	6.9	6.6	6.2	6.2	6.5	7.7	7.8	8.7
	d	8.0	9.5	9.4	7.0	6.9	6.6	-	6.2	6.5	7.7	7.8	8.7

TABLE IX. Correction factors for neutron multiple scattering and self-shielding, MS, and the related correction factors, F_2.

Energy range	MS				F_2		
[keV]	Au	Nb	Rh	Ta	Nb/Au	Rh/Au	Ta/Au
3 - 5	1.022	1.006	1.0025	1.007	1.0159	1.0195	1.0150
5 - 10	1.021	1.010	1.0035	1.007	1.0109	1.0174	1.0139
10 - 15	1.019	1.014	1.004	1.007	1.0049	1.0149	1.0119
15 - 20	1.0185	1.0155	1.005	1.007	1.0030	1.0134	1.0114
20 - 30	1.0175	1.0195	1.005	1.007	0.9980	1.0124	1.0104
30 - 40	1.017	1.022	1.006	1.007	0.9951	1.0109	1.0099
40 - 60	1.016	1.025	1.006	1.007	0.9912	1.0099	1.0089
60 - 80	1.015	1.0275	1.007	1.007	0.9878	1.0079	1.0079
80 - 100	1.014	1.0295	1.007	1.007	0.9849	1.0070	1.0070
100 - 120	1.0135	1.031	1.007	1.007	0.9830	1.0065	1.0065
120 - 150	1.013	1.033	1.0075	1.007	0.9806	1.0055	1.0060
150 - 200	1.0125	1.035	1.008	1.007	0.9783	1.0045	1.0055
Accuracy	±0.3 %	±0.3 %	±0.2 %	±0.2 %			

considerable increase of the effective sample thickness. In addition, only one gamma-ray per capture cascade was detected. In contrast, the present setup covers the entire solid angle of 4π leading to a significantly smaller effective sample thickness, and it records all gamma-rays of a cascade. Therefore, the corrections for gamma-ray self-absorption are much smaller than 1 % and actually were neglected in the present case.

J. Neutron energy calibration

For the TOF measurement, the combined fast detector signals were used for the START of the time to pulse height converter (Ortec 467); the STOP signals were derived from the pulsed proton beam by means of a pick-up. During the experiments, the time scale was calibrated every two days (Ortec time calibrator 462). The position of the prompt gamma-ray

peak was used to define the time zero point in the TOF spectra. As discussed in Ref. 27, the output of the 42-fold OR unit for generating the START signal depends slightly on the event multiplicity, affecting the position of the prompt gamma-ray peak accordingly. In data analysis, the average position in the spectra with multiplcities 3, 4 and ≧5, which contain most of the capture events, was adopted. The differences in these three spectra are less than 50 ps, and in the spectra with multiplicity 1 and 2 they are less than 200 ps. Since the shape of the cross section is mainly determined by events with multiplicity ≧3 (section E), this small difference could be neglected.

For the definition of the time scale, the same average flight path was assumed for the prompt gamma-rays and for the neutrons. Since the intensity of the gamma-ray peak is practically equal for all samples (even in the spectrum without sample), it is probably due to prompt gamma-rays from the neutron target that are not absorbed in the lead shield. These gamma-rays are detected predominantly in the crystals closest to the neutron target and have, therefore, a slightly shorter average TOF than expected with the above assumption.

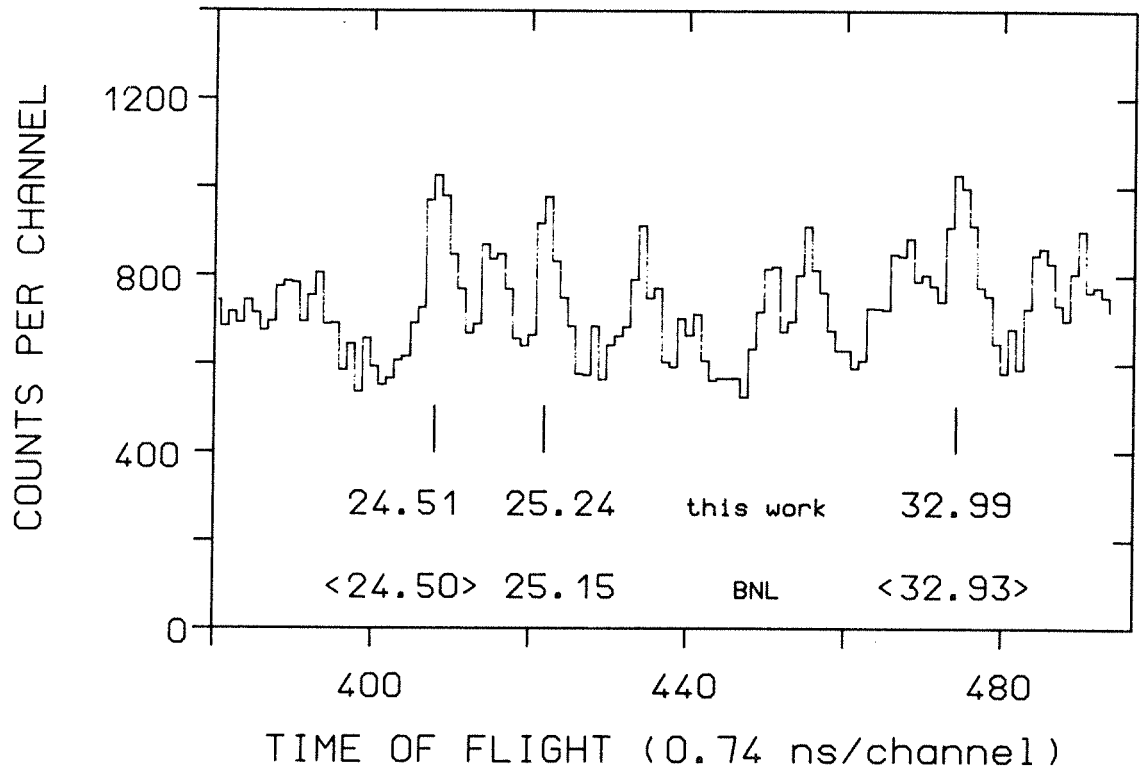

FIG.13 TOF spectrum of the ^{59}Co sample in the energy range around 20 keV, showing a few isolated resonances for a check of the energy scale.

In view of these problems, an independent experimental check of the neutron energy scale was carried out using several well known isolated resonances in ^{59}Co. Fig. 13 shows part of the TOF spectrum of the cobalt sample; in spite of the uncorrected background due to sample scattered neutrons (which in this case is large because of strong scattering amplitudes) the resonances are clearly visible. Compared to the resonance energies from literature[35], agreement within better than 100 eV is found for absolute energies around 20 keV, thus justifying the assumptions for the definition of the neutron energy scale.

V. RESULTS

The neutron capture cross section ratios of ^{93}Nb, ^{103}Rh and ^{181}Ta relative to ^{197}Au are listed with the respective uncertainties in Tables X to XIII for all three runs and the two evaluations discussed in Section IV. In evaluation 1, the original data were used, while in evaluation 2 the background was reduced by elimination of those events consisting only of signals from neighboring detector modules. Hence, evaluation 2 implies smaller statistical uncertainties and more precise normalization factors $\Sigma E(X)/\Sigma E(Au)$ in Eq.(1). In the last columns of Tables X to XIII, the weighted averages of the three runs are given with the weight being determined by the square of the statistical uncertainties.

The data of the present experiment were combined into discrete energy bins to improve the statistical accuracy of the data points and to allow easier comparison with previous measurements; the original data with full energy resolution are available on request from the authors. Since the cross section ratios depend weakly on energy, the average for the energy interval from 30 to 100 keV is also included. This interval corresponds to the TOF region with optimum signal to background ratio; therefore, these averages exhibit good statistical accuracy and are useful for the comparison between different runs and evaluations in order to check for possible systematic effects that may not be accounted for by statistical fluctuations.

An important check for the present experimental technique is the cross section ratio measured with two identical gold samples (Table X). These results are not affected by

TABLE X. The neutron capture cross section ratio of two gold samples, σ(Au II)/σ(Au I), and the respective statistical uncertainties in (%).

Energy [keV]	Run I		Run II		Run III		Average	
Evaluation 1								
5 - 10	0.9573	4.6	0.9955	6.0	-	-	0.9714	3.7
10 - 15	0.9731	2.9	0.9609	4.0	1.0800	3.8	0.9996	2.0
15 - 20	0.9928	2.2	0.9765	3.3	0.9984	2.9	0.9908	1.5
20 - 30	0.9836	1.5	1.0191	2.1	0.9836	1.7	0.9915	1.0
30 - 40	0.9997	1.4	0.9923	1.9	1.0050	1.5	0.9999	0.9
40 - 60	0.9898	1.3	1.0004	1.7	1.0010	1.4	0.9963	0.8
60 - 80	0.9981	1.3	1.0099	1.7	0.9916	1.4	0.9986	0.8
80 - 100	0.9943	1.4	1.0021	2.1	0.9980	1.4	0.9972	0.9
100 - 120	1.0040	1.8	0.9612	2.9	0.9895	1.4	0.9907	1.0
120 - 150	-	-	-	-	0.9957	1.3	0.9957	1.3
150 - 200	-	-	-	-	0.9970	1.4	0.9970	1.4
30 - 100	0.9954	0.7	1.0016	0.9	0.9987	0.7	0.9980	0.4
Evaluation 2								
3 - 5	1.0014	9.7	1.1446	13.4	-	-	1.0506	7.8
5 - 10	0.9652	3.8	1.0209	5.3	-	-	0.9841	3.1
10 - 15	0.9761	2.4	0.9937	3.4	1.0550	2.9	1.0049	1.6
15 - 20	0.9956	1.9	0.9917	2.8	0.9889	2.2	0.9925	1.3
20 - 30	0.9816	1.2	1.0193	1.8	0.9809	1.3	0.9886	0.8
30 - 40	0.9890	1.1	0.9935	1.6	1.0020	1.2	0.9946	0.7
40 - 60	0.9852	1.0	1.0088	1.3	1.0063	1.0	0.9987	0.6
60 - 80	0.9948	1.0	1.0106	1.4	0.9865	1.0	0.9947	0.6
80 - 100	0.9926	1.1	0.9977	1.6	1.0011	1.1	0.9970	0.7
100 - 120	1.0058	1.6	0.9863	2.5	0.9858	1.1	0.9915	0.9
120 - 150	-	-	-	-	1.0012	1.0	1.0012	1.0
150 - 200	-	-	-	-	1.0020	1.1	1.0020	1.1
30 - 100	0.9904	0.5	1.0038	0.7	0.9986	0.5	0.9964	0.3

systematic uncertainties correlated with the spectrum fractions and the multiple scattering corrections, because the factors F_1 and F_2 are unity by definition. Hence, this cross section ratio should also be unity with uncertainties determined only by statistics. Any additional systematic uncertainties due to neutron flux normalization or due to background subtraction should, therefore, become evident. The same holds for the systematic uncertainty related to the selection criterion of evaluation 2 as well.

There are no indications for such effects in the results given in Table X that cannot be explained by statistics and by the small systematic uncertainties due spectrum normalization and to flight path uncertainties (section VI). In particular, no systematic differences are observed for the different evaluations, which strongly supports the data of evaluation 2 to be accepted as the final results.

At this point, it is worth to emphasize the advantage of relative cross section measurements using a standard sample and changing sample and standard cyclically. In this way, the capture events in the sample as well as the neutron flux are measured with one and the same detector simultaneously, avoiding any problems caused by gain shifts, dead time losses, threshold stability, pile-up, etc. As long as the samples are changed frequently enough, all these corrections cancel out in the cross section ratio and do not cause systematic uncertainties.

The results for the capture cross section ratios of ^{93}Nb, ^{103}Rh and ^{181}Ta relative to the gold standard are compiled in Tables XI to XIII. For comparison of the results from individual runs and evaluations, the averaged values in the 30 to 100 keV interval are again best suited. A systematic trend might be visible in the data of evaluation 1, where the results of run III are below and those of run I above the average. The largest deviation is found for tantalum with run III being 2.3% below and run I 1.6% above the average. But even in this case, run III differs from the average only by two standard deviations. Such an effect can still be attributed to statistics; this appears the more plausible as these trends are absent in the results of the statistically more accurate evaluation 2. The average results in the 30 to 100 keV interval obtained in evaluations 1 and 2 are consistent within 0.8% for all three isotopes. This fact confirms that the compilation of uncertainties in section VI is reliable as well as that the data obtained in evaluation 2 can be considered as the final results.

These final cross section ratios are compiled in Table XIV together with the overall statistical

TABLE XI. The neutron capture cross section ratios $\sigma(^{93}Nb)/\sigma(^{197}Au)$ and the respective statistical uncertainties in (%).

Energy [keV]	Run I		Run II		Run III		Average	
Evaluation 1								
5 - 10	0.4947	6.2	0.4708	8.9	-	-	0.4869	5.1
10 - 15	0.5370	3.7	0.5174	5.4	0.5796	4.8	0.5448	2.6
15 - 20	0.5343	2.9	0.5626	4.2	0.5684	3.8	0.5505	2.0
20 - 30	0.5224	2.0	0.5296	2.9	0.5336	2.7	0.5271	1.4
30 - 40	0.5038	1.8	0.5003	2.6	0.4909	2.5	0.4996	1.3
40 - 60	0.4482	1.7	0.4514	2.4	0.4429	2.4	0.4477	1.2
60 - 80	0.3911	1.7	0.3980	2.4	0.3791	2.5	0.3900	1.2
80 - 100	0.3806	1.8	0.3785	2.6	0.3707	2.5	0.3775	1.3
100 - 120	0.3408	2.5	0.3407	3.9	0.3450	2.5	0.3425	1.6
120 - 150	-	-	-	-	0.3263	2.4	0.3263	2.4
150 - 200	-	-	-	-	0.3035	2.4	0.3035	2.4
30 - 100	0.4303	0.9	0.4315	1.2	0.4213	1.2	0.4281	0.6
Evaluation 2								
3 - 5	0.3292	16.9	0.4088	19.8	-	-	0.3628	12.8
5 - 10	0.5095	4.8	0.4594	7.3	-	-	0.4944	4.0
10 - 15	0.5382	2.9	0.5321	4.1	0.5791	4.7	0.5449	2.1
15 - 20	0.5382	2.2	0.5489	3.3	0.5770	2.8	0.5521	1.5
20 - 30	0.5211	1.5	0.5210	2.1	0.5335	1.9	0.5247	1.0
30 - 40	0.5016	1.4	0.4958	2.0	0.4990	1.7	0.4995	1.0
40 - 60	0.4502	1.3	0.4444	1.7	0.4457	1.6	0.4474	0.9
60 - 80	0.3917	1.3	0.3892	1.8	0.3865	1.7	0.3896	0.9
80 - 100	0.3794	1.4	0.3664	2.0	0.3720	1.7	0.3742	1.0
100 - 120	0.3345	2.0	0.3401	3.2	0.3397	1.8	0.3378	1.2
120 - 150	-	-	-	-	0.3230	1.7	0.3230	1.7
150 - 200	-	-	-	-	0.2984	1.7	0.2984	1.7
30 - 100	0.4300	0.7	0.4239	0.9	0.4264	0.8	0.4270	0.5

TABLE XII. The neutron capture cross section ratios $\sigma(^{103}Rh)/\sigma(^{197}Au)$ and the respective statistical uncertainties in (%).

Energy [keV]	Run I		Run II		Run III		Average	
Evaluation 1								
5 - 10	1.0481	7.0	1.0649	9.5	-	-	1.0540	5.6
10 - 15	1.3302	3.6	1.3257	5.1	1.3085	5.0	1.3235	2.5
15 - 20	1.4444	2.6	1.4334	3.9	1.4225	3.5	1.4359	1.8
20 - 30	1.6253	1.7	1.5921	2.4	1.6098	2.0	1.6128	1.1
30 - 40	1.5544	1.5	1.5422	2.1	1.5012	1.8	1.5348	1.0
40 - 60	1.5820	1.4	1.5927	1.9	1.5603	1.6	1.5773	0.9
60 - 80	1.5230	1.4	1.5758	1.9	1.4957	1.6	1.5264	0.9
80 - 100	1.5002	> 1.5	1.4572	2.1	1.4455	1.6	1.4709	1.0
100 - 120	1.4356	2.0	1.3613	3.1	1.3780	1.6	1.3950	1.2
120 - 150	-	-	-	-	1.3094	1.5	1.3094	1.5
150 - 200	-	-	-	-	1.1931	1.6	1.1931	1.6
30 - 100	1.5408	0.7	1.5462	1.0	1.5006	0.8	1.5291	0.5
Evaluation 2								
3 - 5	0.9481	14.7	1.0359	20.4	-	-	0.9781	11.9
5 - 10	1.1067	5.3	1.0198	8.1	-	-	1.0806	4.4
10 - 15	1.3066	2.8	1.2890	4.2	1.3998	3.5	1.3315	1.9
15 - 20	1.4504	2.1	1.4434	3.1	1.4824	2.5	1.4593	1.4
20 - 30	1.6025	1.3	1.5856	1.9	1.6031	1.4	1.5993	0.9
30 - 40	1.5420	1.2	1.5362	1.7	1.5040	1.3	1.5270	0.8
40 - 60	1.5651	1.0	1.5646	1.4	1.5554	1.1	1.5616	0.7
60 - 80	1.5130	1.0	1.5561	1.5	1.4979	1.1	1.5159	0.7
80 - 100	1.4723	1.1	1.4401	1.7	1.4441	1.1	1.4551	0.7
100 - 120	1.3882	1.6	1.3966	2.6	1.3544	1.2	1.3702	0.9
120 - 150	-	-	-	-	1.3007	1.1	1.3007	1.1
150 - 200	-	-	-	-	1.1697	1.1	1.1697	1.1
30 - 100	1.5240	0.5	1.5302	0.8	1.5001	0.6	1.5157	0.3

TABLE XIII. The neutron capture cross section ratios $\sigma(^{181}Ta)/\sigma(^{197}Au)$ and the respective statistical uncertainties in (%).

Energy [keV]	Run I		Run II		Run III		Average	
Evaluation 1								
5 - 10	1.4086	5.8	1.4050	7.7	-	-	1.4073	4.6
10 - 15	1.3378	3.6	1.3343	4.9	1.3063	4.7	1.3282	2.5
15 - 20	1.3853	2.7	1.5031	3.7	1.3753	3.4	1.4114	1.8
20 - 30	1.4538	1.8	1.4540	2.5	1.3997	2.1	1.4362	1.2
30 - 40	1.3535	1.7	1.3429	2.3	1.2989	1.9	1.3324	1.1
40 - 60	1.3325	1.5	1.3234	2.1	1.2750	1.7	1.3109	1.0
60 - 80	1.2678	1.6	1.2657	2.1	1.2209	1.7	1.2505	1.0
80 - 100	1.2895	1.6	1.2637	2.3	1.2539	1.7	1.2709	1.0
100 - 120	1.2100	2.2	1.2765	3.3	1.2079	1.7	1.2183	1.2
120 - 150	-	-	-	-	1.1551	1.7	1.1551	1.7
150 - 200	-	-	-	-	1.0436	1.8	1.0436	1.8
30 - 100	1.3104	0.8	1.2985	1.1	1.2602	0.9	1.2900	0.5
Evaluation 2								
3 - 5	1.2322	12.9	1.5653	15.2	-	-	1.3717	9.8
5 - 10	1.3821	4.7	1.4420	6.2	-	-	1.4040	3.7
10 - 15	1.3181	2.8	1.3565	3.9	1.3751	3.4	1.3447	1.9
15 - 20	1.3544	2.1	1.4954	2.9	1.4287	2.5	1.4111	1.4
20 - 30	1.4265	1.4	1.4280	1.9	1.3927	1.5	1.4146	0.9
30 - 40	1.3268	1.3	1.3164	1.8	1.3148	1.4	1.3202	0.8
40 - 60	1.3017	1.1	1.2992	1.5	1.2854	1.2	1.2954	0.7
60 - 80	1.2396	1.2	1.2518	1.6	1.2355	1.2	1.2407	0.7
80 - 100	1.2514	1.2	1.2362	1.8	1.2507	1.2	1.2484	0.8
100 - 120	1.1821	1.8	1.2493	2.8	1.2115	1.3	1.2074	1.0
120 - 150	-	-	-	-	1.1633	1.2	1.1633	1.2
150 - 200	-	-	-	-	1.0328	1.3	1.0328	1.3
30 - 100	1.2792	0.6	1.2767	0.8	1.2685	0.6	1.2748	0.4

TABLE XIV. The final neutron capture cross section ratios of ^{93}Nb, ^{103}Rh, and ^{181}Ta relative to ^{197}Au together with the statistical and systematic uncertainties in (%). The ratios are converted to absolute cross sections using the gold data from literature[41,42].

Energy [keV]	$\frac{(^{93}Nb)}{\sigma(^{197}Au)}$	uncertainty stat	sys	tot	$\frac{\sigma(^{103}Rh)}{\sigma(^{197}Au)}$	uncertainty stat	sys	tot	$\frac{\sigma(^{181}Ta)}{\sigma(^{197}Au)}$	uncertainty stat	sys	tot
3 - 5	0.3628	12.8	0.8	12.8	0.9781	11.9	0.7	11.9	1.3717	9.8	0.7	9.8
5 - 10	0.4944	4.0	0.8	4.1	1.0806	4.4	0.7	4.6	1.4040	3.7	0.7	3.8
10 - 15	0.5449	2.1	0.8	2.2	1.3315	1.9	0.7	2.0	1.3447	1.9	0.7	2.0
15 - 20	0.5521	1.5	0.8	1.7	1.4593	1.4	0.7	1.6	1.4111	1.4	0.7	1.6
20 - 30	0.5247	1.0	0.8	1.3	1.5993	0.9	0.7	1.1	1.4146	0.9	0.7	1.1
30 - 40	0.4995	1.0	0.8	1.3	1.5270	0.8	0.7	1.1	1.3202	0.8	0.7	1.1
40 - 60	0.4474	0.9	0.8	1.2	1.5616	0.7	0.7	1.0	1.2954	0.7	0.7	1.0
60 - 80	0.3896	0.9	0.8	1.2	1.5159	0.7	0.7	1.0	1.2407	0.7	0.7	1.0
80 - 100	0.3742	1.0	0.8	1.3	1.4551	0.7	0.7	1.0	1.2484	0.8	0.7	1.1
100 - 120	0.3378	1.2	0.8	1.4	1.3702	0.9	0.7	1.1	1.2074	1.0	0.7	1.2
120 - 150	0.3230	1.7	0.8	1.9	1.3007	1.1	0.7	1.3	1.1633	1.2	0.7	1.4
150 - 200	0.2984	1.7	0.8	1.9	1.1697	1.1	0.7	1.3	1.0328	1.3	0.7	1.5

Energy [keV]	$\sigma(^{197}Au)$ [mbarn]	$\sigma(^{93}Nb)$ [mbarn]	$\sigma(^{103}Rh)$ [mbarn]	$\sigma(^{181}Ta)$ [mbarn]
3 - 5	2266.8	822.4	2217.2	3109.4
5 - 10	1471.2	727.4	1589.8	2065.6
10 - 15	972.4	529.8	1294.7	1307.5
15 - 20	738.8	407.9	1078.1	1042.5
20 - 30	585.4	307.2	936.3	828.2
30 - 40	500.4	250.0	764.1	660.6
40 - 60	411.5	184.1	642.6	533.0
60 - 80	349.4	136.1	529.6	433.5
80 - 100	298.3	111.6	434.1	372.4
100 - 120	290.1	98.0	397.5	350.3
120 - 150	274.1	88.5	356.6	318.9
150 - 200	258.1	77.0	301.9	266.6

and systematic uncertainties. The experimental ratios were also converted into absolute cross sections by means of the gold cross section of Macklin[41] after normalization by a factor of 0.989 to the absolute value of Ratinsky and Käppeler[42]. These authors determined the Maxwellian average at kT=30 keV to 582±9 mb, which is the most accurate capture cross section in the keV range, two times more accurate than the respective value calculated from the data of Macklin[41]. Hence, the uncertainties of the absolute values in Table XIV include the 1.5% uncertainty of the gold cross section and a small uncertainty correlated with the shape of the standard cross section of Ref. 41.

Compared with our previous measurement[7], an average deviation of only ~2% is obtained in the range from 20 to 60 keV, where the optimum accuracy was achieved (Figs.14 , 15 , 16). In view of the 5 times better accuracy of the present data, this agreement means simply that the corrections in the old measurement were properly treated. The comparison with other measurements remains unchanged as in Ref. 7, because only one new measurement was reported for these isotopes since. This new ^{181}Ta cross section of Macklin[20] is ~10% lower on average than our present results.

VI. DISCUSSION OF UNCERTAINTIES

A. Statistics

The cross section ratios in Tables X to XIII are energy averaged values calculated via Eq.(1). In total, six terms of Eq. (1) contribute to the statistical uncertainty, i.e. Z_i, ΣZ, and ΣE of sample X and of the gold sample. These terms have the same structure

$$Z(X) = N(X) - f\cdot N(C) - (1-f)\cdot N(L) - B(X) + f\cdot B(C) + (1-f)\cdot B(L)$$

where N stands for the net counts measured with sample X, with the graphite sample C, and with the empty position, L. Correspondingly, B denotes the time-independent backgrounds and f is the normalization factor of the graphite spectrum for proper correction of background from sample scattered neutrons.

Obviously, several quantities occur in more than one term of Eq. (1), i.e. $\Sigma E(X)$ completely includes $\Sigma Z(X)$, and the time-independent backgrounds form part of the entries Z and ΣZ. The statistical uncertainties of the six terms are, therefore, correlated; this means that the squared statistical uncertainties of the cross section ratios are not simply given by summation

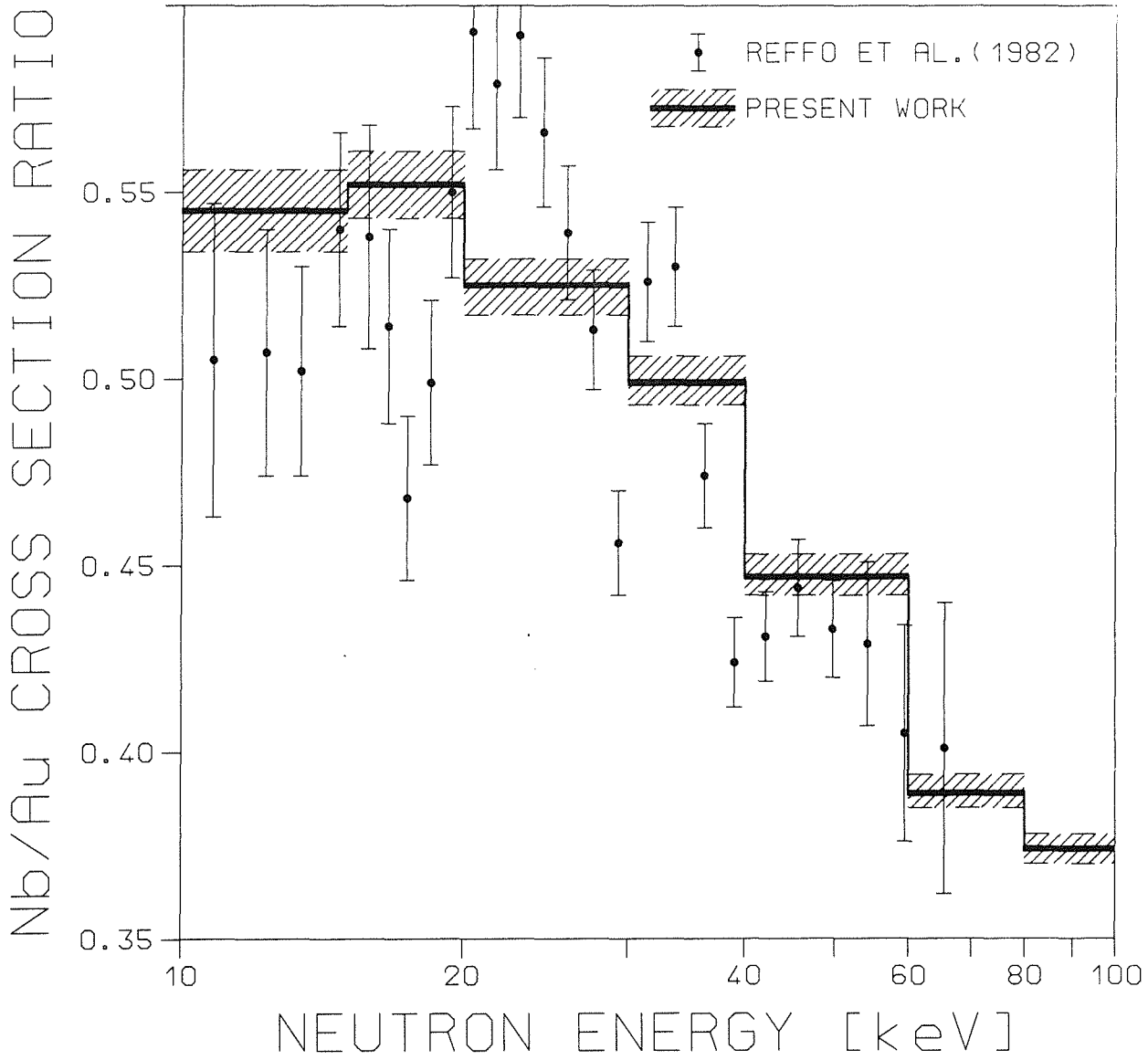

FIG.14 The neutron capture cross section ratio $\sigma(^{93}Nb)/\sigma(^{197}Au)$ compared to the results of Ref. 7.

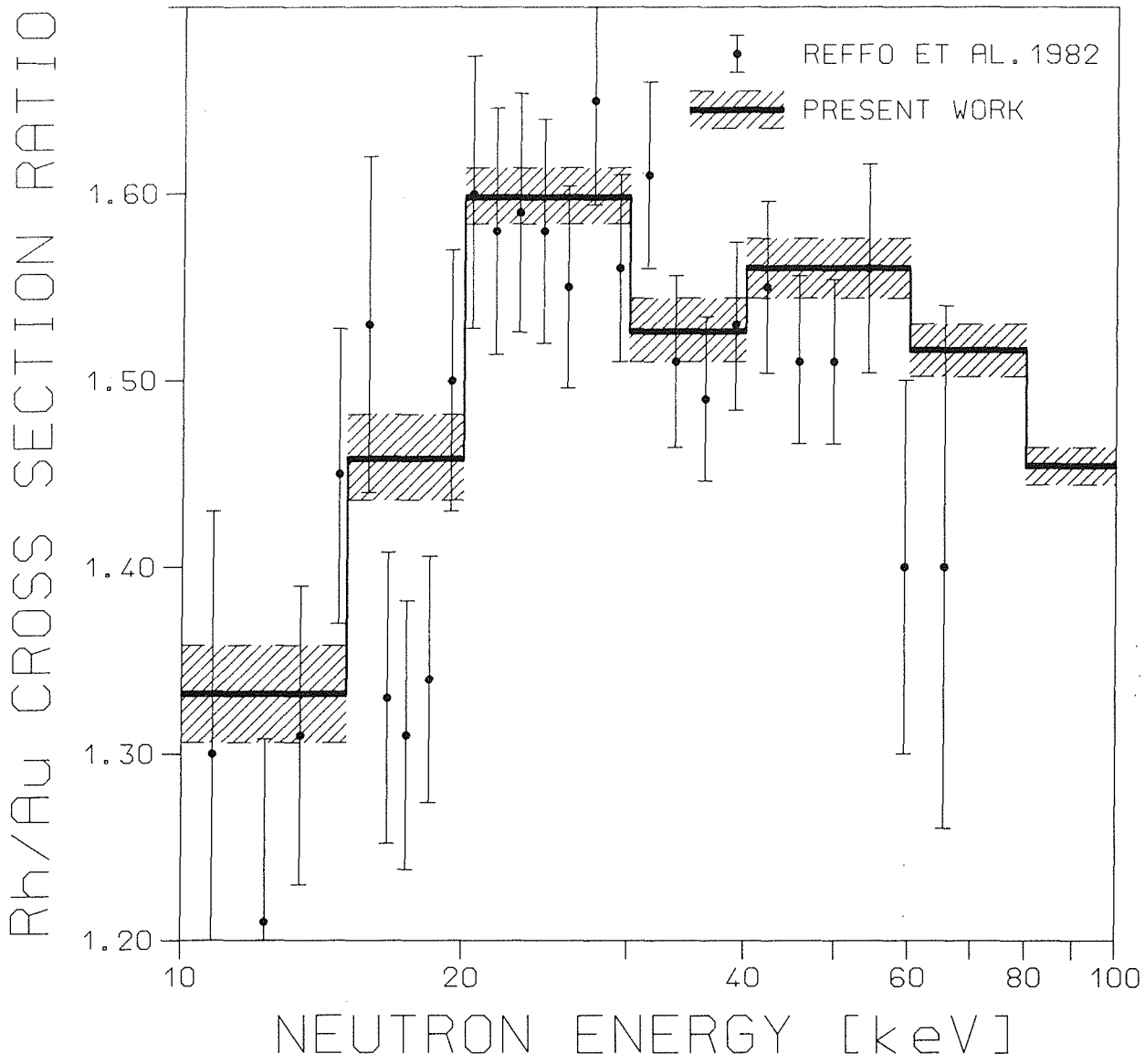

FIG.15 The neutron capture cross section ratio $\sigma(^{103}Rh)/\sigma(^{197}Au)$ compared to the results of Ref. 7.

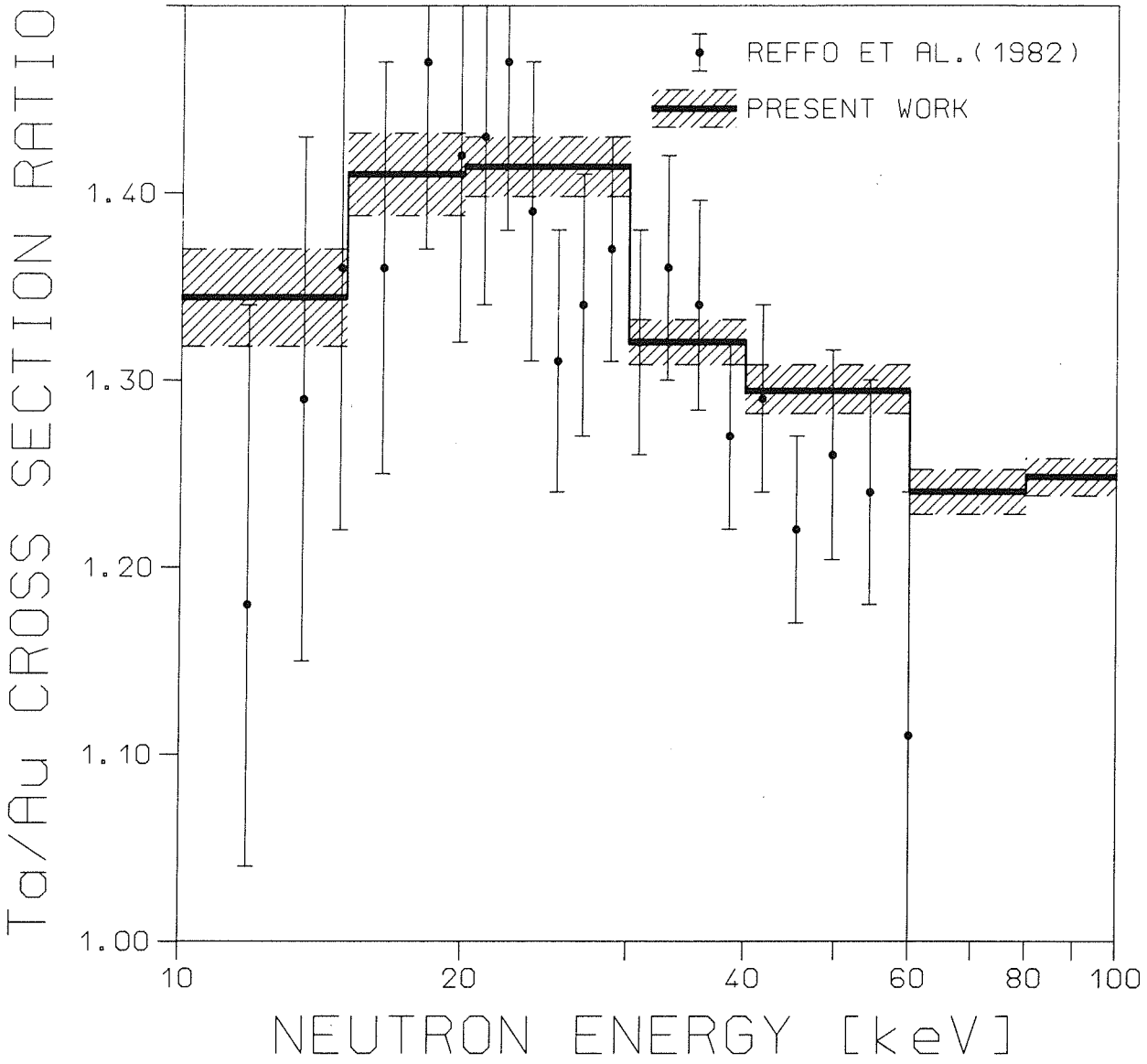

FIG.16 The neutron capture cross section ratio $\sigma(^{181}Ta)/\sigma(^{197}Au)$ compared to the results of Ref. 7.

of the squared statistical uncertainties of the individual terms. For the calculation of appropriate correction terms, the entries N and B have to be subdivided into components with and without overlapping pulse height and (if necessary) TOF channels.

In order to keep the number of terms manageable, several simplifying assumptions were introduced in calculating the correlations: no weight was given to the channel widths in averaging over energy bins, and the weak dependence of the normalization factors, f, on neutron energy was neglected. Then, 16 statistically different terms had still to be treated, giving rise to 56 and 90 correlated uncertainty terms (depending on whether or not the energy bin and the normalization interval do overlap). Since these terms can either be positive or negative, the consideration of these correlations results in a reduction of the overall statistical uncertainty.

B. Systematic uncertainties

The various components of the systematic uncertainties discussed below are compiled in Table XV.

(i) *Background subtraction.* The subtraction of time-independent and time-dependent backgrounds may cause a systematic uncertainty, particularly at low neutron energies where the signal to background ratio is smaller. In case of the time-independent background, nonlinearities in the TOF scale may cause a similar problem, since this background is determined in a TOF range different from that of the capture events. However, such effects cancel out to a large extent in relative measurements; indeed, no evidence beyond the statistical uncertainties was observed in the cross section ratio of the two gold samples (Table X). Since the count rates from sample and reference sample differed on average only by ~20%, no corrections are required in the cross section ratios, and the related systematic uncertainties were neglected.

(ii) *Flight path.* The flight path of the individual samples was measured with an accuracy of 0.1 mm and it was found to be equal for all samples within an accuracy of ±0.2 mm. The average flight path being 775 mm causes a difference in solid angle of 0.1%, if sample and reference sample are supposed to be located at the two extreme positions. Therefore, a systematic uncertainty of 0.1% was included in our analysis.

TABLE XV. Systematic uncertainties [%].

Flight path (cross section ratio):		0.1
Neutron flux normalization (sample):		0.1
Neutron flux normalisation (standard):		0.1
Sample mass (Nb, Rh, Ta):		0.1
Multiple scattering (Au):		0.3
	(Nb):	0.3
	(Rh):	0.2
	(Ta):	0.2
Unobserved events (cross section ratio):		0.6
total	σ(Au)/σ(Au):	0.2
systematic	σ(Nb)/σ(Au):	0.8
uncertainties:	σ(Rh)/σ(Au):	0.7
	σ(Ta)/σ(Au):	0.7

(iii) *Sample mass.* The masses of the individual samples have been determined before and after the experiment to better than 100 μg; therefore, this uncertainty is negligible. The purity of the sample material was >99.9% for the three investigated isotopes and >99.99% for the gold samples. Since it is unlikely that the impurities should have significantly larger capture cross sections, a correlated systematic uncertainty of 0.1% was assumed, which accounts for the case that the impurities have very small cross sections. The uncertainty for the gold samples could be neglected.

(iv) *Dead time and stability.* The event rate for captures in the gold sample varied between 4 and 10 Hz in the different runs, and was ~20% smaller for the other isotopes. The total background rate correlated with the sample mass is a factor of two larger than the capture rate. The overwhelming part of the recorded count rate of 500 to 1000 Hz is independent of the sample, and, therefore, systematic uncertainties due to dead time effects can be excluded.

The gain of all detector modules was stabilized throughout the experiment using the

α-lines of the radium impurities in the BaF_2 crystals for internal calibration. In addition, the thresholds of the constant fraction discriminators were continuously checked without observing any significant shift during the measuring period of two weeks. As pointed out before, relative measurements are insensitive to long term drifts as long as the samples are changed in comparably short intervals (~10 min in the present experiment). Hence, systematic uncertainties due to stability problems could be excluded.

(v) *Pile-up.* The overall count rate of all 40 detector modules above a threshold energy of 50 keV is approximately 40 kHz. The fast decision whether the gates of the individual modules are opened to accept an event for further processing is made in an interval of ~10 ns. This is 2000 times shorter than the mean signal distance,and hence, the probability for catching a signal accidentally together with those of a true capture event is small. After this fast decision, the gates of typically 4 detector modules are open for 3 μs. The integral count rate of these modules is ~4 kHz only, so that the probability for pile-up is still small. Indeed, only ~0.5% of the capture events are registered at energies above the neutron binding energy (see Fig 9). Moreover, this effect cancels out in the ratio, since the number of pile-up events is proportional to the observed capture rate in first approximation. Again, systematic uncertainties due to pile-up could be neglected.

(vi) *Normalization to equal neutron flux.* The integrated count rates of the two neutron monitor detectors are given in Table XVI and are normalized to unity for easier comparison. From the spread of the results obtained with good statistics in runs I and III, a correlated uncertainty of ~0.1% was deduced for this correction. In view of the larger systematic uncertainties for multiple scattering and for unobserved events, these small uncertainties were rounded to one digit. As can be seen from Table XVI, the corresponding corrections were less than 0.5% for all samples.

(vii) *Spectrum fraction.* The largest systematic uncertainty in the present experiment had to be assigned to the correction for undetected capture events falling below the threshold in the sum energy spectra. Therefore, this correction was studied in detail to reveal the influence of the relevant parameters. In the following, the related uncertainties are given in brackets for each of the investigated effects:

- In the calculation of the detection probabilities, the number of bins for the gamma-ray energy was changed from 10 (Ref. 8) to 20 as given in Table VI [0.4%].
- The solid angle covered by detector material was varied between 93 and 95% to check

TABLE XVI. Relative count rates of the two neutron monitor detectors (monitor 1: 20 cm from neutron target; monitor 2: at 2.5 m flight path).

Sample	Run I			Run II			Run III		
	mon1	mon 2	mean	mon 1	mon2	mean	mon1	mon2	mean
1	1.0028	1.0049	1.0039	1.0045	1.0003	1.0024	1.0036	1.0012	1.0024
2	1.0032	1.0019	1.0026	1.0039	1.0027	1.0033	1.0007	0.9994	1.0001
3	1.0002	0.9976	0.9989	1.0028	1.0012	1.0020	1.0013	1.0011	1.0012
4	0.9980	1.0013	0.9997	1.0032	0.9995	1.0014	1.0004	0.9996	1.0000
5	1.0001	0.9969	0.9985	1.0043	0.9979	1.0011	0.9984	0.9970	0.9977
6	1.0013	-	-	0.9990	-	-	0.9983	-	-
7	0.9964	0.9994	0.9979	0.9925	1.0004	0.9965	0.9984	0.9996	0.9990
8	0.9978	0.9980	0.9979	0.9898	0.9980	0.9939	0.9988	1.0020	1.0004
stat. uncert.	0.11%	0.12%		0.18%	0.18%		0.04%	0.09%	

for losses through gaps between the detector modules [0.4%].

- The gamma-ray threshold was changed in the calculations between 0 to 100 keV [0.15%].
- Since limitations in computing time did not allow to consider all cascades with multiplicity 6 in the calculation of the sum energy spectra of gold and tantalum, it was shown at a few examples that the resulting uncertainty was small [0.15%].
- All calculations were made for both assumptions on the detection probability SW(MAX) and SW(MIN) [0.15%].

These contributions add to a total uncertainty of 0.6% . It has to be mentioned again that the absolute detection efficiency is not required in relative measurements. This absolute efficiency would be more difficult to determine, since it strongly depends on the threshold (see Table VII); however, this threshold acts on the fast sum energy signal and is less well defined due to the limited energy resolution of that signal.

(viii) *Multiple scattering.* The correction for neutron multiple scattering and self-shielding was calculated with the SESH code[38] after modification by the author to allow for up to 10^5

Monte Carlo histories. All calculations were made with the three input parameter sets given in Table VIII. The spread of the respective results yields the estimated uncertainties given in Table XV. The smaller uncertainties for ^{181}Ta and ^{103}Rh correspond to the smaller correction factors of less than 1% in these cases.

(ix) *Gamma-ray self-absorption.* As discussed in section V, these corrections and the related systematic uncertainties can be neglected.

VII. MAXWELLIAN AVERAGED CROSS SECTIONS

The Maxwellian averaged cross section in a stellar plasma of thermal energy kT is defined as[43]:

$$\langle\sigma\rangle = \frac{\langle\sigma v\rangle}{v_T} = \frac{2}{\sqrt{\pi}} \frac{\int_0^\infty \sigma_{n\gamma} E \exp(-E/kT)\, dE}{\int_0^\infty E \exp(-E/kT)\, dE} = \frac{2}{\sqrt{\pi}} \frac{1}{(kT)^2} \int_0^\infty \sigma_{n\gamma} E \exp(-E/kT)\, dE \quad (3)$$

Since cross sections have only been measured over a limited energy range in the present work, it is convenient to subdivide the integral into four separate parts according to the different data from which they are calculated as schematically indicated in Fig. 17.

$$\langle\sigma\rangle = \frac{2}{\sqrt{\pi}} \frac{1}{(kT)^2} \left\{ \int_0^{E_1} \ldots dE + \int_{E_1}^{E_2} \ldots dE + \int_{E_2}^{E_3} \ldots dE + \int_{E_3}^{\infty} \ldots dE \right\} = I_1 + I_2 + I_3 + I_4 \quad (4)$$

The main contribution I_3 results from the measured cross sections in the energy range from E_2 to E_3. The term I_2 accounts for the gap between the last known resonance at E_1 and E_2, and I_4 is the contribution from energies beyond the measured range.

The integral I_3 is approximated by the sum

$$I_3 = \frac{2}{\sqrt{\pi}} \frac{1}{(kT)^2} \sum \sigma_{n\gamma,i} E_i \exp(-E_i/kT)\, \Delta E_i \quad (5)$$

where $\sigma_{n\gamma,i}$ is the measured capture cross section in bin i with a width ΔE_i centered at energy E_i.

The integral I_1 over the resonance energy range is approximated according to Ref. 43 by

$$I_1 = \frac{2}{\sqrt{\pi}} \sum A_r \frac{E_r}{(kT^2)} \exp(-E_r/kT), \quad \text{with} \quad A_r = (2\pi^2/k^2)\,(g\Gamma_n\Gamma_\gamma/\Gamma).$$

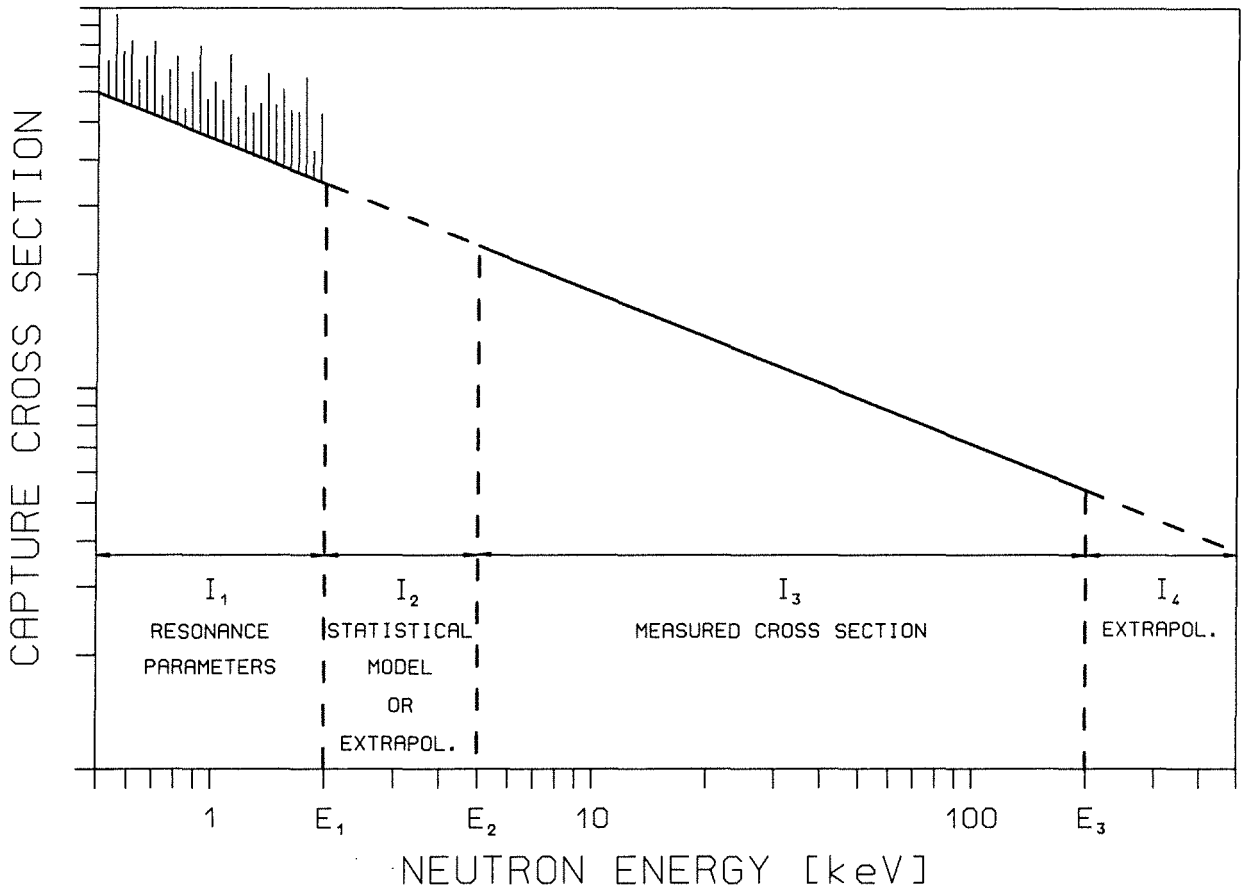

FIG. 17 Subdivision of the neutron energy range for the determination of Maxwellian averaged cross sections.

The sum runs over all resonances with energy E_r; the resonance areas A_r are determined by the neutron, radiation, and total widths Γ_n, Γ_γ, and Γ, respectively. The statistical factor $g=(2J+1)/2(2I+1)$ depends on compound state spin J and target spin I, and *k* is the wave number at the resonance energy.

The resonance parameters were taken from Ref. 35. For all three nuclei, parameters of some individual resonances are missing, e.g. J or Γ_γ. In the case of missing Γ_γ the average radiation width was adopted in the calculations. The contribution of resonances without spin assignment was calculated assuming all $J=I+1/2$ *and* $J=I-1/2$ and adopting the average. In principle, also contributions from direct capture or from negative resonances have to be considered, but they are negligible for the three nuclei investigated and will not be discussed.

For the gap between E_1 and E_2 two different approaches were considered:

(i) Statistical model calculations[44] using formulas given in Ref. 35.

(ii) Theoretical cross sections from Ref. 7.

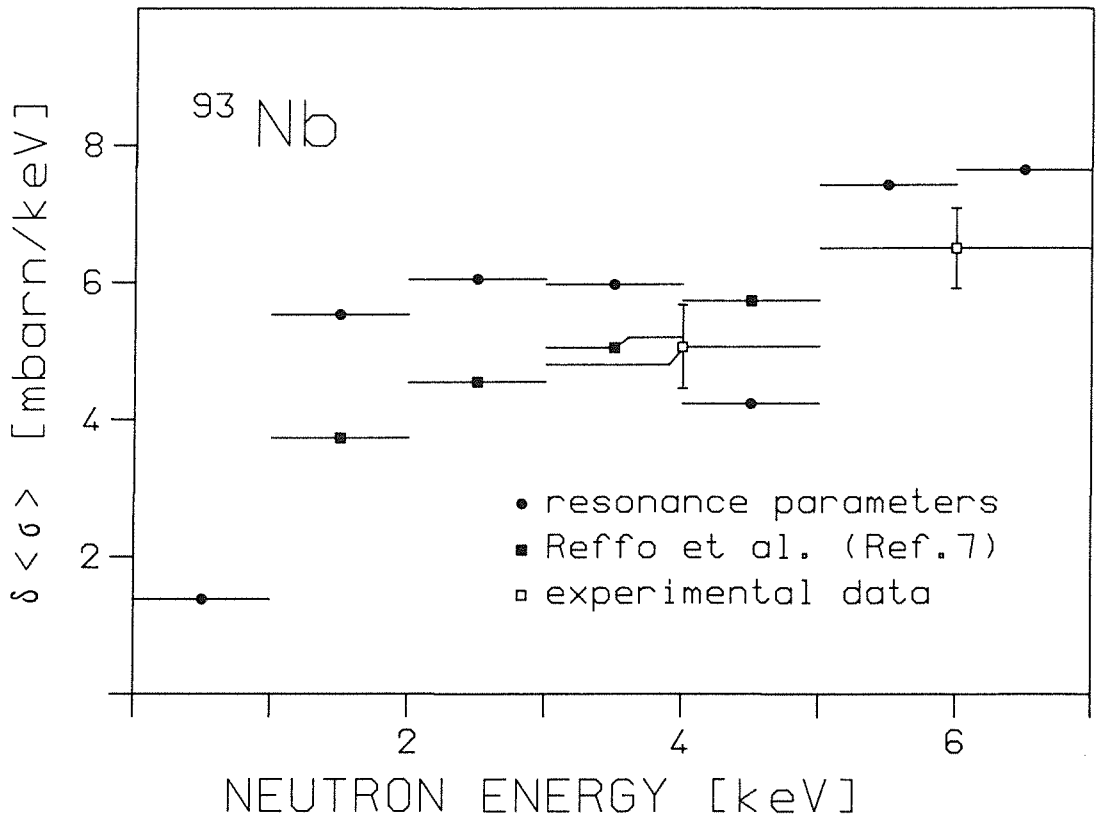

FIG. 18 Contribution from low neutron energies to the Maxwellian averaged cross section of ^{93}Nb at kT=25 keV as determined by different methods (see text).

In order to get an estimate of the uncertainties associated with different methods their contributions to the total integral were compared in 1 keV wide energy bins. For this purpose, the calculations according to (ii) were not restricted to the true gap but also extended into the region of resonance parameters. On the other hand, the contributions from resonances were also calculated for energies overlapping with the measured energy range.

^{93}Nb: Resonance parameters are available up to 7.3 keV. Therefore, there is no gap and no statistical model calculations are required. In addition, the contributions derived from experiment and resonances can be compared. The results are presented in Fig. 18.

^{103}Rh: Resonance parameters are available up to 4.2 keV. Accordingly, the statistical model is only required for the bin 4-5 keV. The results are presented in Fig. 19.

^{181}Ta: Resonance parameters are available up to 2 keV giving rise to a relatively large gap. The results are presented in Fig. 20.

The following conclusions can be drawn from the figures: The data points derived from measured cross sections are consistent with those based on resonance parameters and/or

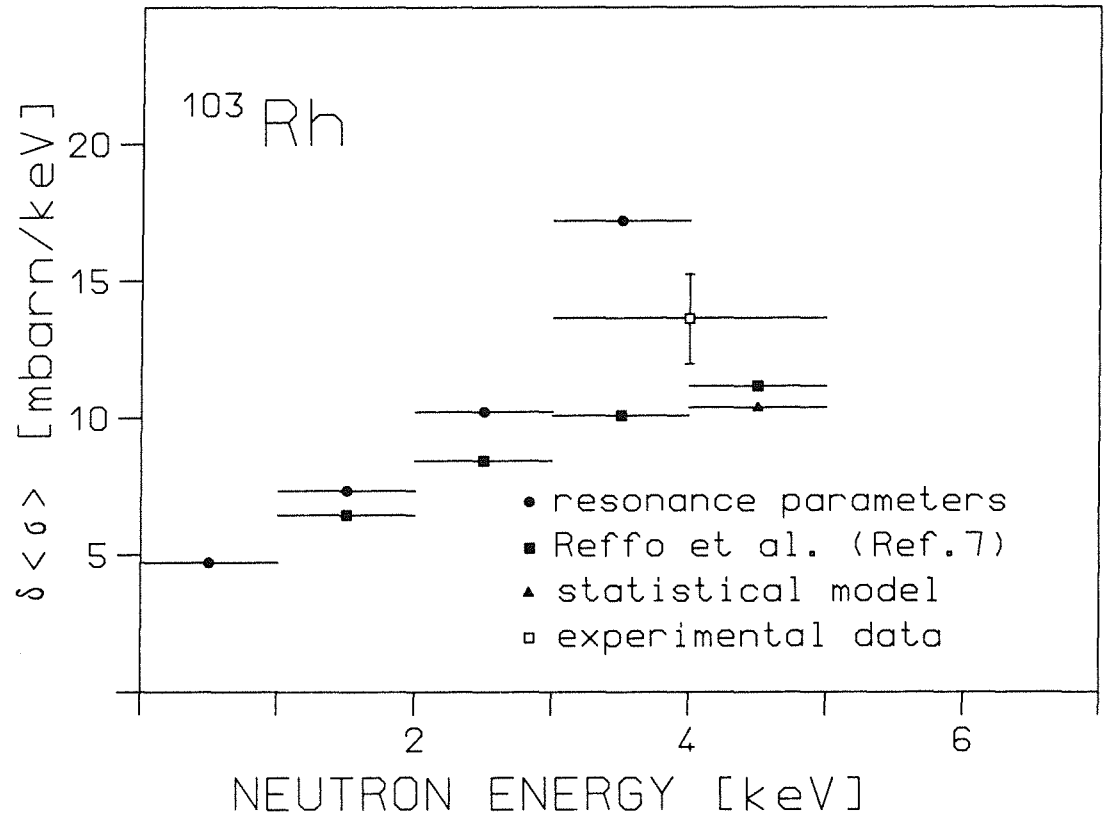

FIG. 19 Same as Fig. 18 but for ^{103}Rh

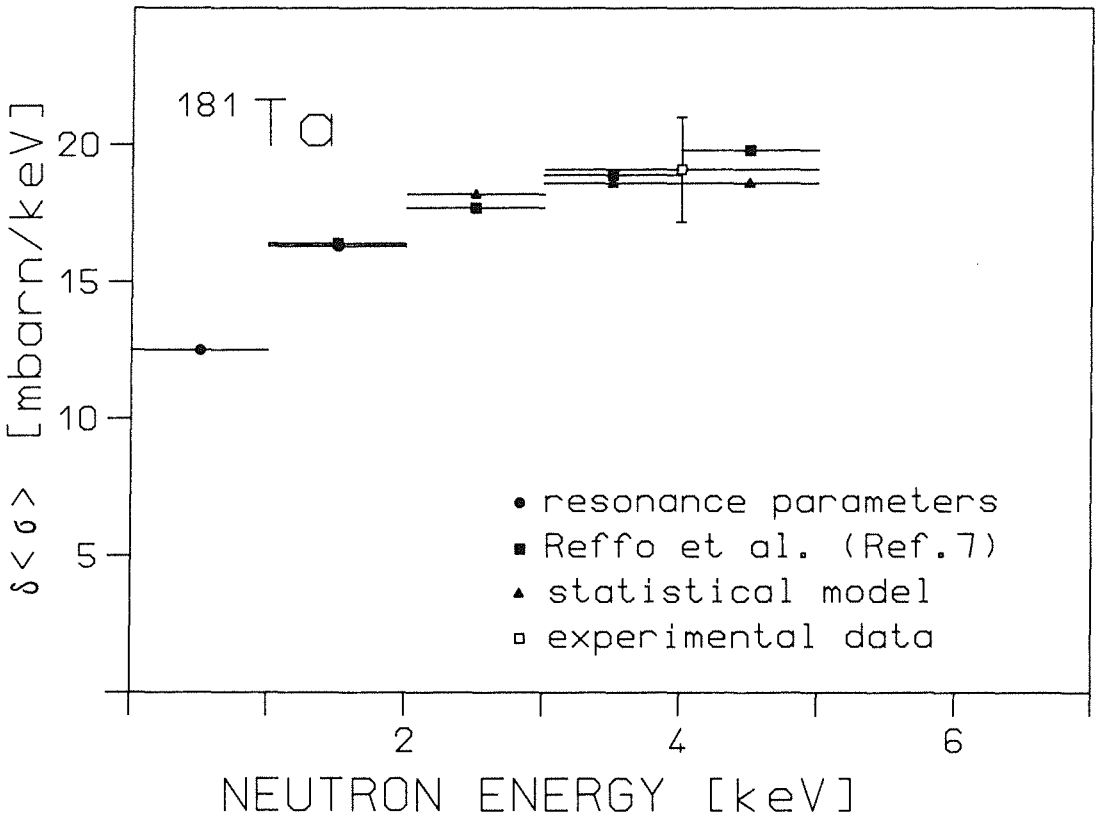

FIG. 20 Same as Fig. 18 but for ^{181}Ta.

the statistical model. While in individual bins the data of Reffo et al.[7] deviate by up to 70 % (^{103}Rh, E_n=3–4 keV) from the data calculated from resonances, on the average they agree within 20 %. The agreement is surprisingly good for ^{181}Ta, especially in view of the relatively poor knowledge of resonance parameters.

As a formal alternative, the code of Beer[44] offers an extrapolation of the measured cross sections to low energies by fitting $\sigma = a E^{-b}$ to the data. The contributions to I_2 corresponding to this fit compare reasonably well with those based on resonance parameters, strength function or the data of Reffo[7], suggesting that such an extrapolation may be a reasonable approach if other information is lacking, at least for energies immediately below the measured range.

The integral I_4 extends to infinity but can be restricted in practice to several hundred keV, depending on the actual kT value. The shape of the cross sections at high energies was taken from Refs. 20,21,22, corrected according to Ref. 45 and normalized to our data. The normalization factors used for ^{93}Nb, ^{103}Rh and ^{181}Ta are 0.89, 0.85 and 1.12, respectively.

Maxwellian averaged cross sections were calculated for kT= 12, 20, 25, 30, 40 and 52 keV. The value at 12 keV was chosen to fit a recent s-process model in low mass stars of low metallicity, (e.g. Ref. 46), where most of the neutron exposure occurs at relatively low temperature. The value at 52 keV can be used for comparison with activation experiments using the T(p,n) reaction, which simulates a Maxwellian neutron energy distribution at rather high temperatures[47]. For each thermal energy, $\langle\sigma\rangle$ was calculated twice: The first result includes all measured data from 3 to 200 keV as given in Table XIV. For the second value no use was made of the relatively uncertain data in the interval from 3 to 5 keV, hence extending the range of I_1 or I_2. The final results are summarized in Tables XVII to XIX.

The uncertainties for $\langle\sigma\rangle$ were estimated in the following way: The resonance parameters of ^{93}Nb and ^{103}Rh are relatively complete; therefore, an uncertainty of 10 % was assumed for the sum $I_1 + I_2$ for these nuclei. For ^{181}Ta, resonances are only given up to 2 keV, mostly with unknown spins and radiation widths. In this case, an uncertainty of 20 % was assumed for $I_1 + I_2$. The uncertainty of I_3 consists of three components: statistics, systematic experimental uncertainties, and the 1.5 % uncertainty of the Au standard cross section. The uncertainty of I_4 at the high energy end was estimated to be smaller than 5 %. The individual uncertainties

TABLE XVII Maxwellian averaged neutron capture cross sections of ^{93}Nb. The individual contributions I_x from different energy ranges ΔE are quoted separately (see eq. 4).

kT	Res. Parameter			Statistical Model			Measurement			Extrapolation			Total	
[keV]	ΔE [keV]	I_1 [mbarn]	δI_1	ΔE [keV]	I_2 [mbarn]	δI_2	ΔE [keV]	I_3 [mbarn]	δI_3[a]	ΔE [keV]	I_4 [mbarn]	δI_4	<σ> [mbarn]	δ<σ>
12	0-3	52.3	5.2		-		3-200	447.8	10.8	>200	0.0	0.0	500.1	12.0
	0-5	89.6	9.0		-		5-200	410.8	9.1		0.0	0.0	500.4	12.8
20	0-3	20.0	2.0		-		3-200	334.1	6.9	>200	0.0	0.0	354.1	7.2
	0-5	35.3	3.5		-		5-200	318.9	6.4		0.0	0.0	354.2	7.3
25	0-3	13.0	1.3		-		3-200	289.4	5.8	>200	0.2	0.0	302.6	5.9
	0-5	23.2	2.3		-		5-200	279.3	5.4		0.2	0.0	302.7	5.9
30	0-3	9.2	0.9		-		3-200	255.9	5.0	>200	0.7	0.0	265.7	5.1
	0-5	16.4	1.6		-		5-200	248.6	4.8		0.7	0.0	265.7	5.0
40	0-3	5.2	0.5		-		3-200	208.0	4.0	>200	2.8	0.1	216.0	4.0
	0-5	9.5	1.0		-		5-200	203.8	3.9		2.8	0.1	216.1	4.0
52	0-3	3.1	0.3		-		3-200	169.0	3.2	>200	7.2	0.4	179.3	3.2
	0-5	5.7	0.6		-		5-200	166.4	3.1		7.2	0.4	179.3	3.2

[a] This uncertainty includes statistical and systematic uncertainty of the measured ratio and a 1.5 % uncertainty for the gold standard cross section

TABLE XVIII Maxwellian averaged neutron capture cross sections of ^{103}Rh. The individual contributions I_x from different energy ranges ΔE are quoted separately (see eq.4).

kT	Res.	Parameter		Statistical Model			Measurement			Extrapolation			Total	
[keV]	ΔE	I_1	δI_1	ΔE	I_2	δI_2	ΔE	I_3	δI_3[a]	ΔE	I_4	δI_4	$\langle\sigma\rangle$	$\delta\langle\sigma\rangle$
	[keV]	[mbarn]		[keV]	[mbarn]		[keV]	[mbarn]		[keV]	[mbarn]		[mbarn]	
12	0-3	92.5	9.3		-		3-200	1186.5	26.7	>200	0.0	0.0	1278.9	28.3
	0-4	174.2	17.4	4-5	29.7	3.0	5-200	1086.9	22.5		0.0	0.0	1290.8	30.3
20	0-3	35.4	3.5		-		3-200	962.4	18.4	>200	0.2	0.0	997.9	18.8
	0-4	68.6	6.9	4-5	12.5	1.3	5-200	921.5	17.1		0.2	0.0	1002.7	18.9
25	0-3	23.1	2.3		-		3-200	867.2	16.0	>200	0.9	0.1	891.2	16.2
	0-4	45.1	4.5	4-5	8.4	0.8	5-200	839.9	15.2		0.9	0.1	894.3	16.1
30	0-3	16.2	1.6		-		3-200	791.4	14.3	>200	2.9	0.1	810.5	14.4
	0-4	31.9	3.2	4-5	6.0	0.6	5-200	772.0	13.8		2.9	0.1	812.7	14.3
40	0-3	9.3	0.9		-		3-200	674.4	12.0	>200	11.6	0.6	695.3	12.0
	0-4	18.4	1.8	4-5	3.5	0.4	5-200	663.1	11.7		11.6	0.6	696.5	11.9
52	0-3	5.5	0.6		-		3-200	568.2	10.0	>200	28.7	1.4	602.4	10.1
	0-4	11.0	1.1	4-5	2.1	0.2	5-200	561.4	9.9		28.7	1.4	603.2	10.1

[a] This uncertainty includes statistical and systematic uncertainty of the measured ratio and a 1.5 % uncertainty for the gold standard cross section

TABLE XIX Maxwellian averaged neutron capture cross sections of ^{181}Ta. The individual contributions I_x from different energy ranges ΔE are quoted separately (see eq. 4).

kT	Res.	Parameter		Statistical Model			Measurement			Extrapolation			Total	
[keV]	ΔE	I_1	δI_1	ΔE	I_2	δI_2	ΔE	I_3	δI_3[a]	ΔE	I_4	δI_4	$\langle\sigma\rangle$	$\delta\langle\sigma\rangle$
	[keV]	[mbarn]		[keV]	[mbarn]		[keV]	[mbarn]		[keV]	[mbarn]		[mbarn]	
12	0-2	121.8	24.4	2-3	69.3	13.9	3-200	1239.2	29.0	>200	0.0	0.0	1430.3	48.0
	0-2	121.8	24.4	2-5	204.9	41.0	5-200	1099.6	23.3		0.0	0.0	1426.2	69.4
20	0-2	45.5	9.1	2-3	27.1	5.4	3-200	929.3	18.4	>200	0.1	0.0	1002.1	23.5
	0-2	45.5	9.1	2-5	82.9	16.6	5-200	871.9	16.6		0.1	0.0	1000.4	30.6
25	0-2	29.4	5.9	2-3	17.8	3.6	3-200	815.0	15.5	>200	0.8	0.0	863.0	18.1
	0-2	29.4	5.9	2-5	54.9	11.0	5-200	776.7	14.4		0.8	0.0	861.9	22.2
30	0-2	20.6	4.1	2-3	12.6	2.5	3-200	730.5	13.5	>200	2.5	0.1	766.2	15.1
	0-2	20.6	4.1	2-5	39.1	7.8	5-200	703.2	12.8		2.5	0.1	765.4	17.5
40	0-2	11.7	2.3	2-3	7.2	1.4	3-200	609.5	11.0	>200	10.3	0.5	638.7	11.7
	0-2	11.7	2.3	2-5	22.6	4.5	5-200	593.7	10.7		10.3	0.5	638.2	12.7
52	0-2	7.0	1.4	2-3	4.3	0.9	3-200	507.3	9.1	>200	25.7	1.3	544.3	9.5
	0-2	7.0	1.4	2-5	13.7	2.7	5-200	497.7	8.9		25.7	1.3	544.0	9.9

[a] This uncertainty includes statistical and systematic uncertainty of the measured ratio and a 1.5 % uncertainty for the gold standard cross section

are given together with the cross sections in Tables XVII to XIX. Except for small kT,the Au standard contributes most to the total uncertainty. (However, in many problems related to nuclear astrophysics, only cross section ratios are required so that this term cancels out.) At low kT, there are significant contributions also from the statistical uncertainties of the low energy data points and from the estimated uncertainties of the integrals I_1 and I_2 .

Other potential sources of uncertainties requiring consideration are the procedure for averaging the cross sections into energy bins before calculating the Maxwellian average, and uncertainties in the shape of the Au cross section. Starting from the high resolution Au cross sections of Macklin[41], the Maxwellian average was calculated according to eq. 5 with increasing bin widths for different kT values. The resulting effect of the bin width was found to be ≦ 0.2 %.

Because the cross section ratios $\sigma(X)/\sigma(Au)$ are energy-dependent, uncertainties in the shape of the Au cross section may lead to uncertainties in $\langle\sigma(X)\rangle$ in addition to the 1.5 % uncertainty quoted above. Assuming a slightly different slope with neutron energy but leaving the Maxwellian average unchanged has the effect that the corresponding deviations cancel in the integral. Since such deviations are certainly below 2 %, it was estimated that the resulting uncertainty of $\sigma\langle(X)\rangle$ does not exceed a few tenth of a percent even in unfavourable cases. Consequently, these two possible uncertainties have been neglected in the final results given in Tables XVII to XIX.

In Fig.21 the present results are compared with the experimental data for kT=30 keV published since 1970 and compiled in Ref.5. For our previous measurement, the data were directly taken from Ref.7 that were already calculated with the revised gold cross section of Macklin[41] . By mistake, the ENDF/BV data were quoted as the standard in Ref. 7; hence, these data were corrected a second time in Ref. 5. The data of Ref. 53 were not considered as they have been withdrawn in the meantime. The present results are 3 to 10 times more accurate compared to previous cross sections, and their uncertainties are still dominated by the standard cross section. In general, good agreement with the older measurements is obtained, but a systematic deviation of the data of Macklin et al. (Refs.20,21,22,45) is to be noted. Their data are 16 and 25 % larger for ^{93}Nb and ^{103}Rh, but 8 % lower for ^{181}Ta, all deviations being far outside the quoted uncertainties. These discrepancies seem to be correlated with the binding energies of the investigated isotopes and may be due to a problem with the weighting function. Recently, Corvi et al.[15] discovered significant differences

between calculated and experimentally determined weighting functions, which could account for the discrepant results if the weighting function of Macklin is rising too fast with pulse height.

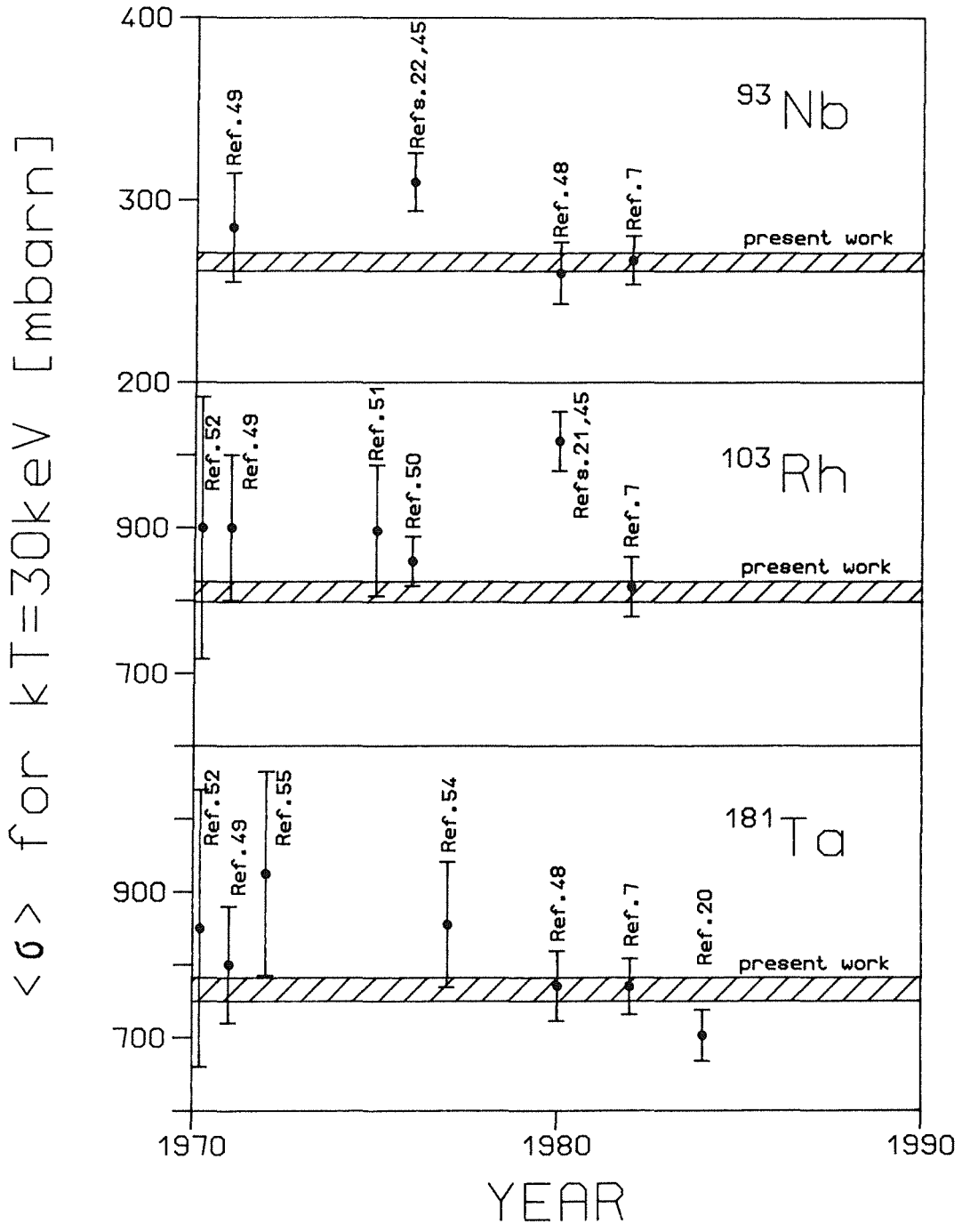

FIG. 21 Maxwellian averaged cross section at kT=30 keV of ^{93}Nb, ^{103}Rh and ^{181}Ta in comparison to the data published since 1970.

VIII. FURTHER IMPROVEMENTS AND CONCLUSIONS

During the first capture cross section measurements with the new experimental setup, the method was studied in detail and several possible improvemennts were persued for future implementation.

At present, the achieved uncertainty for the cross section ratio of ~1 % is mainly limited by the absolute normalization of the cross section shape. The main problems are the reduced signal to background ratio at low sum energies, especially in the spectra with multiplicity 1 and 2 (see Fig. 9), and the determination of the spectrum fraction below threshold.

In view of this situation, the following improvements are planned or already implemented:

(i) The spectra shown in Fig. 9 have been measured with 40 detector modules covering 95 % of the full solid angle; two positions were left open for the neutron beam to pass. This means for a capture cascade of multiplicity 4 that there is already a 20 % probability that one of the gamma–rays may escape from the detector without hitting a BaF_2 crystal at all. Hence, the number of events in the full energy peak is reduced and the average multiplicity appears too low. A significant fraction of the missing solid angle presently not filled with BaF_2 will be covered in the future by crystals with a central hole of 50 mm diameter for the neutron beam.

(ii) The background from radium impurities was reduced meanwhile by 40 % as the eight crystals with largest radium content were replaced. Correspondingly, the threshold in the sum energy spectrum could be reduced down to 1.8 MeV in a second experiment.

(iii) The pulsing system of our accelerator is presently being modified with the aim to improve the intensity per pulse in the extracted proton beam. Any such improvement will translate almost linearly in an improved signal to background ratio.

(iv) Neutron scattering in the air along the flight path through the detector was practically eliminated by evacuated flight tubes with thin Kapton foils.

The favorable combination of a Van de Graaff accelerator and the 4π BaF_2 detector for measurements in the keV neutron energy range was discussed in detail. With the $^7Li(p,n)^7Be$ reaction as an efficient source of keV neutrons and with flight paths of less than 1 m, it is well suited for the intended application, since neutron production can be restricted exactly to the energy range of astrophysical interest. The setup offers a number of possibilities for background suppression, and the remaining backgrounds can be studied quantitatively.

Barium fluoride proved to be the best available scintillator, combining high efficiency, good energy resolution, and excellent timing with a low sensitivity to capture of keV neutrons.

The new method required significant investments for scintillator, electronics, and computers; large amounts of data have to be handled, and painstaking procedures had to be worked out in order to verify each step of data analysis. However, already the first results on ^{93}Nb, ^{103}Rh, and ^{181}Ta confirmed that it was worth this effort, and that data for the cross section ratio relative to gold with an accuracy at the one percent level could be obtained. The comparison to the existing data measured with the classical pulse height weighting technique showed discrepancies of 10 - 25 %, probably correlated with the binding energy of the measured isotope. This supports the recently discovered problems with calculated weighting functions[15] and may be an indication that the accuracy claimed for this method was sometimes overestimated.

The determination of Maxwellian averaged capture cross section from the experimental data was discussed in detail. It was found that the energy range from 0 to 3 keV, which is not covered by the experimental data, may introduce significant uncertainties for low thermal energies kT. To overcome this difficulty, it is planned to use a complementary experiment with Moxon-Rae detectors and flightpaths of ~10 cm for measuring the cross section shape down to ~ 1 keV.

IX. REFERENCES

[1] F. Käppeler, H. Beer, and K. Wisshak, Reports on Progress in Physics **52**, 945 (1989).

[2] IUPAC. , N. E. Holden, ed., Atomic Weights of the Elements 1979, Pure Appl. Chem. **52**, 2349 (1980).

[3] P. J. Patchett Proc of the 46th Annual Meeting of the Meteoritical Society, Mainz, Fed. Rep. of Germany September 5-9 1983.

[4] H. Beer, G. Walter, R.L. Macklin, and P.J. Patchett, Phys. Rev. C **30**, 464 (1984).

[5] Z.Y. Bao and F. Käppeler At. Data Nucl. Data Tables **36**, 411 (1987).

[6] WRENDA 87/88 World Request List for Nuclear Data, W. Dahai, ed., INDC(SEC)-095/URSF International Atomic Energy Agency, Vienna, Austria 1988.

[7] G. Reffo, F. Fabbri, K. Wisshak, and F. Käppeler, Nucl. Sci. Eng. **80**, 630 (1982).

[8] K. Wisshak, F. Käppeler, and G. Schatz, Nucl. Instr. Meth. **221**, 385 (1984).

[9] K. Wisshak, F. Käppeler, G. Reffo, and F. Fabbri, Nucl. Sci. Eng. **86**, 168 (1984).

[10] B.C. Diven, J. Terrell, and A. Hemmendinger, Phys. Rev. **120**, 556 (1960).

[11] D. Kompe, Nucl. Phys. **A133**, 513 (1969).

[12] M.C. Moxon and E.R. Rae, Nucl. Instr. Meth. **24**, 445 (1963).

[13] R.L. Macklin and J.H. Gibbons, Phys. Rev. **159**, 1007 (1967).

[14] F. Käppeler, K. Wisshak, and L.D. Hong, Nucl. Sci. Eng. **84**, 234 (1983).

[15] F. Corvi, A.Prevignano, H. Liskien, and P.B. Smith, Nucl. Instr. Meth. **A265**, 475 (1988).

[16] F.G. Perey, J.O. Johnson, T.A. Gabriel, R.L. Macklin, R.R. Winters, J.H. Todd, and N.W. Hill, in Nuclear Data for Science and Technology, ed. S. Igarasi (Saikon, Tokyo, 1988) p. 379.

[17] R.L. Macklin, Nucl. Sci. Eng. **83**, 1309 (1983).

[18] R.L. Macklin, Nucl. Sci. Eng. **95**, 200 (1987).

[19] F. Corvi, C. Bastian, and K. Wisshak, Nucl. Sci. Eng. **93**, 348 (1986).

[20] R.L. Macklin, Nucl. Sci. Eng. **86**, 362 (1984).

[21] R.L.Macklin and J. Halperin, Nucl. Sci. Eng. **73**, 174 (1980).

[22] R.L.Macklin, Nucl. Sci. Eng. **59**, 12 (1976).

[23] F. Käppeler, G. Schatz, and K. Wisshak, Vorschlag zum Bau eines Wismuth-Germanat Detektors für Präzisionsmessungen zur Elementsynthese im s-Prozeß, report KfK-3472, Kernforschungszentrum Karlsruhe (1983).

[24] K. Wisshak and F. Käppeler, Nucl. Instr. Meth. **227**, 91 (1984).

[25] K. Wisshak, F. Käppeler, and G. Müller, Nucl. Instr. Meth. **A251**, 101 (1986).

[26] K. Wisshak, K. Guber, and F. Käppeler, Nucl. Instr. Meth. **A259**, 583 (1987).

[27] K. Wisshak, K. Guber, F. Käppeler, J. Krisch, H. Müller, G. Rupp, and F. Voß, The Karlsruhe 4π Barium Fluoride Detector, report KfK-4652, Kernforschungszentrum Karlsruhe (1989), and Nucl. Instr. Meth. (submitted).

[28] M. Tepe and F. Käppeler, in preparation.

[29] G.V. Muradjan, Yu.V. Adamchuck, Yu.G. Shchepkin, and M.A. Voskanyan, Nucl. Sci. Eng. **90**, 60 (1985).

[30] R.C. Block, P.J. Marano, N.J. Drindak, F. Feiner, K.W. Seeman, and R.E. Slovacek, in Nuclear Data for Science and Technology, ed. S. Igarasi (Saikon, Tokyo, 1988) p. 383.

[31] S. Yamamoto, K. Kobayashi, and Y. Fujita, in Nuclear Science and Technology, ed. S. Igarasi (Saikon, Tokyo, 1988) p. 375.

[32] P.E. Koehler and H.A. O´Brien, in Nuclear Data for Science and Technology, ed. S. Igarasi (Saikon, Tokyo, 1988) p. 1101.

[33] M. Laval, M. Moszynski, R. Allemand, E. Cormoreche, P. Guinet, R. Odru, and J. Vacher, Nucl. Instr. Meth. **206**, 169 (1983).

[34] The crystals were supplied by Merck GmbH Darmstadt, Fed. Rep. of Germany.

[35] S.F. Mughabghab, M. Divadeenam, and N.E. Holden, Neutron Cross Sections, Vol.1, Part A (Academic Press, New York, 1981).

[36] R.R. Winters, F. Käppeler, K. Wisshak, A. Mengoni, and G. Reffo, Astrophys. J. **300**, 41 (1986).

[37] G. Schatz and J. Oehlschläger, Ein Programm zur Berechnung der Ansprechwahrscheinlichkeit eines 4π-Szintillationszählers, report KfK-3710, Kernforschungszentrum Karlsruhe (1984).

[38] F.H. Fröhner, SESH- A Fortran IV Code for Calculating the Self-Shielding and Multiple Scattering Effects for Neutron Cross Section Data Interpretation in the Unresolved Resonance Region, report GA-8380, Gulf General Atomic (1968).

[39] V. McLane, C.L. Dunford, and P.F. Rose, Neutron Cross Section, Vol. 2, Neutron Cross Section Curves (Academic Press, New York, 1988).

[40] K. Wisshak, G. Walter, and F. Käppeler, Nucl. Instr. Meth. **219**, 136 (1984).

[41] R.L. Macklin, private communication (1982)

[42] W. Ratynski and F. Käppeler, Phys. Rev. C **37**, 595 (1988).

[43] R.L. Macklin and J.H. Gibbons, Rev. Mod. Phys. **37**, 166 (1965).

[44] H. Beer, private communications (1990).

[45] R.L. Macklin and R.R. Winters, Nucl. Sci. Eng. **78**, 110 (1981).

[46] R. Gallino, M. Busso, G. Picchio, C.M. Raiteri, and A. Renzini, Ap. J. Let. **334**, L45 (1988).

[47] F. Käppeler, A.A. Naqvi, and M. Al-Ohali, Phys. Rev. **C35**, 936 (1987).

[48] N. Yamamuro, K. Saito, T. Emoto, T. Wada, Y. Fujita, and K. Kobayashi, J. Nucl. Sci. Technol. **17**, 582 (1980).

[49] B.J. Allen, J.H. Gibbons, and R.L. Macklin, Adv. Nucl. Phys. **4**, 205 (1971).

[50] C. Le Rigoleur, A. Arnaud, and J. Taste, report CEA-R-4788, Centre d´Etudes Nucleaires de Cadarache (1976).

[51] R.W. Hockenbury, H.R. Knox, and N.N. Kaushal, Proc. Conf. Nucl. Cross Sections and Technology, eds. R.A. Schrack and C.D. Bowman, Washington, D.C. March 3-7 1975, NBS Special Publication 425, U.S. National Bureau of Standards (1975).

[52] M.P. Fricke, W.M. Lopez, S.J. Friesenhahn, A.D. Carlson, and D.G. Costello, Nuclear Data for Reactors, Helsinki (IAEA Vienna); Vol.II ,265 (1970).

[53] H. Beer and F. Käppeler, Phys. Rev. **C21**, 534 (1980).

[54] V.N. Kononov, B.D. Yurlov, E.D. Poletaev, and V.M. Timokhov, Yad. Fiz. **26**, 947 (1977).

[55] J.R.D. Lepine, R.A. Douglas, and H.A. Maia, Nucl. Phys. **A196**, 83 (1972).

X. APPENDIX

A. Two dimensional spectra of the gold and rhodium samples in dependence of detector multiplicity measured with a neutron spectrum with 100 keV maximum energy and a sum energy threshold of 2.7 MeV

Fig. A1 Gold sample measured spectra

Fig. A2 Gold sample spectra corrected for sample independent background

Fig. A3 Gold sample spectra corrected for capture of sample scattered neutrons

Fig. A4 Rhodium sample measured spectra

Fig. A5 Rhodium sample spectra corrected for sample independent background

Fig. A6 Rhodium sample spectra corrected for capture of sample scattered neutrons.

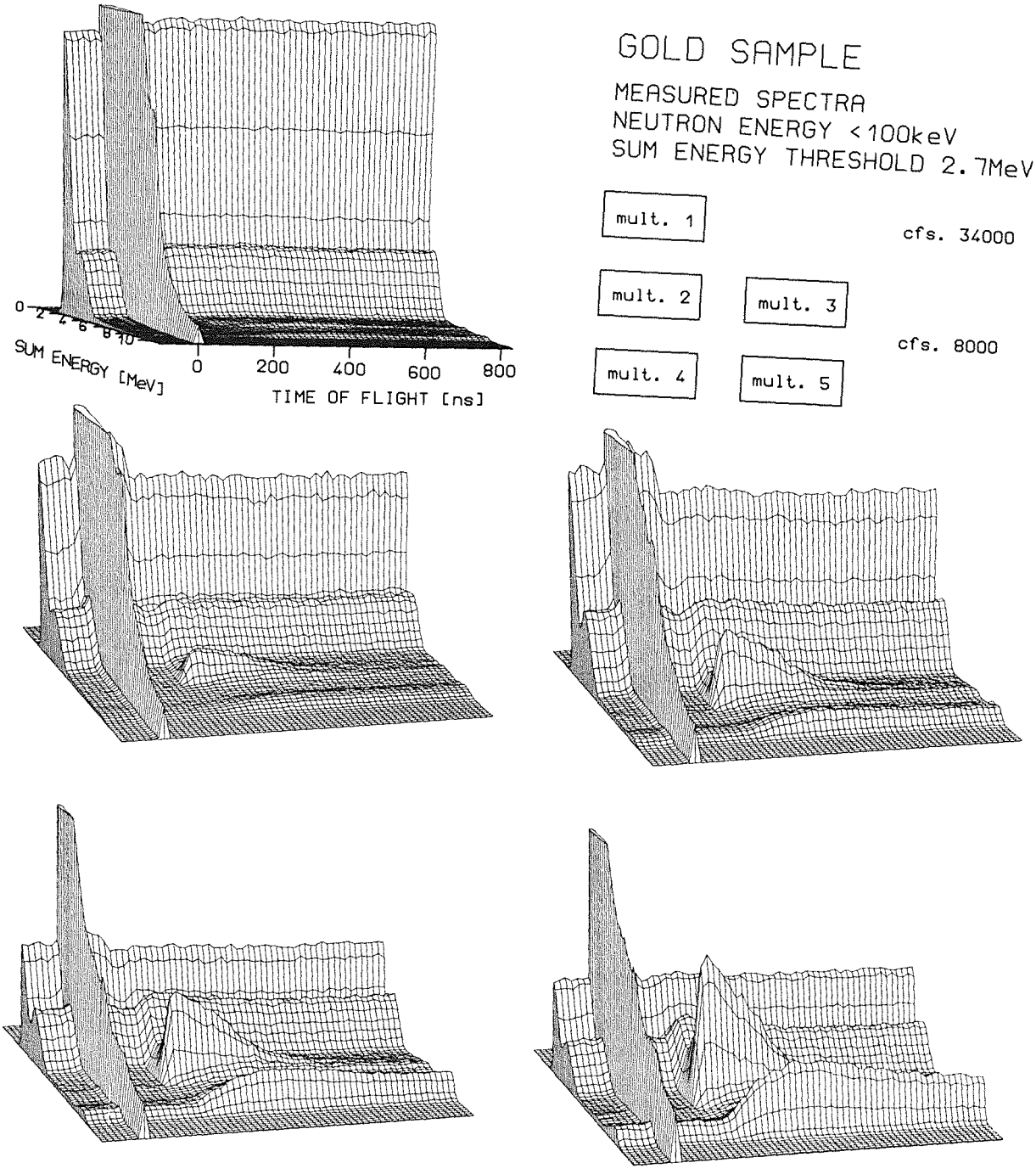
GOLD SAMPLE
MEASURED SPECTRA
NEUTRON ENERGY <100keV
SUM ENERGY THRESHOLD 2.7MeV
mult. 1
cfs. 34000
mult. 2
mult. 3
cfs. 8000
mult. 4
mult. 5
SUM ENERGY [MeV]
0
2
4
6
8
10
0
200
400
600
800
TIME OF FLIGHT [ns]

FIG: A1

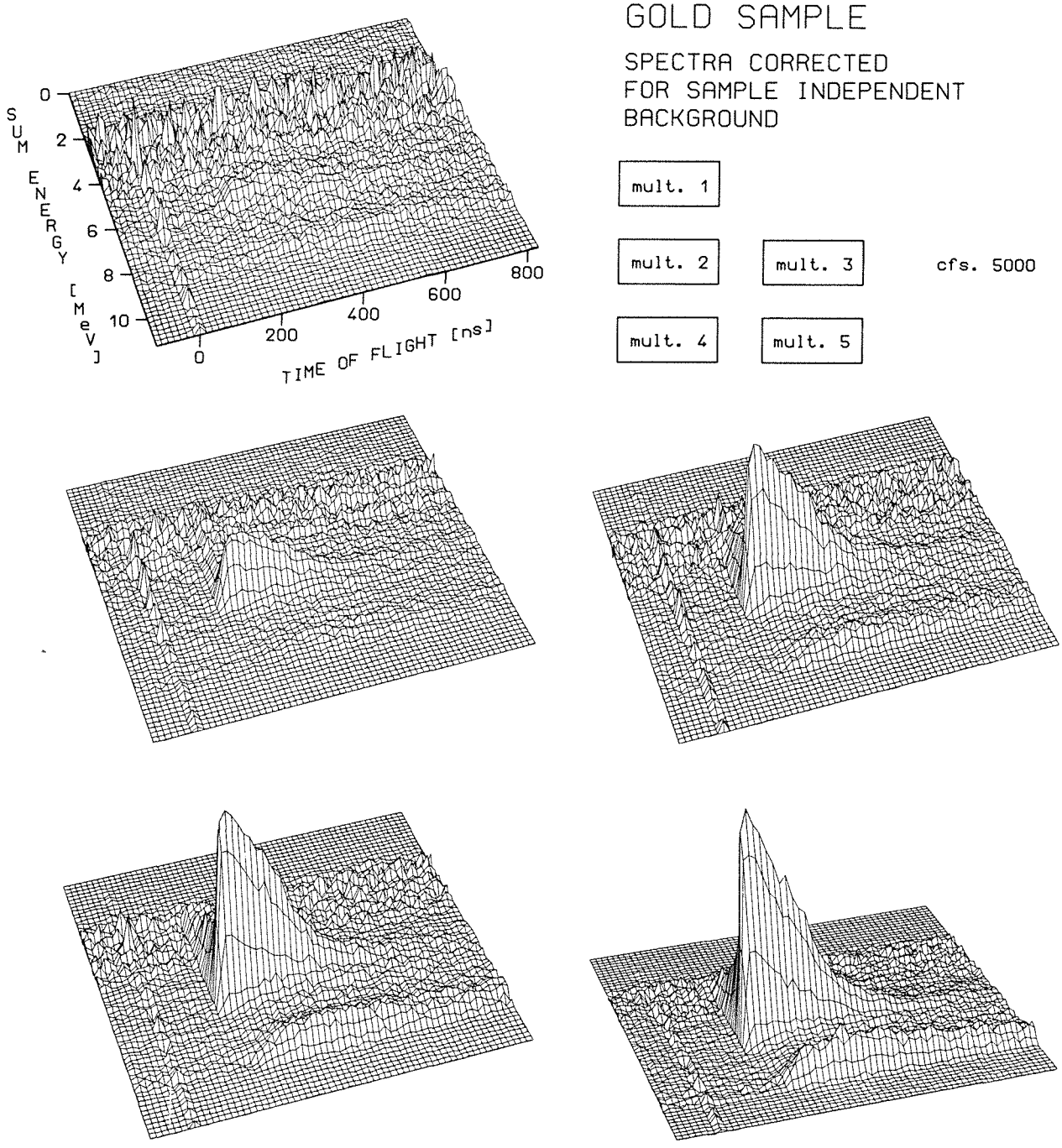
GOLD SAMPLE
SPECTRA CORRECTED
FOR SAMPLE INDEPENDENT
BACKGROUND
mult. 1
mult. 2
mult. 3
cfs. 5000
mult. 4
mult. 5
SUM ENERGY [MeV]
0
2
4
6
8
10
0
200
400
600
800
TIME OF FLIGHT [ns]

FIG: A2

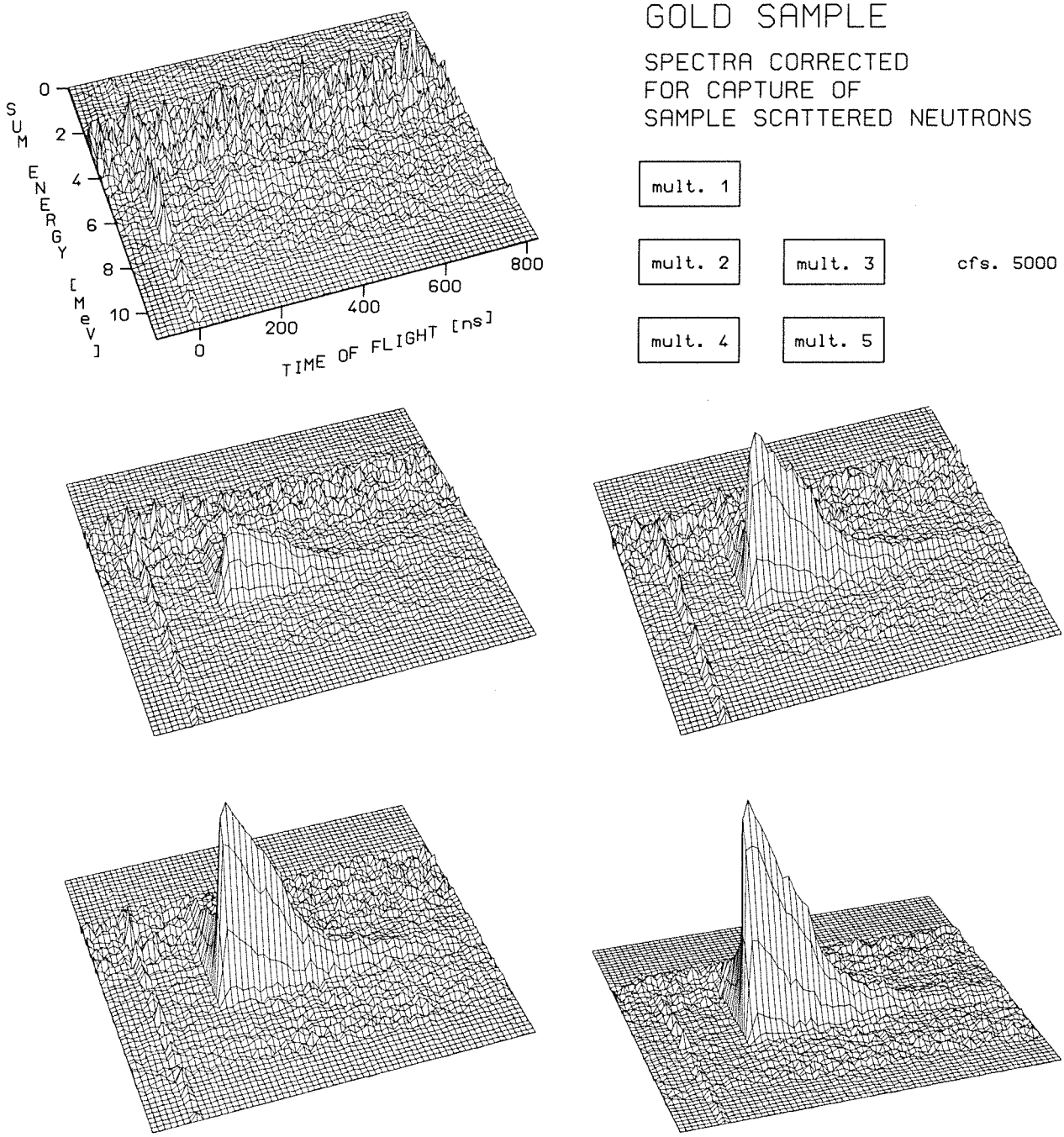
GOLD SAMPLE
SPECTRA CORRECTED
FOR CAPTURE OF
SAMPLE SCATTERED NEUTRONS
mult. 1
mult. 2
mult. 3
cfs. 5000
mult. 4
mult. 5
SUM ENERGY [MeV]
0
2
4
6
8
10
0
200
400
600
800
TIME OF FLIGHT [ns]

FIG. A3

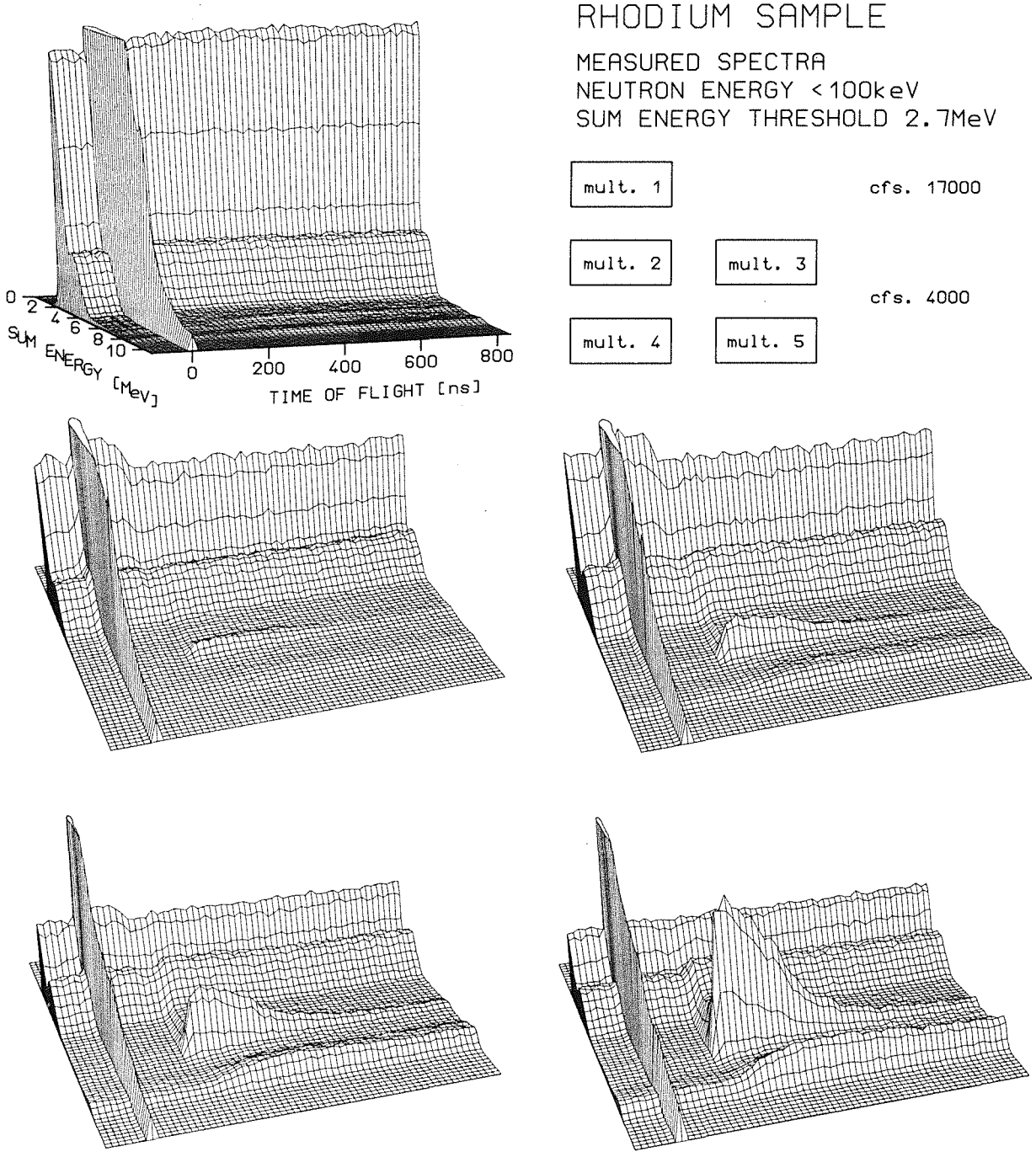
RHODIUM SAMPLE
MEASURED SPECTRA
NEUTRON ENERGY <100keV
SUM ENERGY THRESHOLD 2.7MeV
mult. 1
cfs. 17000
mult. 2
mult. 3
cfs. 4000
mult. 4
mult. 5
0
2
4
6
8
10
SUM ENERGY [MeV]
0
200
400
600
800
TIME OF FLIGHT [ns]

FIG. A4

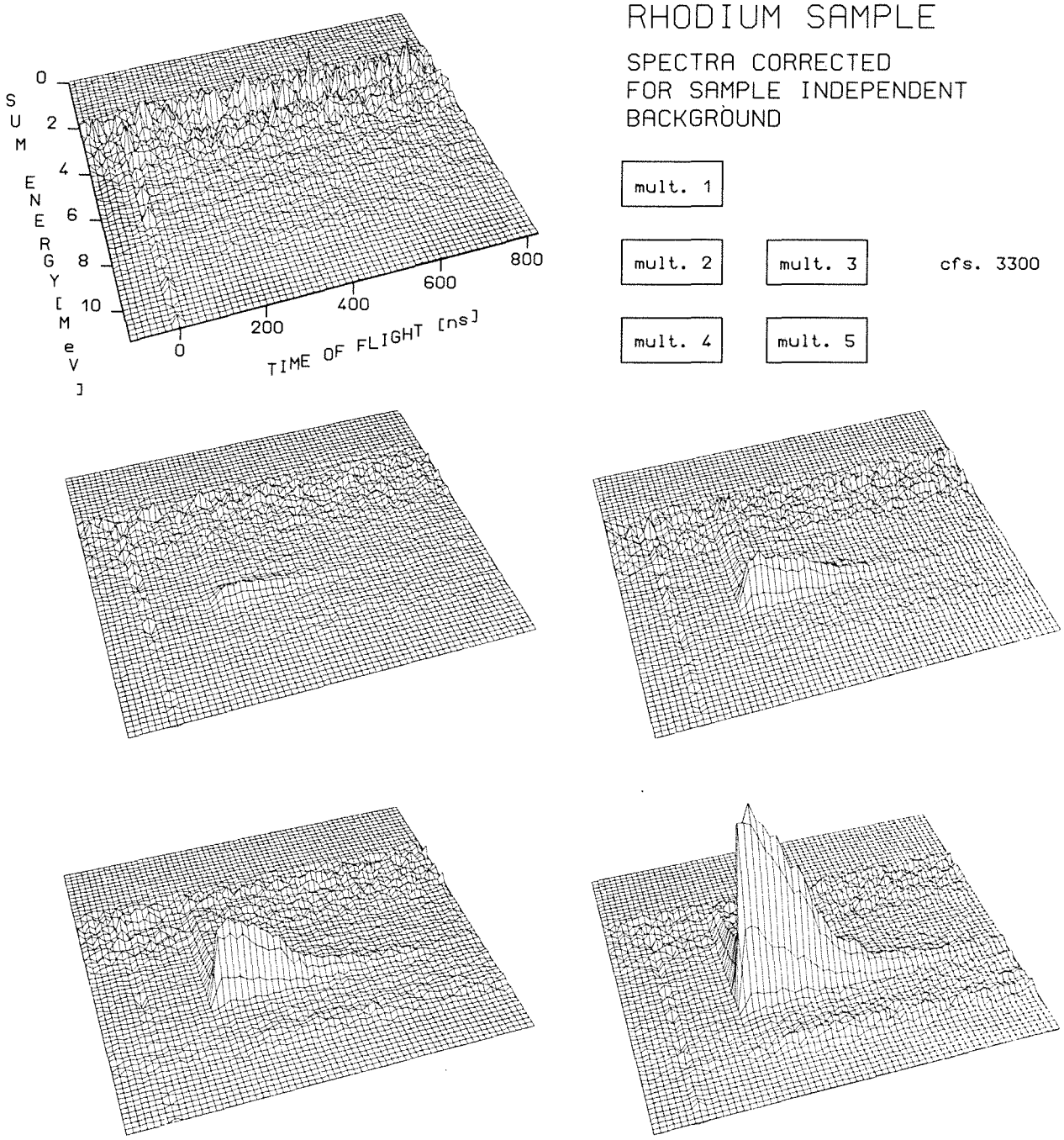
RHODIUM SAMPLE
SPECTRA CORRECTED
FOR SAMPLE INDEPENDENT
BACKGROUND
mult. 1
mult. 2
mult. 3
cfs. 3300
mult. 4
mult. 5
SUM ENERGY [MeV]
0
2
4
6
8
10
0
200
400
600
800
TIME OF FLIGHT [ns]

FIG. A5

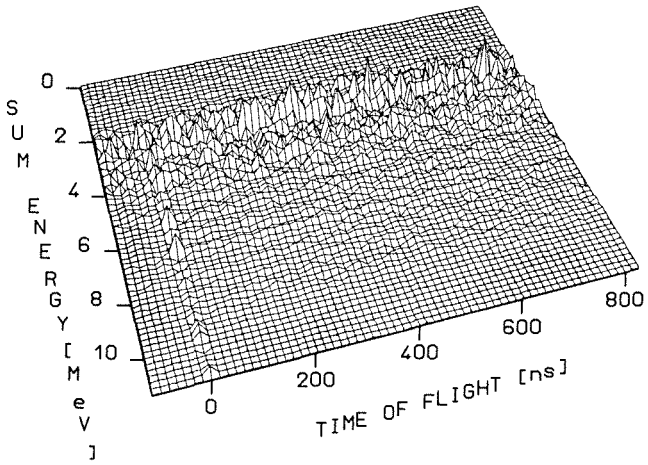

RHODIUM SAMPLE

SPECTRA CORRECTED
FOR CAPTURE OF
SAMPLE SCATTERED NEUTRONS

mult. 1

mult. 2 mult. 3 cfs. 3300

mult. 4 mult. 5

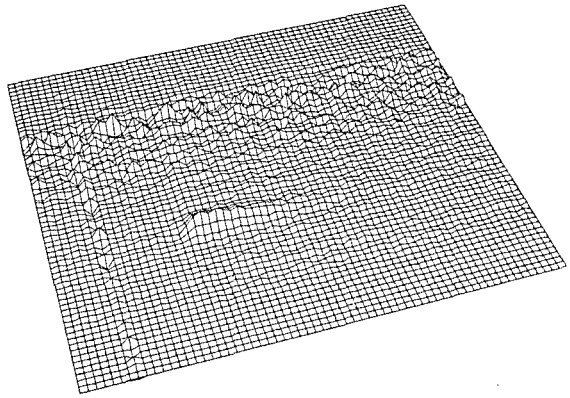

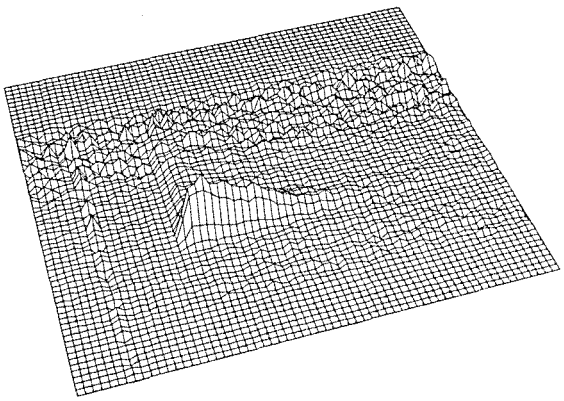

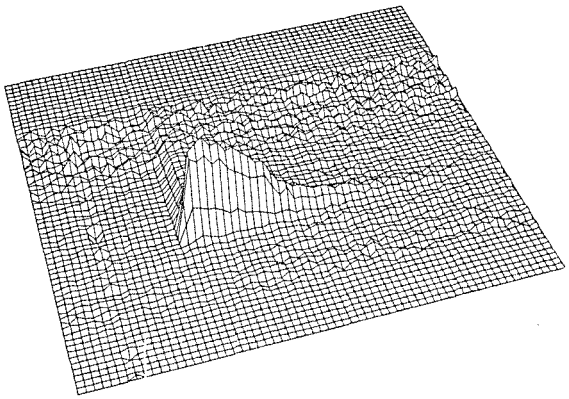

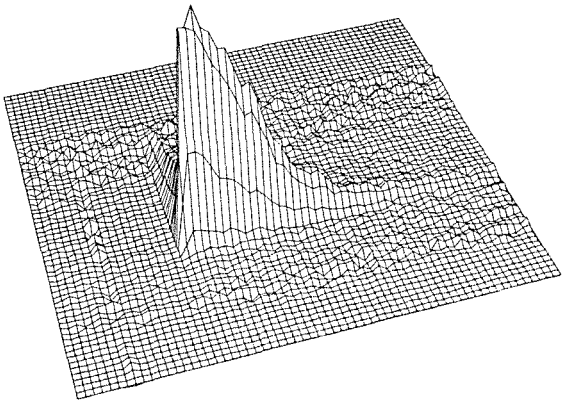

FIG. A6

XI. ACKNOWLEDGEMENTS

The authors would like to thank G. Rupp and H. Müller for continuous support in optimizing the experimental setup and the electronics. We appreciate the efforts of the Van de Graaff crew in providing optimum beam conditions, and we thank F. Fröhner and H. Beer for their help in the calculations of multiple scattering corrections and Maxwellian averaged cross sections.